Mechanical effects of light in presence of optical spin-orbit interaction

Hernando Magallanes González

université de BORDEAUX

THÈSE PRÉSENTÉE

POUR OBTENIR LE GRADE DE

DOCTEUR DE

L'UNIVERSITÉ DE BORDEAUX

ÉCOLE DOCTORALE DES SCIENCES PHYSIQUES DE L'INGÉNIEUR

SPÉCIALITE : LASER, MATIÉRE ET NANOSCIENCES

Par Hernando MAGALLANES GONZÁLEZ

Sujet:

Mechanical effects of light in presence of optical spin-orbit interaction

Sous la direction de : Etienne BRASSELET

Soutenance le 18 décembre 2019.

Membres du jury :

M. HANNA, Simon	Reader in physics	Président
M. DUPONT, Laurent	Professeur des universités	Rapporteur
Mme. VOLKE SEPULVEDA, Karen	Associate professor	Rapporteur
M. BRASSELET, Etienne	Directeur de recherche	Directeur de thèse

Titre : Effets optomécaniques en présence de couplage spin-orbite pour la lumière

Résumé : Des interactions entre la matière et la lumière sont à l'origine de phénomènes opto-mécaniques. L'une des caractéristiques distinctives de l'interaction lumière-matière est l'interaction spin-orbite de la lumière. Cette dernière s'étudie au sein d'un domaine de recherche émergent consacré à l'étude des effets opto-mécaniques en présence de l'interaction entre la polarisation et des degrés de liberté spatiaux de la lumière. En particulier, ce travail vise à observer directement la manifestation (i) des forces latérales et (ii) des couples optiques gauches qui sont des effets opto-mécaniques contre-intuitifs. On utilise pour cela des milieux non homogènes et anisotropes comme ingrédients essentiels à la fabrication d'éléments optiques spin-orbite. Nous rapportons tout d'abord, les tentatives d'observations expérimentales directes, à partir des résultats préliminaires obtenus préalablement dans notre groupe de recherche. Nous présentons ensuite de nouvelles propositions d'expérimentations ainsi qu'une généralisation adaptée au cas des forces latérales. Par conséquent, nous rapportons d'une observation directe à l'échelle du millimètre des forces latérales optiques et des couples optiques gauches dépendantes du spin en effectuant une étude complète. Il ressort de l'analyse des deux phénomènes que leurs vitesses peuvent être augmentées en réduisant l'inertie ou la taille des éléments optiques spin-orbite au point de rendre les phénomènes significatifs à l'échelle microscopique et intéressants pour les applications technologiques. Nous faisons un rapport chronologique de notre travail expérimental consistant à observer le moment de force orienté à gauche à l'échelle du micromètre en utilisant des versions miniaturisées des échantillons précédents. Comme la dernière tentative n'était pas concluante, nous finissons par proposer de nouvelles stratégies prometteuses pour manipuler de tels micro-objets.

Mots clés : Interaction spin-orbite optique, Moment angulaire orbital, Optomécanique.

Title : Mechanical effects of light in presence of optical spin-orbit interaction

Abstract : Interactions between light and matter cause optomechanical phenomena, where a distinctive feature of light-matter interaction, namely, the spin-orbit interaction of light, takes place within an emerging research area dedicated to the study of optomechanical effects in the presence of the interplay between polarization and spatial degrees of freedom of light. In particular, this work aims to directly observe the manifestation of (i) lateral forces and (ii) left-handed torques, which are counterintuitive optomechanical effects, by using inhomogeneous and anisotropic media as a critical ingredient for the manufacture of spin-orbit optical elements. Hence, we report on their direct experimental observations attempts, starting from the preliminary results obtained in our group before this work, and then present our new proposals and further generalization to the case of lateral forces. Consequently, we report on a millimeter-scale direct observation of optical spin-dependent lateral forces and left-handed torques with a full study. From the analysis of both phenomena, it turns out that their speed can be increased by reducing the spin-orbit optical elements inertia or size, making the phenomena relevant at microscopic-scale and interesting for technological applications. Thus, we account for our experimental journey chronologically, to observe the left-handed torque at micrometer-scale with samples that correspond to miniaturized versions of previous ones. Since the last results were inconclusive, we finish by proposing new strategies of manipulation of such micro-elements with promising implementation.

Keywords : Spin-orbit interaction of light, Orbital angular momentum, Optomechanics.

Unité de recherche

Laboratoire Ondes et Matière d'Aquitaine, (UMR 5798), Bât A4N, 351 Cours de la Libération, 33405 Talence Cedex, France

I dedicate this work to my brothers,
Javier, Adrián, Pablo and Vanessa,
to my mom Gloria and dad José Luis,
as well as to my future wife Eva.

February 7, 2020

Acknowledgements

I want to thank Etienne Brasselet from the bottom of my heart for the opportunity of life he gave me when he invited me to work with him. With this work, I leave a testimony of his creativity, professionalism, and leadership.

I also thank all the members of LOMA, who together have created a cutting-edge scientific research institution. During my stay, I enjoyed his company, support, and friendship, being part of an environment that invited teamwork. I want to thank especially Stephano and Marcela, dear friends with whom I spent memorable leisure time, and from whom I received comfort in difficult times.

Finally, I want to thank the team's gangs, starting with the French, Delphine, Charles, Mikaël, Loïc, and Vincent; to the Armenian, Davit, Mushegh, and Artur; to the Ukrainian, Georgiy, Tetiana, and Nina; and to the Mexican (of which I was part), Benjamín, and Juan Pablo. Everyone contributes to the success of the team in a way that makes it so Singular!

Contents

CHAPTER 1

General introduction

This chapter aims at briefly presenting the key ingredients at play in the research work done during this thesis. First, linear and angular momentum of matter and light are introduced, followed by their interaction from which results optomechanical phenomena, the latter being the core of this work. Then we will present a particular feature of light-matter interaction, namely, the spin-orbit interaction of light. Indeed, the latter is the cornerstone of our work that takes place within an emerging research area dedicated to the study of optomechanical effects in presence of the interplay between polarization and spatial degrees of freedom of light. This chapter eventually summarizes the scientific position of our proposals with respect to the state of the art.

1.1 Mechanics

In classical mechanics, the variables used to describe the translational motion of an object have analog quantities for rotational motion. Among them, the variables used in this thesis (*linear* $\leftrightarrow$ *angular*) are: *spatial position* $\leftrightarrow$ *angular position*, *mass* $\leftrightarrow$ *rotational inertia*, *linear momentum* $\leftrightarrow$ *angular momentum*, and *force* $\leftrightarrow$ *torque*. In a closed system composed of N elements, the total linear momentum of the system is the sum of the linear momenta of all its elements. Similarly, the total angular momentum of the system is the sum of the angular momenta of all its elements. We express the total linear momentum as $\boldsymbol{P}$, and the total angular momentum as $\boldsymbol{J}$. These quantities are highlighted in Table 1.1 in the framework of the fundamental principles of mechanics that allow describing the motion of systems under the action of external forces and torques, summarized here for a Galilean reference frame. In that case, (i) the

MECHANICAL PRINCIPLES	
$\frac{d}{dt}\boldsymbol{P} = \sum_i \boldsymbol{F}_{\text{ext},i}$	$\frac{d}{dt}\boldsymbol{J} = \sum_i \boldsymbol{\Gamma}_{\text{ext},i}$
TRANSLATION	ROTATION

Table 1.1: Summary of the fundamental principles of mechanics describing the translational and rotational dynamics of an object in a Galilean reference frame, where $\boldsymbol{F}_{\text{ext},i}$ and $\boldsymbol{\Gamma}_{\text{ext},i}$ represent the external forces and external torques exerted on the object, respectively.

rate of change of the linear momentum of an object equals the net external force exerted on the object and, (ii) the rate of change of the angular momentum of an object equals the net external torque exerted on the object.

The angular momentum can be decomposed formally into an orbital part and a spin part. The former is associated with off-axis motion of the center of mass, called orbital angular momentum ($\boldsymbol{L}$), whereas the latter is associated with rotational motion on-axis of the center of mass, called spin angular momentum ($\boldsymbol{S}$). For instance, the angular momentum in free space of a solid object of volume V, expresses as

$$\boldsymbol{J} = \iiint \boldsymbol{r} \times \boldsymbol{p} \; d\mathrm{V} \tag{1.1}$$

where $\boldsymbol{p}$ is the linear momentum per unit volume and $\boldsymbol{r}$ is the position vector. Introducing the center of mass position vector $\boldsymbol{r}_{\text{cm}}$ with respect to an origin point in space, and defining $\boldsymbol{r} = \boldsymbol{r}_{\text{cm}} + \boldsymbol{r}'$, one gets

$$\boldsymbol{J} = \boldsymbol{r}_{\text{cm}} \times \boldsymbol{P} + \iiint \boldsymbol{r}' \times \boldsymbol{p} \; d\mathrm{V} = \overbrace{\boldsymbol{L}}^{\text{orbital}} + \underbrace{\boldsymbol{S}}_{\text{spin}} . \tag{1.2}$$

Noteworthy, the orbital part is associated with the center of mass trajectory, as illustrated by the sketch in Fig.1.1.

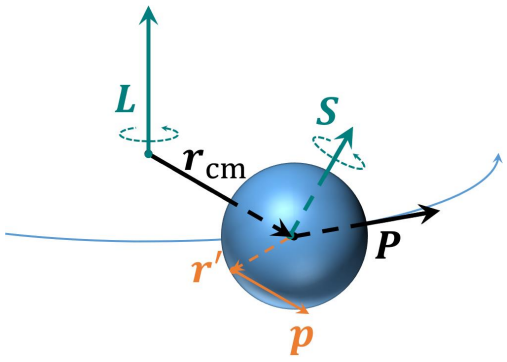

Figure 1.1: *Linear momentum* $\boldsymbol{P}$*, orbital angular momentum* $\boldsymbol{L}$*, and spin angular momentum* $\boldsymbol{S}$*, of a solid sphere moving along a curved path, where* $\boldsymbol{r}_{\mathrm{cm}}$ *is the position vector of the center of mass with respect to an origin point in space. Writing the position vector as* $\boldsymbol{r} = \boldsymbol{r}_{\mathrm{cm}} + \boldsymbol{r}'$ *allows identifying* $\boldsymbol{r}'$ *as the position vector of an elementary volume of the object with respect to its center of mass, and* $\boldsymbol{p}$ *refers to the linear momentum per unit volume of the object.*

Importantly, in the microscopic world, angular momentum is actually quantized, as early postulated by Bohr for the orbital angular momentum. Although Bohr's model is outdated, the modern view provided by quantum mechanics also states quantization. Indeed, quantum mechanics gives states whose allowed eigenvalues for the total angular momentum generator along an axis (say, z) are integer or half-integer. Of course, for macroscopic systems, quantization is barely detectable. However, when dealing with classical optomechanics, it is interesting to recall the quantum picture of photons, which is classically relevant to consider when dealing with sufficiently low photon flux, implying that no more than one photon at a time interacts with the material system. To give an idea of it, let us consider a system with characteristic size L. The corresponding maximum optical power that corresponds to 'one photon at a time in the system' is $P = \hbar\omega c/L$ where ω is the optical angular frequency, see Fig.1.2. This gives at a glance the relationship between the optical power of a source and an optical element in order to be in such a regime.

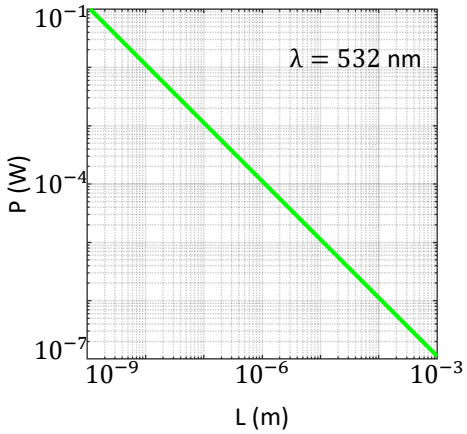

Figure 1.2: *Maximum optical power of a beam, P, that corresponds to "one photon at a time in the system", for light wavelength λ = 532 nm (which is the one used in this thesis), as a function of the characteristic size, L, of the system.*

1.2 Optics

Light is an electromagnetic wave described by two related real vector fields that are functions of the position and time: the electric field $\boldsymbol{\mathcal{E}}(\boldsymbol{r},t)$ and the magnetic field $\boldsymbol{\mathcal{B}}(\boldsymbol{r},t)$. In general, an electromagnetic wave is any solution of the wave equation derived from the Maxwell's equations. In our investigations, which are experimentally driven, we are interested in those that meet the criterion of paraxiality. Namely

$$\left|\frac{\partial^2 E}{\partial z^2}\right| \ll k\left|\frac{\partial E}{\partial z}\right| \quad \text{and} \quad \left|\frac{\partial E}{\partial z}\right| \ll k\,|E|\,, \tag{1.3}$$

where E is the electric field amplitude, k is the wavevector, and z is the spatial coordinate along the propagation direction of the wave.

Considering the electric field, for a monochromatic wave propagating along the z-axis towards $z > 0$ in free space, it is convenient to adopt the complex representation. We thus introduce the complex electric field

$$\boldsymbol{E}(z,t) = Ee^{i(kz-\omega t)}\mathbf{e}, \tag{1.4}$$

that satisfies $\boldsymbol{\mathcal{E}} = \mathrm{Re}\{\boldsymbol{E}\}$, where ω is the angular frequency, and $\mathbf{e}$ is a unit vector that represents the polarization state. In the Cartesian reference frame,

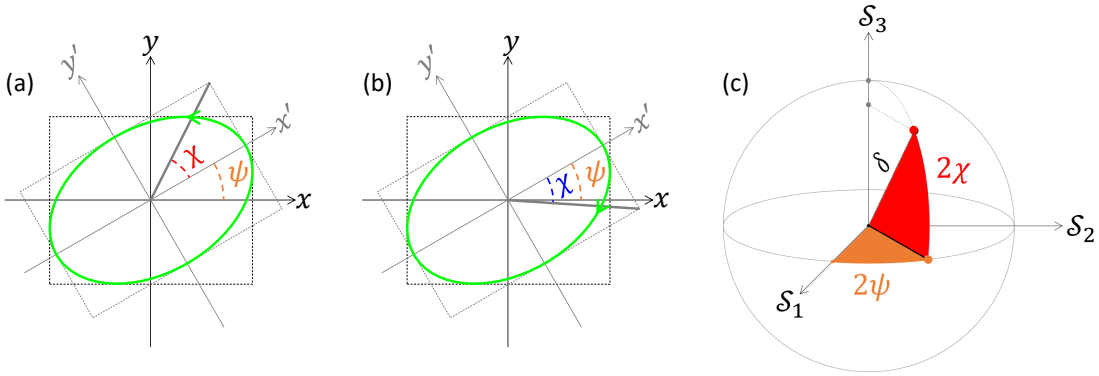

Figure 1.3: *(a,b) Polarization ellipse for left* ($\chi > 0$) *and right* ($\chi < 0$) *elliptical polarization state. (c) Representation of a fully polarized beam, characterized by an ellipticity angle and an azimuth angle, on the Poincaré unit sphere where the axes represent the reduced Stokes parameters and the gray arrow represents the reduced Stokes vector* $\mathbf{s} = (s_1, s_2, s_3)$.

the polarization vector is represented by a so-called Jones vector expressed in the (x, y) basis as:

$$\mathbf{e} = \begin{pmatrix} \cos\psi\cos\chi - i\sin\psi\sin\chi \\ \cos\psi\sin\chi + i\sin\psi\cos\chi \end{pmatrix}, \tag{1.5}$$

where $-\pi/4 \leqslant \chi \leqslant \pi/4$ and $0 \leqslant \psi \leqslant \pi$ are the ellipticity angle and azimuth angle, respectively (see Fig.1.3). In particular, circular polarization states are represented by

$$\mathbf{e}_\sigma = \frac{1}{\sqrt{2}}(\mathbf{x} + i\sigma\mathbf{y}), \tag{1.6}$$

where $\sigma = \pm 1$. Here we opt for the following convention to label the polarization handedness: right-handed (RH)/left-handed (LH) circular polarization states denote the clockwise/counterclockwise rotation of the tip of the real electrical vector when an observer is looking towards the source. Therefore, $0 < \chi \leqslant \pi/4$ and $-\pi/4 \leqslant \chi < 0$ respectively refer to LH and RH polarization states (see Fig.1.3(a,b)), whereas $\chi = 0$ refers to a linear polarization state. Such convention is consistent with the handedness of the helix formed by the real electric field vector at any time, as depicted in Fig.1.4.

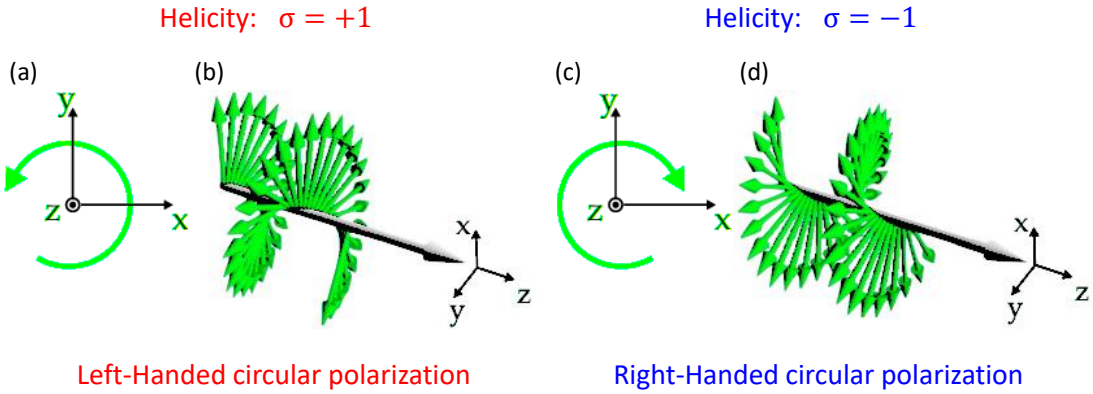

Figure 1.4: *Circularly polarized plane wave is a chiral electromagnetic field. In (a) and (c) the rotation of the electric field vector on a fixed plane propagating towards the reader. In (b) and (d), the electric field vectors (green arrows) of a light wave, at given time, propagating in the* **z** *direction.*

A practical method to represent the polarization state of light is to introduce the four-dimensional Stokes vector $\boldsymbol{\mathcal{S}} = (\mathcal{S}_0, \mathcal{S}_1, \mathcal{S}_2, \mathcal{S}_3)$ defined from the components (E_x, E_y) complex electric field according to

$$\boldsymbol{\mathcal{S}} = \begin{pmatrix} \mathcal{S}_0 \\ \mathcal{S}_1 \\ \mathcal{S}_2 \\ \mathcal{S}_3 \end{pmatrix} = \begin{pmatrix} |E_x|^2 + |E_y|^2 \\ |E_x|^2 - |E_y|^2 \\ 2\mathrm{Re}(E_x^* E_y) \\ 2\mathrm{Im}(E_x^* E_y) \end{pmatrix} = \begin{pmatrix} I_{\mathbf{e}} + I_{\mathbf{e}_\perp} \\ I_{\mathbf{e}_0} - I_{\mathbf{e}_\pi} \\ I_{\mathbf{e}_{\pi/4}} - I_{\mathbf{e}_{-\pi/4}} \\ I_{\mathbf{e}_{\sigma=+1}} - I_{\mathbf{e}_{\sigma=-1}} \end{pmatrix}. \tag{1.7}$$

It has the merit to be experimentally accessible via the measurement of a set of intensity values I_i, where the subscripts $(\mathbf{e}, \mathbf{e}_\perp)$ refer to any pair of orthogonal polarization states, and $\mathbf{e}_\alpha$ refers to a linear polarization state of angle α relative to the x-axis. It is also convenient to introduce the reduced Stokes vector, which is expressed as

$$\mathbf{s} = \frac{1}{\mathcal{S}_0} \begin{pmatrix} \mathcal{S}_1 \\ \mathcal{S}_2 \\ \mathcal{S}_3 \end{pmatrix}. \tag{1.8}$$

It is important to note that the representation using the Stokes vector allows describing the polarization state of any light field, whether it is unpolarized

($\delta = 0$), partially polarized ($0 < \delta < 1$) or entirely polarized ($\delta = 1$), where $\delta = |\mathbf{s}|$ is the degree of polarization. In the practical case of a fully polarized light field, whose polarization ellipse is unambiguously characterized by the pair of angles χ and ψ, its reduced Stokes vector can be expressed using these angles according to

$$\begin{pmatrix} s_1 \\ s_2 \\ s_3 \end{pmatrix} = \begin{pmatrix} \cos 2\chi \cos 2\psi \\ \cos 2\chi \sin 2\psi \\ \sin 2\chi \end{pmatrix}. \tag{1.9}$$

In that case, the vector $\mathbf{s}$ univocally corresponds to a point on the surface of a unit sphere called the Poincaré sphere, see Fig.1.3(c).

1.2.1 Linear and angular momenta of light

An electromagnetic wave carries linear momentum, in free space, its linear momentum density (per unit volume) is a vector defined by

$$\frac{\mathbf{S}}{c^2} = \epsilon_0 \boldsymbol{E} \times \boldsymbol{B}, \tag{1.10}$$

which is proportional to the instantaneous Poynting vector $\mathbf{S}$. The average rate (per unit time) of linear momentum flowing across a unit area oriented perpendicular to the direction of $\mathbf{S}$ is $\langle \mathbf{S} \rangle / c$, where $\langle \mathbf{S} \rangle$ is the average over a time period T of the instantaneous Poynting vector over time given by

$$\langle \mathbf{S} \rangle = \frac{1}{T} \int_0^T \mathbf{S} \, dt. \tag{1.11}$$

In addition, electromagnetic radiation can also be seen in terms of photons instead of waves. In free space, the linear momentum per photon within the plane wave framework for quantum field description is given by

$$\boldsymbol{p} = \hbar \boldsymbol{k}, \tag{1.12}$$

where $\hbar = h/2\pi$ is the reduced Planck constant. An electromagnetic wave may also carry angular momentum, and the average rate of angular momentum transported by an electromagnetic field is $\boldsymbol{r} \times \langle \mathbf{S} \rangle / c$.

1.2.2 Spin and orbital angular momenta of light

The momentum per unit volume associated with an electromagnetic wave is given by Eq.(1.10). Thus, the total angular momentum density is the cross product of the last equation with the position vector. The total angular momentum is therefore

$$\boldsymbol{J} = \iiint \epsilon_0 \boldsymbol{r} \times (\boldsymbol{E} \times \boldsymbol{B}) \, d\mathrm{V}. \tag{1.13}$$

The starting date of the modern study of the orbital angular momentum of light is often associated with the paper of Allen et al. [1]. This work showed that any paraxial light beam propagating along the z axis having a complex amplitude distribution expressing as $u(r, \varphi, z) = u_0(r, z) \exp(i\ell\varphi)$ in the cylindrical coordinate system, where ℓ is an integer, carries on angular momentum along the beam axis that can be separated into orbital and spin components. On the one hand, the orbital contribution per photon is determined solely by the azimuthal phase dependence and corresponds to

$$l_z = \ell\hbar. \tag{1.14}$$

On the other hand, the spin angular momentum per photon is solely determined by the polarization state, namely,

$$s_z = s_3\hbar \tag{1.15}$$

where we recall that $-1 \leqslant s_3 \leqslant 1$. The extremal values $s_z = \pm\hbar$ respectively correspond to left-handed and right-handed circular polarization states. A realistic example of light field of this kind is a Laguerre–Gaussian beam, which emerges naturally from paraxial optics in cylindrical coordinates, as discussed in Sec.1.2.3.

The identification of an orbital angular momentum is strongly suggested by the analogy between paraxial optics and quantum mechanics [2]. Here, the Schrödinger wave equation is identical to the paraxial form of the wave equation with t replaced by z, while the operator corresponding to the z-component of orbital angular momentum can be represented in the form $L_z = -i\hbar\partial/\partial\varphi$. The analogy allows much of paraxial optics, including orbital angular momentum, to be studied using the formalism of quantum mechanics. This has been articulated

by van Enk and Nienhuis [3], who introduced an eigenfunction description of laser beams, and by Nienhuis and Allen [4], who compared paraxial modes and their properties to those of the quantum harmonic oscillator. Noteworthy, the propagation of spin and orbital angular momenta through optical elements can usefully be described without reference to the spatial form of the light beam, by a generalization of the Jones matrix description of optical polarization [5]. This abstraction is analogous to separating the angular and radial wavefunctions in quantum mechanics.

To conclude this section, we note that fields described by an amplitude proportional to $\exp(i\ell\varphi)$ are associated with singular point where amplitude vanishes and phase is undefined. The phase subsequently circulates around these points of zero intensity. This points have received different names, such as: phase singularities, nodal points, wave dislocations and optical vortices. Phase singularities can also be seen as topological objects embedded in wave-front surfaces. Optical phase singularities are characterized by their topological charge which corresponds to the signed multiple of 2π explored by the phase per full turn along a closed circuit around the singularity. A light field of the form $u_0(r,z)\exp(i\ell\varphi)$ is therefore associated with a phase singularity having a topological charge ℓ. Orbital angular momentum, phase singularities and twisted wavefronts are therefore quantities that are intimately related.

1.2.3 Laguerre-Gaussian modes

Among all options to expand a paraxial field on a basis, the use of cylindrical coordinate is especially relevant when dealing with orbital angular momentum. It refers to the Laguerre-Gaussian basis where any field propagating along the z-axis is described as

$$\boldsymbol{E} = \sum_{\ell,p,\sigma} C_{\ell,p} u_{\ell,p}(r,z) e^{i\ell\varphi} e^{i(kz-\omega t)} \mathbf{e}_\sigma, \tag{1.16}$$

where, $C_{\ell,p}$ is a normalization constant, and

$$u_{\ell,p}(r,z) = \frac{w_0}{w(z)}\left[\frac{r}{w(z)}\right]^{|\ell|}\exp\left[-\frac{r^2}{w^2(z)}\right]L_p^{|\ell|}\left(\frac{2r^2}{w^2(z)}\right) \exp\left[\frac{ikr^2z}{2(z^2+z_R^2)}\right]\exp[-i(2p+|\ell|+1)\zeta(z)], \tag{1.17}$$

where, $r=\sqrt{x^2+y^2}$, $w(z)=w_0\sqrt{1+(z/z_R)^2}$ is the beam radius at z, w_0 is beam waist at $z=0$, $z_R=\pi w_0^2/\lambda$ is the Rayleigh distance, λ is the wavelength, $\zeta(z)=\arctan(z/z_R)$ is the Gouy phase for the Gaussian field ($\ell=0,\ p=0$), and $L_p^{|\ell|}$ are the generalized Laguerre polynomials with the radial index p and the topological charge ℓ. The main characteristics of a five ($p=0,\ -2\le 0\le 2$) Laguerre Gaussian beams are illustrated in Fig.1.5 where the plots of the wavefront, the phase, and the intensity are shown.

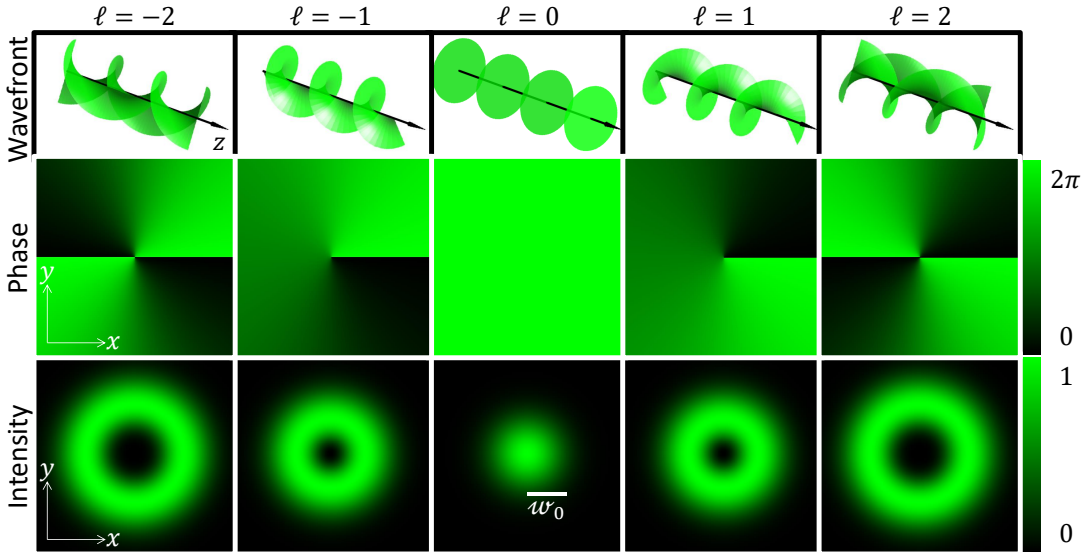

Figure 1.5: *Illustration of fundamental Laguerre-Gaussian modes (optical vortices) arranged in a 3×5 matrix. First row corresponds to the wave surfaces of constant phase (wavefronts) that carry on-axis phase singularities. Second and third rows correspond to the phase and normalized intensity distributions profiles, respectively, observed in the transverse plane at $z=0$ for the azimuthal indices $\ell=0,\pm1,\pm2$ and the radial index $p=0$.*

1.3 Optomechanics

We define an optomechanical effect has a mechanical response of matter to the action of light on it or viceversa. The former case can be a linear or rotational displacement induced by light while an example of the latter case is observed in the frequency shift associated with the linear or rotational Doppler effect. In our studies, we consider the mechanical response of matter for an isolated 'light + matter' system. The material motions are therefore described according to the Table 1.2.

OPTOMECHANICAL EFFECTS FOR AN ISOLATED SYSTEM	
$-\frac{d}{dt}\boldsymbol{P}_{\text{light}} = \boldsymbol{F}$	$-\frac{d}{dt}\boldsymbol{J}_{\text{light}} = \boldsymbol{\Gamma}$
TRANSLATION	ROTATION

Table 1.2: Optomechanical effects are defined by the mechanical principles.

As a photon traveling in free space interacts with a dielectric medium, it could be absorbed, reflected, refracted, or scattered depending on the nature and the spatial variations of the dielectric permittivity. Let us consider a monochromatic beam that propagates along the z-direction and interacts with a medium. Ensuing changes of the linear and angular momenta distribution of light, respectively, lead to

$$\boldsymbol{F} = -(\boldsymbol{p}^{\text{out}} - \boldsymbol{p}^{\text{in}})\frac{dN}{dt}, \qquad \text{and} \qquad \boldsymbol{\Gamma} = -(\boldsymbol{j}^{\text{out}} - \boldsymbol{j}^{\text{in}})\frac{dN}{dt}, \tag{1.18}$$

where dN is the number of photons interacting with the object during the time duration dt. Moreover, $\boldsymbol{p}$ and $\boldsymbol{j}$ are the linear and angular momenta per photon, respectively. From mechanical principles, the changes of momenta lead to the

force $\boldsymbol{F}$ and the torque $\boldsymbol{\Gamma}$. In general, for an incident monochromatic light beam of power P and angular frequency ω, the number of incident photon per unit time is $P/\hbar\omega$. The force and the torque exerted by this beam are therefore equal to

$$\boldsymbol{F} = \frac{P}{c}\boldsymbol{a}, \qquad \text{and} \qquad \boldsymbol{\Gamma} = \frac{P}{\omega}\boldsymbol{b}, \tag{1.19}$$

where $\boldsymbol{a}$ and $\boldsymbol{b}$ are dimensionless vectors whose magnitude and direction are the signature of the light-matter interaction processes. For instance, the mechanical effects resulting from a circularly polarized ($s_z = \sigma\hbar$, $\sigma = \pm 1$) Gaussian beam propagating along the unit vector $\boldsymbol{u}$ impinging on a perfect absorber are $\boldsymbol{F} = \frac{P}{c}\boldsymbol{u}$ and $\boldsymbol{\Gamma} = \sigma\frac{P}{\omega}\boldsymbol{u}$, see Figs.1.6(a,b). Another typical example is the case of a perfect mirror. The situation is depicted in Figs.1.6(c,d). The force is directed along the normal $\boldsymbol{z}$ to the mirror and is $\boldsymbol{F} = 2\cos\theta\frac{P}{c}\boldsymbol{z}$ and the torque is directed parallel to the mirror plane, $\boldsymbol{\Gamma} = 2\sigma\sin\theta\frac{P}{w}\boldsymbol{x}$.

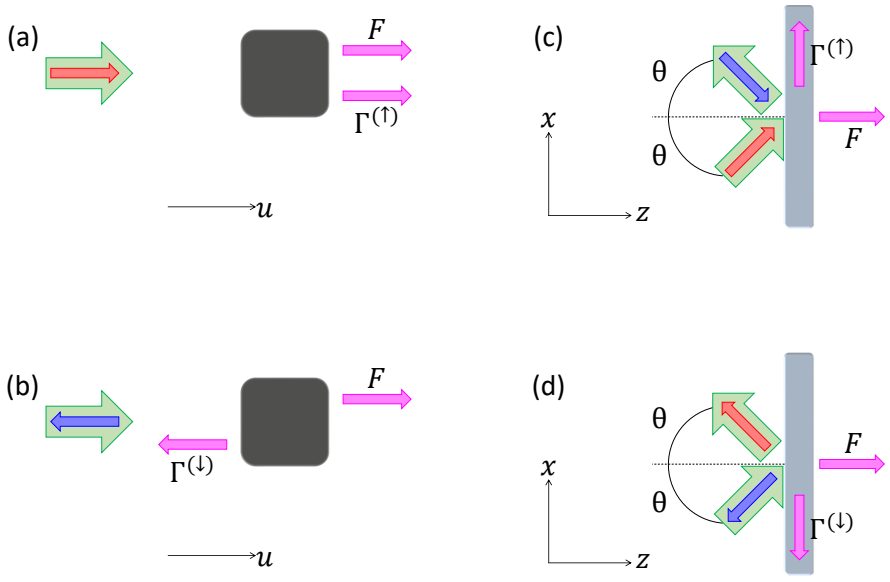

Figure 1.6: *Illustrations of typical optomechanical effects from a circularly polarized beam represented by a green arrow, in which the inner arrow stands for the light helicity, blue for right-handed and red for left-handed, while the pink arrows stands for the mechanical action of light on the material system, namely, the torque* $\boldsymbol{\Gamma}$ *and the force* $\boldsymbol{F}$*. In (a) and (b) the beam impinges on a perfect absorber while (c) and (d) the beam impinges on a perfect mirror.*

1.3.1 Historical review

Before discussing more recent aspects of optomechanical effects, hereafter we provide a brief survey of key historical works dealing with the mechanical action of light on matter, which is summarized in Fig.1.7.

Regarding the force that light can exert on matter, it is accepted that Kepler was the first to conjecture that light generates a radiation pressure, in 1619 [6], to explain the observation that the tail of a comet always points away from the Sun. Newton, also used this observation [7] as an argument of its corpuscular theory in 1704. In 1873, Maxwell [8], predicted from electromagnetic theory that a pressure field should result from the absorption or reflection of light, which was independently proved experimentally in the 1900's by Lebedev [9] and Nichols [10, 11].

Regarding the torque that light can exert on the matter, Sadowsky [12] and Poynting [13] independently predicted that circularly polarized electromagnetic wave also carries angular momentum, leading to the conjecture that light can also exert a torque. Beth [14] in 1936, detected and measured mechanically the angular momentum of circularly polarized light assuming the conservation of angular momentum holds as light passes through a half-wave plate suspended at the tip of a quartz wire. The designed apparatus used to detect and measure this effect, a torsional pendulum, was optimized to enhance the sought-after mechanical effect by an appropriate arrangement of quartz wave plates, and to reduce interferences, see Fig.1.7(d).

With respect to singularities in electromagnetic fields, Nye and Berry [15], in the 1970s, were considering the form of radio echoes reflected from the bedrock of the Antarctic ice sheet. To simulate this, they used ultrasound scattered from a rough surface and noted that the spatial form of the returned signal contained intensity nulls around which the phase of the signal changed by 2π. This led to the advent of the study of phase singularities era beyond acoustics and optics.

During few decades, there was a debate about the separation of the angular momentum in two independent contributions contributions of a spin and orbital nature. In 1992, Allen *et al.* [1] demonstrated the separation of both contributions for paraxial beams, and propose a way to measure them independently

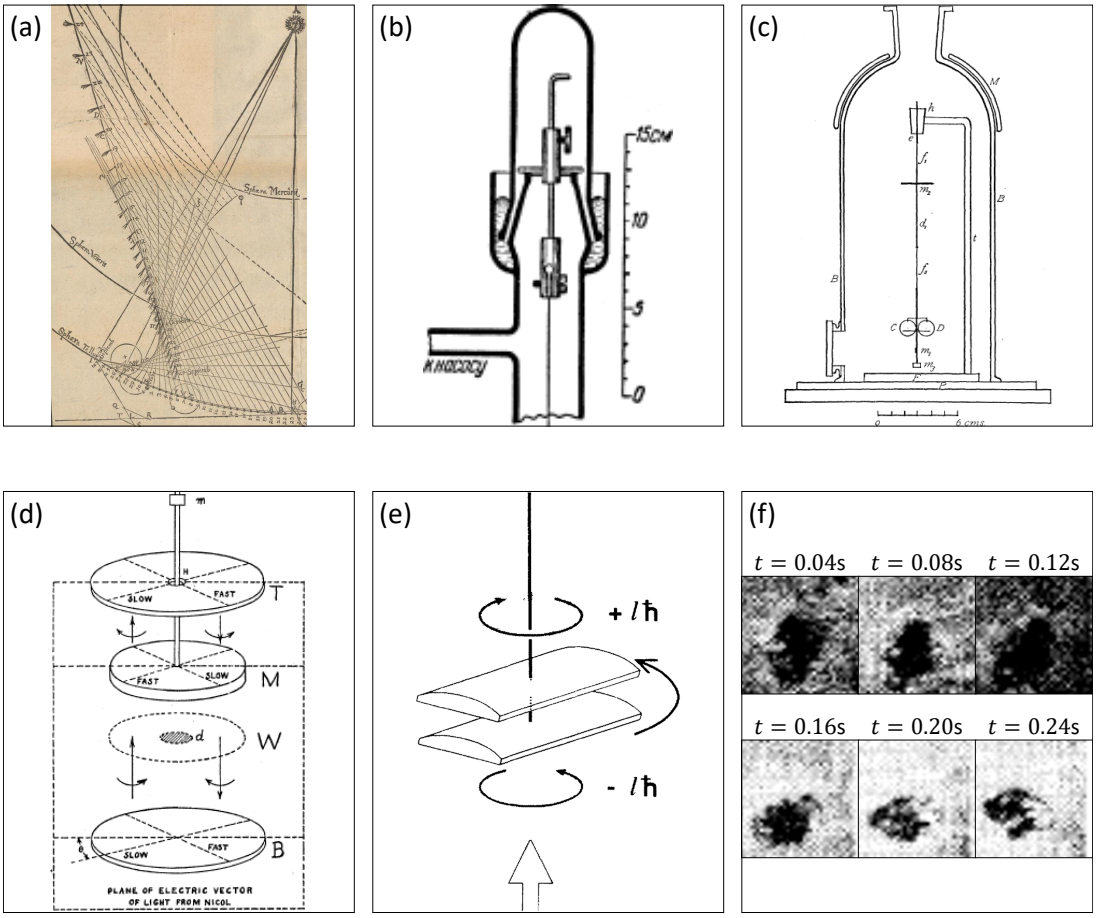

Figure 1.7: *Historical works on light linear and angular momenta. (a) Suggestion of Kepler [6] that a 'solar wind' push comet's tail away with respect the sun. (b) and (c) are Lebedev's [9] and Nichols' [11], respectively, torsion balances sketches to measure the radiation pressure; the main difference between their methods was the composition of the light's target and the operating pressure of the surrounded gas. (d) Beth's [14] torsion pendulum to measure the spin angular momentum of light, designed to observe the deflection of a quartz wave plate when polarized light is sent through the plate. (e) Allen's [1] conceptual experiment where light exerts a torque on a mode converter. (f) He [16] experiment; trapped black ceramic particle rotates through an angle about $\pi/2$ over a period of* 0.24s.

according to the use of an apparatus analog to that of Beth, but for the orbital angular momentum, Fig.1.7(e). Finally, He *et al.* [16] observed in 1995 the rotational mechanical effect of a pure optical orbital angular momentum transfer to an absorbing particle, see Fig.1.7(f).

Over time, the mechanical action of light on matter became a key tool in many areas such as atomic physics, optics, and biological science [17]. For instance, many optical beams and nanoscale devices have been proposed to mechanically act on nanoparticles in precise, stable and flexible ways. Noteworthy, during the writing of this thesis, A. Ashkin has been recognized with the Nobel prize in physics [18] for the optical tweezers and their application to biological systems. In particular, his work on optical scattering and gradient forces on micron-sized particles opened the field of optical trapping and manipulation. Further consequences of Ashkin's work include imaging [19, 20], applications in nonlinear optics [21] and quantum optics [22], information encoding [23, 24] among others.

In what follows, we introduce a few kinds of unusual optomechanical effects that form the motivation of our work.

1.3.2 Backward Forces

In general, a negative optical force is defined from the condition

$$\boldsymbol{F} \cdot \boldsymbol{P}^{\text{in}} < 0. \tag{1.20}$$

Optical forces are often sorted into the (conservative) gradient force and the (non-conservative) scattering and absorption forces. At first sight, using a light beam to pull a particle backwards may seem counter-intuitive, especially in the absence of an intensity gradient. Optical trapping of dielectric particles by a single-beam gradient force trap was demonstrated for the first reported time by Ashkin [25]. This confirmed the concept of backward force component that is due to an axial intensity gradient. The physical origin of the backward gradient force in single-beam gradient force traps is most obvious for particles whose diameter is large compared with λ. Indeed, in such situation, a geometrical ray tracing treatment allows identifying how the incident linear momentum is redistributed

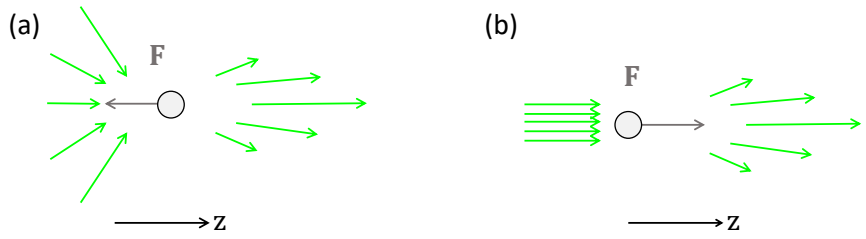

Figure 1.8: *Illustration of backward (a) and forward (b) motion of a scatterer depending on the balance of the total linear momentum between incoming and outgoing light.* ***F*** *is the optical force exerted on the scatterer and the green arrows refer to the linear momentum angular distribution.*

and lead into a backward balance of momentum that brings a spherical particle.

On the contrary, it has been shown that it is possible to exert a backward scattering force that pulls a particle towards of optical energy without an equilibrium point, which strikingly contrasts to the usual situation encountered in optical tweezers [26]. The forces acting against the propagation direction of light arise due to a particular redistribution of the linear momentum (Fig.1.8(a)) and can also appear as the light is scattered when passing from one dielectric medium to another with a higher refractive index in presence of a non-planar scatterer [27]. Also, an optical pulling force acting against the direction of incident energy flow for nonparaxial incident Bessel beams [28]. The latter is related with the fact that, for Mie particles, the destructive interference of the backscattered field helps to direct the scattering in the forward direction when it is in the presence of a plane wave.

In all the situations mentioned so far, the creation of a negative force over an extended range requires some assistance from either the surrounding objects or the medium. However, one could rely only on the properties of the object itself if the momentum transfer from the light to the object could be optimized in this scope. Both the shape and material composition of a small particle can be tailored to manipulate its scattering properties.

In principle, one can redirect the optical linear momentum at will in order to control the change of the direction and magnitude of the net optical force

as is done for a 'photon sail' or an optical lift [29]. However, some amount of momentum along the direction of light propagation is always lost in these situations, and this makes it impossible for a scattering object to move in a direction opposite to that of the incident beam.

In the next section we discuss another aspect of optical forces, when a component perpendicular to the incident flow of linear momentum arises.

1.3.3 Lateral forces

When a scattering event breaks symmetries, interesting manifestations of optomechanical effects take place. An example is the situation of lateral force $\boldsymbol{F}_{\perp}$, see Fig.1.9. Several theoretical studies have been proposed to address this effect; for instance, by placing an object close to an interface. This is the case for the evanescent field of the dielectric [30] or plasmonic [31] interfaces because the scattered field of a rotationally symmetric object in the proximity of a surface loses its symmetry. This was experimentally demonstrated soon after, by the measurements of spin-dependent lateral forces [32, 33], achieving forces with magnitude of the order of fN for micron-sized polystyrene particles placed at the water–air interface. Also lateral forces at the pN level have been detected and identified for nm-sized cantilever of a 'Lateral Molecular Force Microscope'. In all these situations, it is the coupling between the spin and orbital degrees of freedom of the light field that is at work.

In addition to the case of surface waves involved in [30, 31], the back-action of the guided modes in the presence of material spatial confinement has also been explored for circularly oscillating light-induced [34] dipoles, or spontaneously emitting atomic dipoles [35]. Other schemes have been proposed, for example, by placing a spinning cylinder in the path of a light beam [36], similar to the Magnus effect for light, or by using inhomogeneous light fields [37, 38, 39]. Finally, we also mention the first theoretical efforts to deploy spin-dependent lateral forces to sort chiral material by chiral light [40, 41, 42, 43, 44, 45].

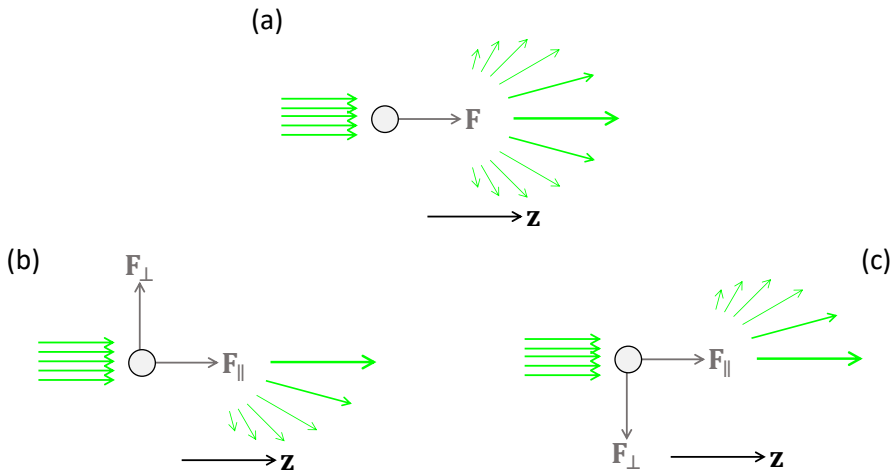

Figure 1.9: *In (a), a beam is symmetrically scattered by a particle. In (b) and (c), the impinging light is redistributed by the object in a way that it breaks the axisymmetry of the scattered field.* $\boldsymbol{F}$, $\boldsymbol{F}_{\parallel}$ *and* $\boldsymbol{F}_{\perp}$ *are the force and its parallel and perpendicular components, respectively. The green arrows have a similar meaning as in Fig. 1.8.*

1.3.4 Left-handed torques

In analogy with backwards force, where the motion of the object is against the average linear momentum of incident photons, one can consider its angular counterpart to which we refer to as 'left-handed torque' according to the terminology introduced in [46]. In this case, an incident light-field exerts a torque directed against the incident angular momentum (see Fig.1.10), that is to say,

$$\boldsymbol{\Gamma} \cdot \boldsymbol{J}^{\text{in}} < 0. \tag{1.21}$$

As argued in Ref.[46], 'left-handed torque' adjective is preferred to 'negative' because the sign of an optical torque can be directed either along or against the propagation direction of the incident light field. This specific feature provides the impetus to analyze the optical radiation torque exerted on an object from the stand point of such counter-intuitive optical radiation torque. An early numerical prediction of spin-driven left-handed torques was reported in [47] in the case of wavelength-sized prolate particles made of transparent isotropic medium under tightly focused circularly polarized Gaussian beams. Other earlier and related

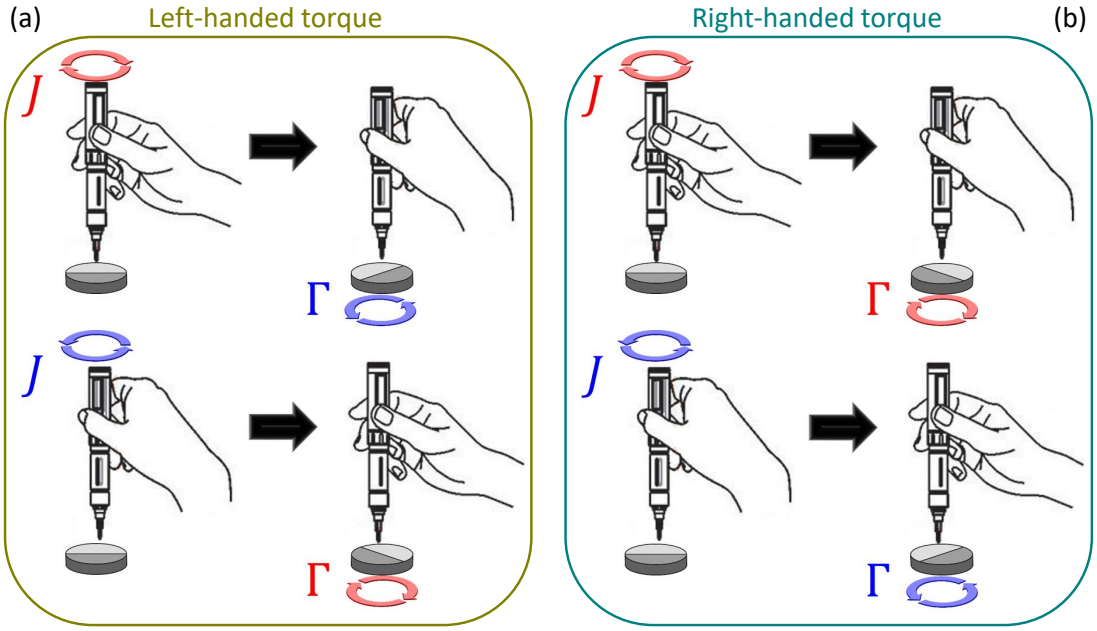

Figure 1.10: *Illustration of how we qualify the handedness of the torque applied to an object. (a) The screwdriver's twist is in counter-sense of the induced rotation of the disk. (b) The screwdriver's twist has the same sense as the induced rotation of the disk.*

works dealing with incident fields bearing orbital angular momentum are also worth mentioning, where reverse orbital motion is predicted [48] and observed [49]. Since then, several alternative routes have been discussed theoretically [50, 51, 52, 53, 54, 55].

Experimentally, the problem has started to be addressed by considering the use of an inhomogeneous and anisotropic transparent macroscopic medium. Practical difficulties associated with the direct observation of the torque on a macroscopic object have been bypassed by measuring the mechanical action of matter on light via Doppler effect [46]. Recently, while carrying out this thesis work, two experimental studies [56, 57] have been reported, which deal with multiple optically-isotropic nanoparticles bounded together by light. In [56], the authors examine the formation and concomitant rotation of electrodynamically bound dimers of 150 nm diameter silver nanoparticles trapped in circularly polarized focused Gaussian beams. By using a coupled-dipole/effective polarizability model,

it was revealed that retardation of the scattered fields and electrodynamic interactions can lead to a left-handed torque. In the more recent work [57], it was shown that left-handed optical torque can happen in self-assembled arrays of metal nanoparticles placed in polarized optical traps, the size of the arrays being in the range ~ 0.3 µm to ~ 3 µm.

In this thesis, we are experimentally dealing with unconventional optomechanical manifestations by exploiting a particular kind of light-matter interaction that we introduce hereafter: the optical spin-orbit interaction.

1.4 Spin-orbit interaction of light

Spin and orbital angular momenta of light are separately conserved during propagation in vacuum and in isotropic homogeneous transparent media, however, this is no longer the case in presence of material inhomogeneity or optical anisotropy. In that case, the polarization (spin) degree of freedom may couple to the spatial (orbital) degree of freedom: this defines the spin-orbit interaction of light.

1.4.1 Spin-controlled phase shaping using anisotropic and inhomogeneous media

Combining anisotropy and inhomogeneity allows efficient control of both the polarization and the spatial degrees of freedom of light. In practice this can be fruitfully used to shape the intensity and phase spatial distributions. In such media, strong spin-orbit interaction can be achieved with planar structures as early unveiled theoretically in 1997 by Bhandari [58], who proposed the first design of a spin-orbit lens made of a space-variant half-wave plate. In 2002, Hasman's team [59, 60] exploited the fact that a periodic subwavelength grating acts as an effective birefringent retarder whose neutral axes correspond to the directions parallel and perpendicular to the wavevector of the gratings. With appropriate gratings patterns, they obtained polarization-dependent optical elements based on the Pancharatnam-Berry phase [61, 62].

To explain the principle at work in such space-variant optical elements, let us consider a transparent and locally uniaxial plate, whose in-plane orientation of

the optical axis is defined by the angle ψ formed with the x-axis (see Fig.1.11). Then we consider an incident plane wave of amplitude E_0, angular frequency ω, wavenumber k, and circular polarization $\mathbf{e}_\sigma$, described by the complex field

$$\boldsymbol{E}_{\text{in}} = E_0 e^{i(kz-\omega t)} \mathbf{e}_\sigma. \tag{1.22}$$

The light field at the output facet of the plate (whose input facet defines the origin $z = 0$) is obtained, neglecting diffraction inside the space-variant material, from the Jones formalism. Namely,

$$\boldsymbol{E}_{\text{out}} = \hat{J} \boldsymbol{E}_{\text{in}}, \tag{1.23}$$

where $\hat{J}$ is the Jones matrix describing the space-variant modifications of the polarization state as light passes through the plate. Its expression is given by

$$\hat{J} = \hat{R}(-\psi)\hat{P}\hat{R}(\psi), \tag{1.24}$$

where

$$\hat{R}(\psi) = \begin{pmatrix} \cos\psi & \sin\psi \\ -\sin\psi & \cos\psi \end{pmatrix} \tag{1.25}$$

is the rotation matrix around the z axis by an angle ψ, and

$$\hat{P} = \begin{pmatrix} e^{ikn_\parallel L} & 0 \\ 0 & e^{ikn_\perp L} \end{pmatrix} \tag{1.26}$$

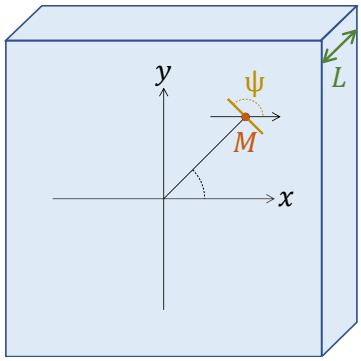

Figure 1.11: *Diagram of a plate made of locally-uniaxial birefringent material of thickness L. Orientation of the optical axis in the plane of the plate is defined at the point M by the angle ψ.*

is the propagation matrix through the plate, where $n_{\parallel}$ and $n_{\perp}$ are respectively, the refractive indices parallel and perpendicular to the optical axis, and L is the thickness of the plate. By introducing the phase delay associated with the birefringent phase retardation, $\Delta = k(n_{\parallel} - n_{\perp})L$, we obtain after calculations

$$\boldsymbol{E}_{\text{out}} = E_0 e^{-i\omega t} e^{ikn_{\perp}L} e^{i\frac{\Delta}{2}} \left[\cos\left(\frac{\Delta}{2}\right)\mathbf{e}_{\sigma} + i \sin\left(\frac{\Delta}{2}\right) e^{i2\sigma\psi}\mathbf{e}_{-\sigma} \right]. \tag{1.27}$$

The output component of the light field having orthogonal polarization state with respect to that of the incident light is therefore endowed by a spin-dependent space-variant phase profile directly dictated by the anisotropy patterning of the plate. In particular, when $\Delta = \pi$, only the spatially modulated light-component survives. Namely,

$$\boldsymbol{E}_{\text{out}} = -E_0 e^{-i\omega t} e^{ikn_{\perp}L} e^{i2\sigma\psi}\mathbf{e}_{-\sigma}. \tag{1.28}$$

Two kinds of space-variant profiles for ψ are specifically discussed hereafter, they correspond to situations that have been exploited in this thesis.

1.4.2 1D rectilinear distribution of the optical axis

Here, the orientation of the anisotropy axis change linearly with one of the Cartesian coordinates, say x. Namely,

$$\psi(x) = \pm\frac{2\pi}{\Lambda}x + \psi(0). \tag{1.29}$$

where $\Lambda/2$ is the spatial period of the element along x-axis. In this case, when $\Delta = \pi$ an incident circularly-polarized light is converted into light with opposite helicity and acquires a one-dimensional helicity-dependent geometric-phase constant gradient [59, 63]. This geometric phase gradient corresponds to the effect of an helicity-dependent prism producing a helicity-dependent transverse component for the linear momentum of light. In other words, the structure deflects right- and left-handed polarized beams in opposite directions as illustrated in Fig.1.12 that shows the simulated far field for an incident circularly polarized Gaussian beam. Taking into account that the material spatial period of the transverse-periodic distribution is $\Lambda/2$ and considering the half-wave plate condition $\Delta = \pi$, the deflection angle α equals the diffraction angle of a sinusoidal phase grating with period $\Lambda/2$.

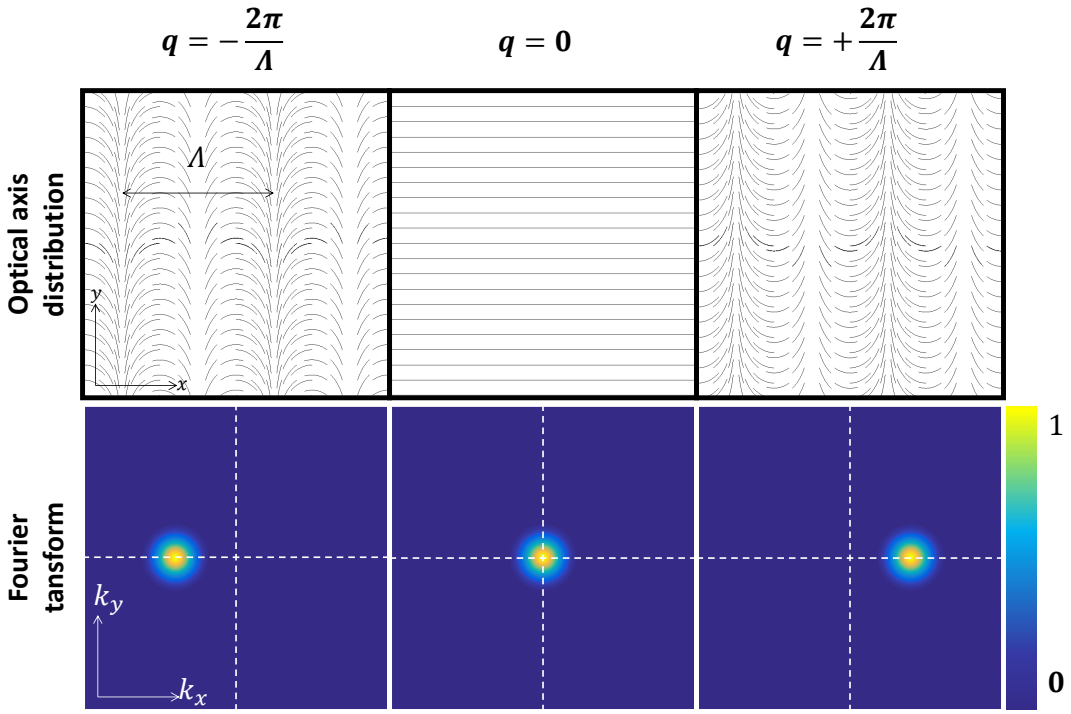

Figure 1.12: *In-plane distributions of the optical axis orientation in a locally-uniaxial plate. First row corresponds to the optical axis linear distribution* $\psi(x) = qx$*. Second row corresponds to far field normalized intensity distribution (calculated by Fourier transform) for left-handed circularly-polarized incident Gaussian beam assuming a uniform birefringent phase retardation of* π*.*

Namely,

$$\alpha = \arcsin\left(\frac{\lambda}{\Lambda/2}\right). \tag{1.30}$$

From a mechanical point of view, such samples allows spin-controlled lateral forces, which will be discussed in details in Chap.2

1.4.3 Azimuthal distribution of the optical axis

Here, the orientation of the anisotropy axis changes linearly with the azimuthal angle of the cylindrical coordinates. Namely,

$$\psi(\varphi) = q\varphi + \psi(0). \tag{1.31}$$

In that case, when $\Delta = \pi$, the transmitted beam is a vortex beam with topological charge $\ell = 2\sigma q$ when q is an integer or half-integer [60, 64] (see Fig.1.13). Such azimuthal anisotropic structures (often called q-plates) have become a popular way to generate vortex beams. Here, we will use such samples to implement the direct experimental observation of the mechanical consequences of left-handed vs. right-handed optical torque, as discussed in details in Chap.2.

1.5 Proposal of spin-driven optomechanics

In this chapter, we have described the mechanical principles (Sec.1.1) from the point of view of the analogy between the displacement and rotation. Then, we have reviewed the optics (Sec.1.2) in order to define the main features of light used in this manuscript. From the optomechanics principles (Sec.1.3) we introduced the concept of what we call 'unconventional' effects, namely, lateral forces and left-handed torques. Finally, we focused on spin-orbit interaction of light that is the key ingredient of the present thesis.

In this work, we propose to design and realize experiments based on the spin-orbit interaction that allow us to directly detect and measure 'lateral forces' using the approach described in Sec.1.4.2 and 'left-handed torques' using the approach described in Sec.1.4.3. By doing so, we aim at going further than previous demonstrations of helicity-controlled unusual effects [46, 65]. Indeed, using linearly and azimuthaly structured anisotropic media we propose to control the generation of lateral forces and left-handed torques, respectively. The encountered fabrication and optical manipulation challenges and optimization strategies will be discussed. In particular, we will treat the macroscopic case (cm-sized systems) in Chap.2 while the microscopic case (tens of µm-sized systems) is presented in Chap.3. Our results illustrate how spin-orbit optics can be used to experimentally unveil, in a 'simple' manner non-trivial phenomena that were, so far, restricted to subtle physical processes and highly demanding instrumentation.

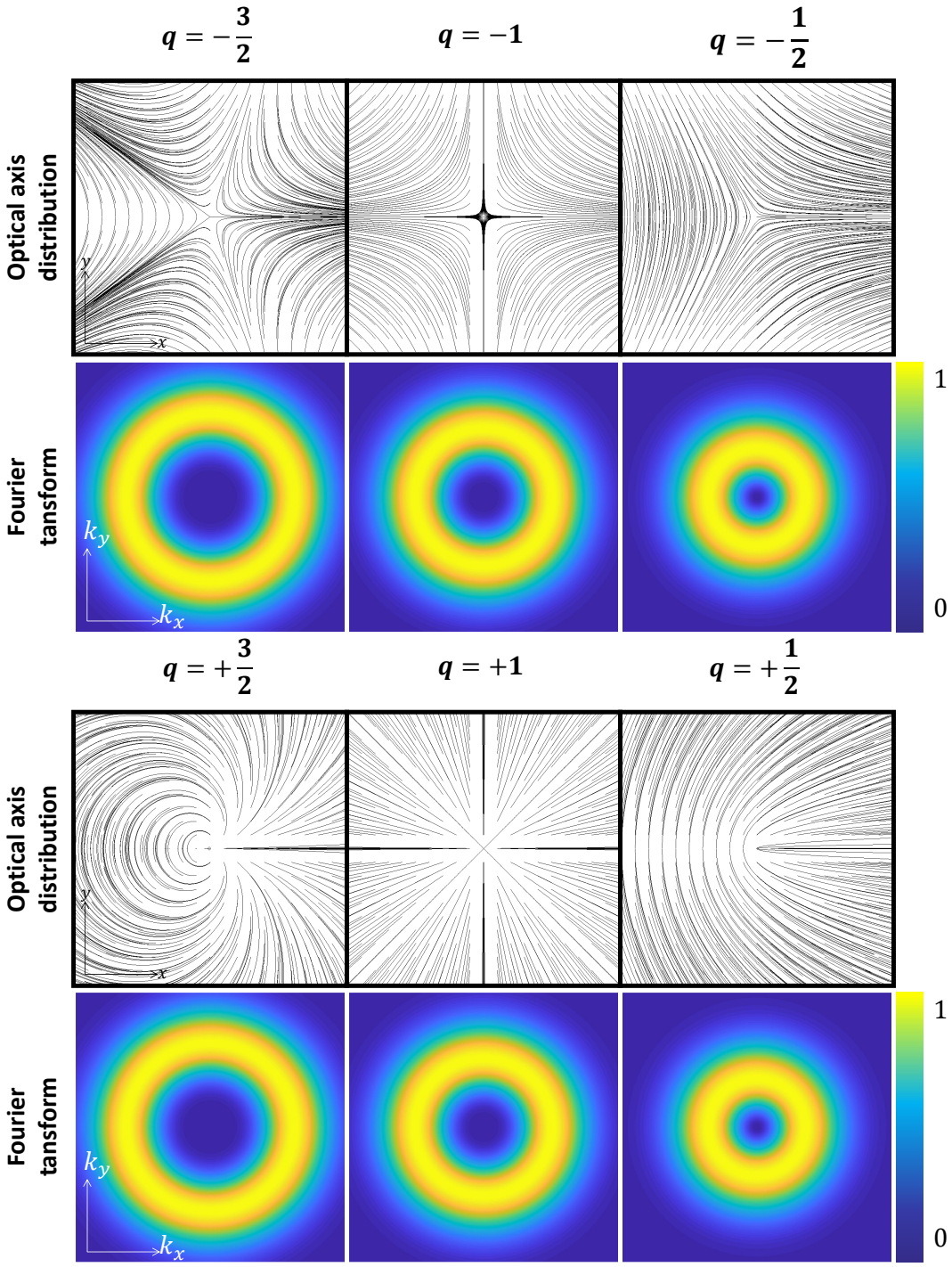

Figure 1.13: *In-plane distributions of the optical axis orientation in a locally-uniaxial plate. First row corresponds to the optical axis azimuthal distribution* $\psi(\varphi) = q\varphi$. *Second row corresponds to far field normalized intensity distribution (calculated by Fourier transform) for left-handed circularly-polarized incident Gaussian beam assuming a uniform birefringent phase retardation of* π.

CHAPTER 2

Macroscopic direct observation of optical spin-dependent lateral forces and left-handed torques

In the preceding chapter, we made a general introduction where our proposal to directly observe the manifestation of (i) lateral forces and (ii) left-handed torques is introduced. Here, we report on their direct experimental observations at macroscopic scale. In Sec.2.1 we present quantitative estimations of both phenomena and discuss the feasibility of experimental demonstrations by evaluating the optical performance of ideal systems. Our experimental attempts with millimeter-scale glass samples with a linearly variant birefringence for lateral forces and azimuthally variant birefringence for left-handed torques are reported in Sec.2.2. There, we start from the preliminary results obtained in our group in the case of torques before I started my thesis work [65], and then our new proposals are presented, and we also report on the case of lateral forces. Encountered difficulties led us to define and use other kind of material systems with respect to those originally used in previous works, which are based on nanostructured silica samples. Namely, we eventually use patterned polymerized liquid-crystal films, whose advantages are described in Sec.2.3. In Sec.2.4, we report on the full study of lateral forces and, in Sec.2.5 we report on left-handed torques.

2.1 Estimations and experimental approaches

Before presenting the experimental approach, we estimate the magnitude of the lateral force and the left-handed torque that we could ideally reach in practice.

In Sec.1.4 we introduced the concept of spin-orbit interaction which allows us to control the phase spatial distribution of the transmitted light by design using space-variant orientation of the anisotropy axis (ψ). Since linear patterns, Eq.(1.29), imply change in the transverse linear momentum and azimuthal patterns, Eq.(1.31), imply change in the total angular momentum, both sought-after optomechanical effects are a priori accessible with appropriately structured optically anisotropic elements. Hereafter we discuss the case of ideal samples consisting of space-variant half-waveplate with either rectilinear or azimuthal distribution of the optical axis.

2.1.1 Rectilinearly varying half-waveplate samples

2.1.1.1 General considerations

Let us consider a system as depicted in Figs.2.1. It consists of a lossless dielectric slab behaving as a half-waveplate having its optical axis varying along one direction, according to Eq.(1.29), which works as a polarization grating. Choosing the condition $\Delta = \pi$ ensures maximal polarization conversion efficiency. In that case, an incident light beam is fully deflected into the first diffraction orders of the grating. Each circularly polarized component of the incident light is deflected in a distinct direction whose angle α is given by Eq.(1.30). Then, the balance of linear momentum, see Eqs.(1.18) and (1.19), leads to the following expression for the lateral force in the case of a beam with power P and reduced third stokes parameter s_3:

$$F_{\perp,\mathrm{opt}} = s_3 \frac{2\lambda}{\Lambda} \frac{P}{c}. \tag{2.1}$$

Note that since $\boldsymbol{J}^{\mathrm{out}} - \boldsymbol{J}^{\mathrm{in}} \neq \boldsymbol{0}$, a net torque is also exerted on the object, however, the lateral force is independent of it. In addition, there is also a force component along the propagation direction of the incident beam. The experimental detection of the lateral force will therefore have to manage with those additional optomechanical contributions.

The experimental feasibility primarily relies on our ability to have as small as possible period Λ for the material structuring and as large as possible optical

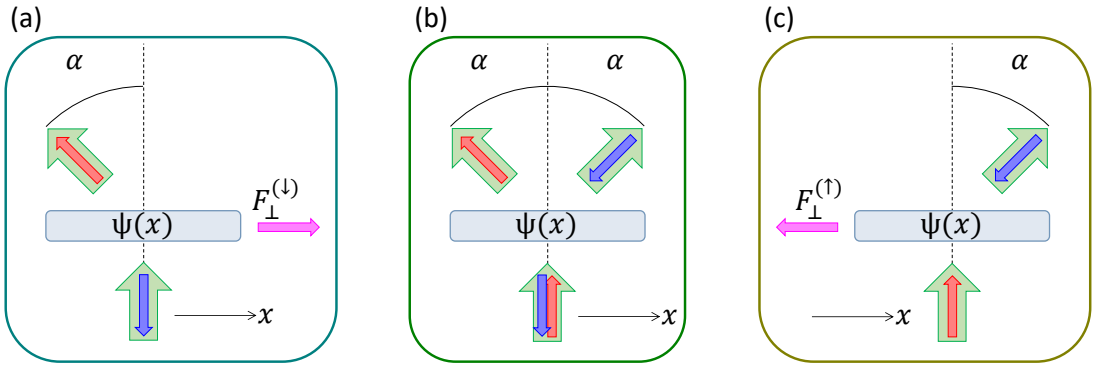

Figure 2.1: *Spin-dependent beam steering associated with the deflection angle α (ref. [59]) of the transmitted photons for half-waveplate with sinusoidally varying optical axis orientation along the x-axis, $\psi(x)$. This leads to spin-dependent lateral optical forces $\boldsymbol{F}_\perp^{(\uparrow,\downarrow)}$ with opposite direction and the same magnitude for incident spin up $(\uparrow)$ and down $(\downarrow)$ (c,a) which respectively refer to left-handed and right-handed circularly polarized light and no net lateral force for incident linearly polarized light carrying equal-weight fractions of spin up and down photons (b).*

power P. Regarding accessible power, we could reach up to $P_{\max} \sim 10$ W with $\lambda = 532$ nm by using our laboratory laser resources. In Fig.2.2 we estimate the magnitude of lateral force as a function of the material period in the range $1\ \mu\text{m} \leqslant \Lambda \leqslant 10\ \mu\text{m}$, which corresponds to technologically accessible values, and the beam power in the range $0.1\ \text{W} \leqslant P \leqslant 10\ \text{W}$. It turns out that lateral forces of the order of a few nN is possible.

Next step involves the design of the experiment, where new estimations are performed in order to anticipate the level of the experimental challenge regarding the detection of the mechanical effects.

2.1.1.2 Design of the lateral force experiment

Ideally, we look for a system enabling freely moving sample along the grating direction only. To achieve this, an air-liquid interface or a liquid-liquid interface, on which could be deposited the structured slab, are natural candidates. In practice, an appropriate design allows restricting the motion of the object only along the direction of interest. This is done by using a rectangular container

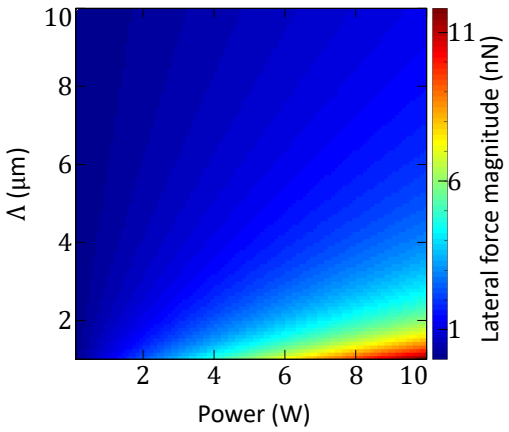

Figure 2.2: *Estimation, in the ideal case, of the magnitude of the lateral optical force ($|F_{\perp,\mathrm{opt}}|$) as a function of power (P) and the material periodicity (Λ) considering the light-matter interaction geometry depicted in Fig.2.1.*

(pool) of Plexiglas, see Fig2.3(a). In such pool, it is possible to tailor either a liquid-liquid interface or a liquid-air interface. This design allows bearing an object owing to interfacial surface tension and constraining its motion into 1D translation owing to anisotropic geometry. The interface is obtained by filling the trench of the rectangular pool with a liquid, taking care to fix the solid–liquid–gas contact line at the rim of the trench. Then, the object is placed on the air/liquid interface. Then, by slightly removing fluid starting from a fully filled trench, the interface acquires two main menisci along x and y, see Figs.2.3(b,c). By using a rectangular slab, self-alignment is obtained, x being the easy direction of motion. For optical manipulation at liquid-liquid interface, a second liquid is poured into the pool soon after the object is placed at the interface.

2.1.1.3 Experimental feasibility of the lateral force experiment

According to the experimental setup proposed in Fig.2.3(d), here we evaluate the expected typical light-induced velocity v_0 accounting for the balance between the optical lateral force and the viscous drag force. For this purpose, we consider that the rectangular sample is placed at air/water interface and we assume no restoring effects from the meniscus along the long axis of the pool. The light-

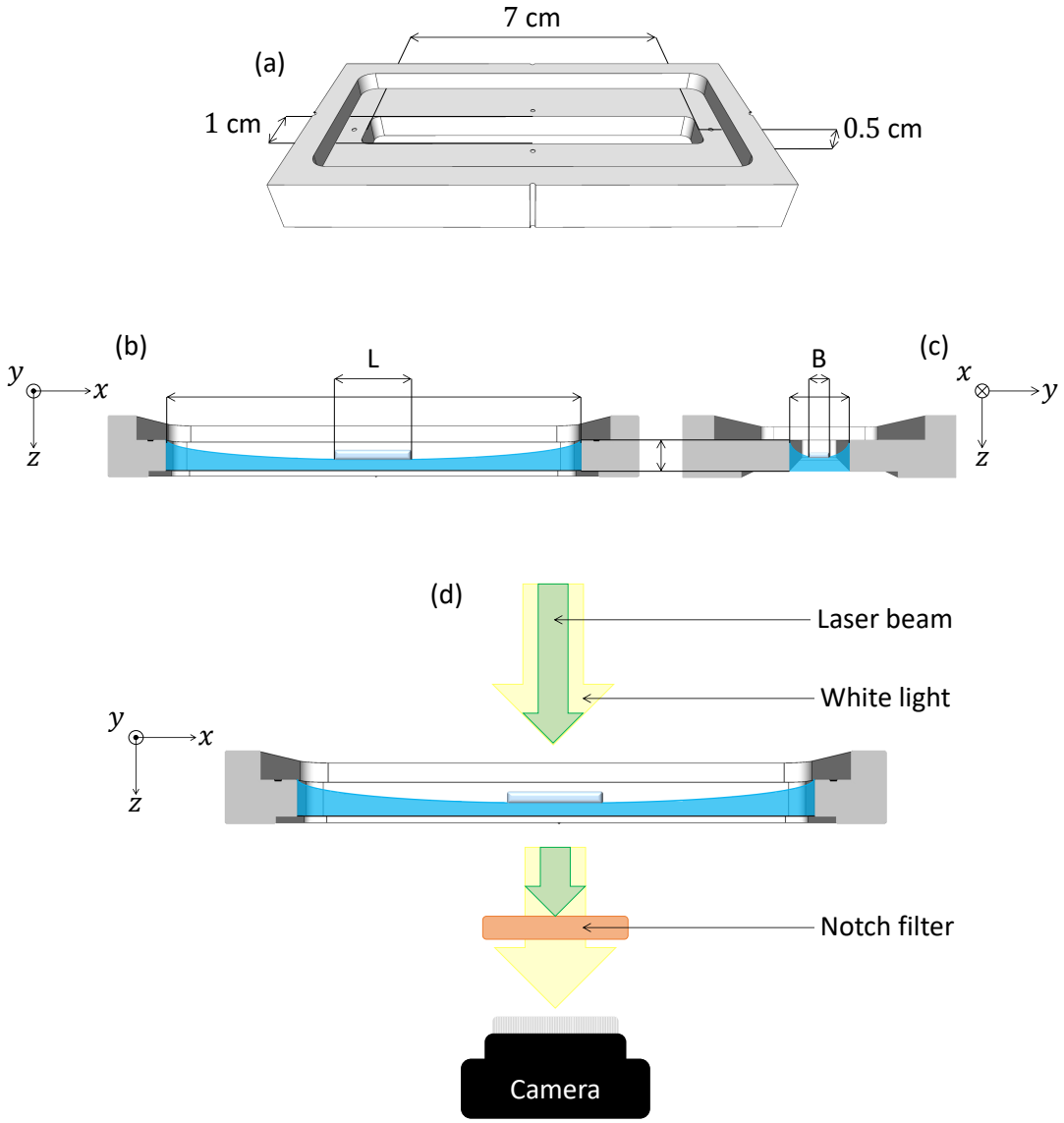

Figure 2.3: *System set for the lateral force experimental realization with linear symmetry. (a) Experimental rectangular-shaped Plexiglas pool designed for the lateral force experimental realization. The idea is to place a rectangular-shaped structured slab at an air/liquid (or liquid/liquid) interface in the trench of the pool, taking care to fix the solid–liquid–gas (or solid/liquid/liquid) contact line at the rim of the slightly under-filled pool. (b,c) The two main menisci, with different radii of curvature, thus ensuring capillary alignment and stable trapping of a rectangular sample in the centre of the pool. (c) Experimental setup: video recording system and pumping beam are depicted.*

induced constant translation velocity is thus obtained at steady state from the balance between (i) the optical radiation force, $\boldsymbol{F}_{\perp,\mathrm{opt}}$, driven by spin-orbit interaction of light and (ii) the viscous drag force, $\boldsymbol{F}_{\mathrm{visc}}$, exerted by the fluid surrounding the moving sample. Namely,

$$\boldsymbol{F}_{\perp,\mathrm{opt}} + \boldsymbol{F}_{\mathrm{visc}} = 0. \tag{2.2}$$

Considering an infinitely thin plate with dimensions B (width) and L (length), see Fig.2.3(b-c), and assuming the hydrodynamic Stokes approximation to be valid (i.e. inertial effects are discarded with respect to viscous ones), the magnitude of the viscous drag force is [66]:

$$F_{\mathrm{visc}} \sim \rho B L^{\frac{1}{2}} \nu^{\frac{1}{2}} v_0^{\frac{3}{2}}, \tag{2.3}$$

where ρ and ν are the density and the kinematic viscosity, of the fluid ($\rho \sim 1\ \mathrm{g\,cm^{-3}}$ and $\nu \sim 1\ \mathrm{mm^2\,s^{-1}}$, for water at 20 °C). Combining Eqs.(2.2), (2.3) and (2.4) one gets

$$v_0 \sim \omega^{-\frac{2}{3}} \Lambda^{-\frac{2}{3}} \rho^{-\frac{2}{3}} \nu^{-\frac{1}{3}} B^{-\frac{2}{3}} L^{-\frac{1}{3}} P^{\frac{2}{3}}. \tag{2.4}$$

According to this scaling, miniaturization is favorable but implies larger intensity values at fixed optical power, which implies in return some limitations. Indeed, we are limited in accessible power and undesired effects that can be expected at larger intensities. For instance, thermal effects could trigger additional physical phenomena such as Marangoni flows or thermal damage of the material. For a plate with dimensions $B = 1$ mm and $L = 5$ mm, experiencing a optical lateral force $F_{\perp,\mathrm{opt}} = 1$ nN, we expect to observe a $v_0 \sim 1\ \mathrm{mm\,s^{-1}}$, which sounds accessible for measurements.

2.1.2 Azimuthally varying half-waveplate samples

2.1.2.1 General considerations

Similarly to the previous section, we consider systems as depicted in Figs.2.4, which consists of space variant half-waveplate having azimuthally varying optical axis orientation according to the Eq.(1.31). For an incident circularly polarized Gaussian beam, the total angular momentum output includes an orbital

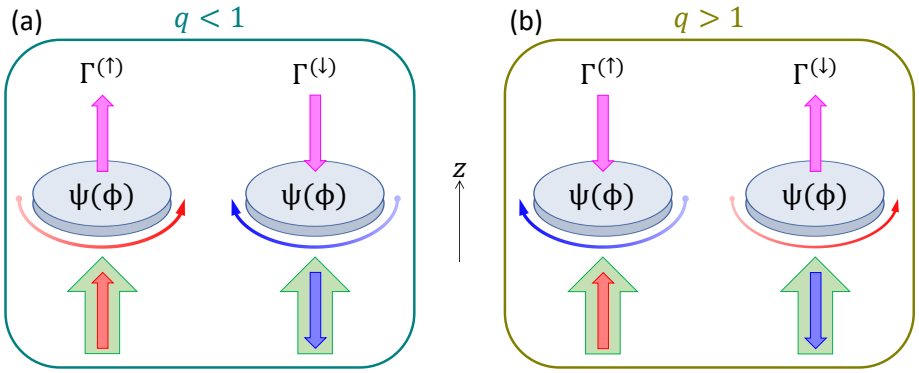

Figure 2.4: *Principle of optical radiation torque for right- and left-handed. In (a), an object subjected to the application of a usual optical torque ('right-handed') controlled by the spin angular momentum of the light, the object tends to rotate in the same direction as the incident angular momentum; therefore, the spin and the torque are parallels. In (b), the reverse situation corresponds to a manifestation of unconventional optical torque ('left-handed'); therefore, the spin and the torque are anti-parallels.*

part as a result of the spin-orbit interaction. In other words, the output is a contra-circularly polarized vortex light according to the Eq.(1.28). The angular momentum changes as light passes through the optical element is summarized as follows when considering the projection of the total angular momentum along the propagation axis z:

$$\underbrace{j_z^{\text{in}} = \sigma\hbar}_{\text{(Spin part only)}} \longrightarrow \overbrace{j_z^{\text{out}} = -\sigma\hbar + 2\sigma q\hbar}^{\text{(Spin + Orbital parts)}}. \tag{2.5}$$

From the left-handed torque condition, Eq.(1.21), we obtain

$$j_z^{\text{in}}\Gamma_{z,\text{opt}} < 0 \quad \longrightarrow \quad \sigma\Gamma_{z,\text{opt}} < 0. \tag{2.6}$$

Then, inserting the previous equations in Eq.(1.18) we get

$$\sigma\Gamma_{z,\text{opt}} = (\hbar - \sigma j_z^{\text{out}})\frac{dN}{dt} < 0 \quad \longrightarrow \quad \sigma j_z^{\text{out}} > \hbar, \tag{2.7}$$

which implies $q > 1$ and the general expression of the optical torque is given by

$$\Gamma_{z,\text{opt}} = 2\sigma(1-q)\frac{P}{\omega}. \tag{2.8}$$

Assuming a disk of radius R characterized by $q = 100$ and mass M in free space experiencing a torque from an incident beam with power P, it is set into rotation at angular frequency $\Omega(t)$ satisfying the relationship:

$$\Gamma_{z,\text{opt}} = \frac{1}{2} M R^2 \frac{d\Omega}{dt}. \tag{2.9}$$

Therefore, considering initially the disk at rest, one gets

$$\Omega(t) \sim \omega^{-1} M^{-1} R^{-2} q P t. \tag{2.10}$$

Again, next step involve the design of the experiment, where estimations are performed in order to evaluate feasibility of an experiment before implementing it.

2.1.2.2 Design of the left-handed torque experiment

In Sec.2.1.1.2, we concluded that an air-liquid interface or a liquid-liquid interface is a suitable choice in practice. Here we propose to use the same approach, but with the aim at observing a rotational motion, implying the use of a circular shaped pool. In Fig.2.5(a-b) we show the design of the circular Plexiglas pool, where it is possible to tailor either a liquid-liquid interface or a liquid-air interface. Here, a disk-shaped object will therefore be self-centered by capillary effect, though being free to rotate around the z axis.

2.1.2.3 Experimental feasibility of the left-handed torque experiment

Experimental setup proposed for left-handed torque is depicted in Fig.2.5(c). To evaluate the mechanical consequences of the viscous torque, we assume that the sample is placed at air/water interface and is free to rotate. At the steady state, the light induces a constant rotation rate to the sample that can be determined from the balance between (i) the optical radiation torque $\mathbf{\Gamma}_{z,\text{opt}}$ driven by spin-orbit interaction of light and (ii) the viscous torque $\mathbf{\Gamma}_{\text{visc}}$ exerted by the fluid surrounding the rotating sample. Namely,

$$\mathbf{\Gamma}_{z,\text{opt}} + \mathbf{\Gamma}_{\text{visc}} = 0. \tag{2.11}$$

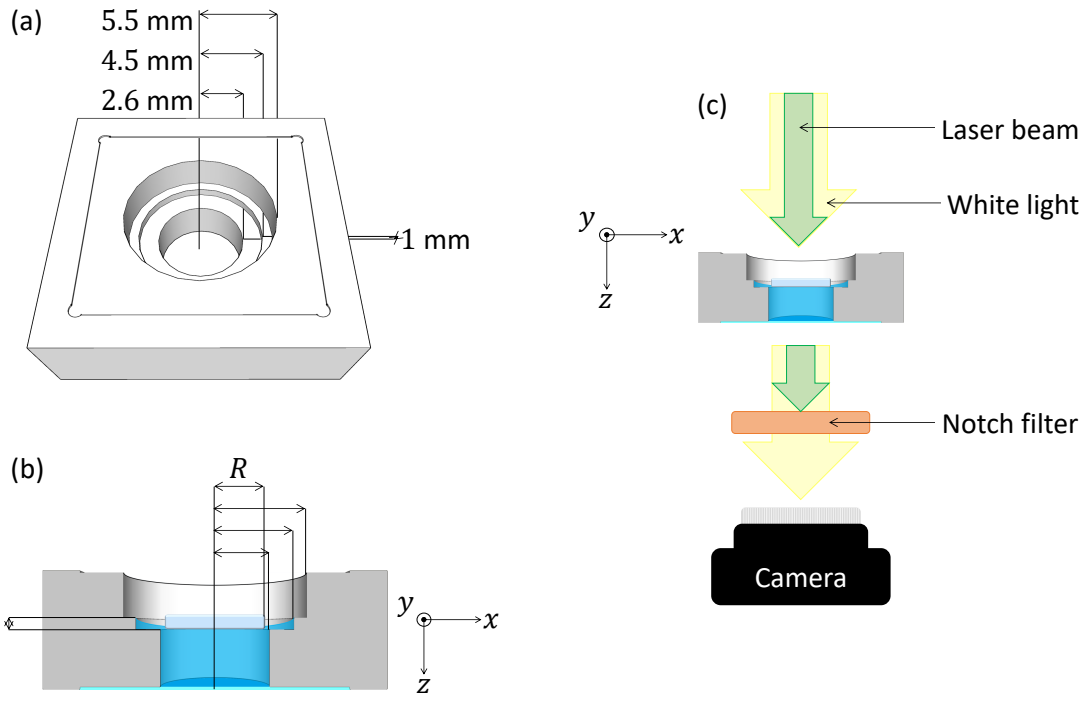

Figure 2.5: *System set for the left-handed torque experimental realization with azimuthal symmetry. (a) Three concentric circular-steps pool of Plexiglas. (b) The sample is placed at an air–water interface in the pool, taking care to fix the solid–liquid–gas contact line at the rim of the slightly under-filled pool. (c) Experimental setup: video recording system and pumping beam are depicted.*

Considering an infinitely thin disk of radius R half-immersed in water and the Stokes approximation the viscous torque expression is [66]:

$$\Gamma_{\text{visc}} = \frac{16}{3}\rho\nu R^3 2\pi f_0, \tag{2.12}$$

where f_0 is the steady rotation frequency. Combining Eqs.(2.8) and (2.12) we obtain the following scaling for the notation frequency:

$$f_0 \sim \rho^{-1}\nu^{-1}R^{-3}q\omega^{-1}P. \tag{2.13}$$

Similar practical considerations as discussed in the last paragraph of the Sec.2.1.1.3 also apply here. Hence, for a disk of dimensions R = 3 mm and q = 100, illuminated by a beam with power P = 10 W, we expect to observe a $f_0 \sim$ 10 mHz, which encourages experimental investigations.

2.2 Nanostructured silica glass slabs

2.2.1 Presentation of the samples

Our first choice was motivated by the use of a material that could sustain high irradiation power, hence optimizing the chances to observe the desired optomechanical effects. Specifically, we explored the use of nanostructured silica glass slabs whose technology is nowadays well-established. The principle consists in the direct laser writing of self-assembled nanogratings owing to femtosecond laser pulses [67], see Fig.2.6. Such structuring correspond to subwavelength gratings for the visible light, hence endowing matter with form birefringence. By adjusting the writing beam polarization state (which controls ψ) and intensity (which controls Δ), arbitrary space-variant anisotropic patterns can be fabricated.

In our case, a compromise between technical realization capabilities and a first experimental implementations led us to design a set of 1D half-waveplates gratings (for λ = 532 nm wavelength) written in parallelepipeds, see Fig.2.7, of $\Lambda = \{20\ \mu m, 40\ \mu m, 60\ \mu m\}$, a mass m = 22 mg, dimensions $(L \times B \times H)$ 5 mm × 2 mm × 1 mm, and a structured volume of $(l \times b \times h)$ 4.5 mm × 1.6 mm × 74 µm.

Similarly, we opted for a set of optical disks with azimuthal patterning characterized by $q = \{10, 25, 50, 75, 100\}$, a mass m = 196 mg, diameter of $2R$ = 5 mm, thickness of H = 1 mm, and a structured volume written with a thickness of h = 74 µm in between of two concentric circles of $2R_{min}$ = 250 µm, $2R_{max}$ = 4.5 mm, see Fig.2.8. The samples have been fabricated by Altechna R&D company.

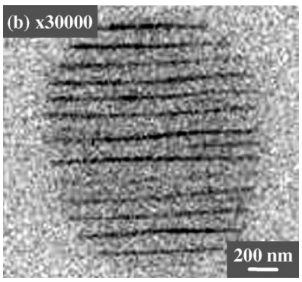

Figure 2.6: *Example of a nanostructured silica glass. Here is shown a SEM image taken from [67], where the authors present 'fingerprints' left in the sample after direct femtosecond laser writing process.*

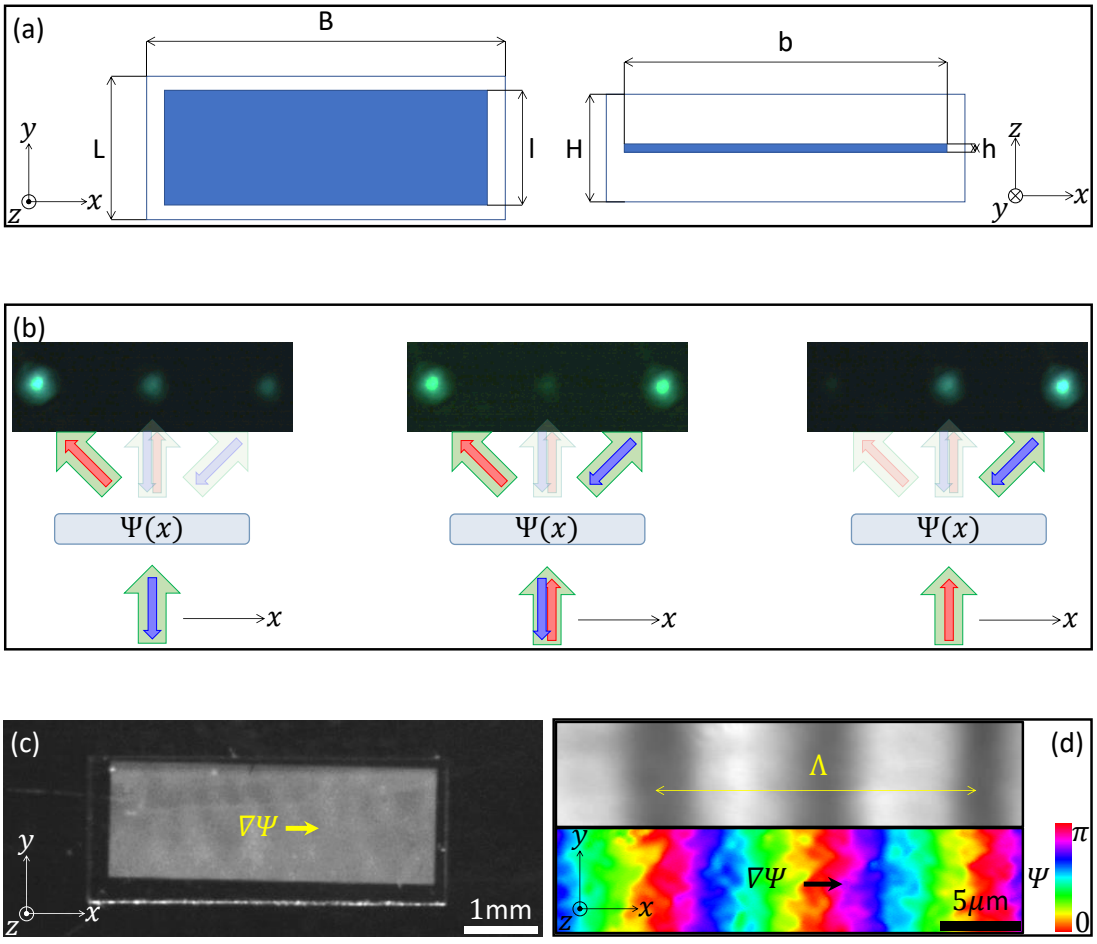

Figure 2.7: *Nanostructured silica glass parallelepipeds. (a) Our set of samples consist of three parallelepipeds of* $(L \times B \times H)$ 5 mm × 2 mm × 1 mm, *with a structured volume of* $(l \times b \times h)$ 4.5 mm × 1.6 mm × 74 µm. *(b) Actual diffraction patterns for three polarization states of light: right-handed circular (blue), linear (blue and red), and left-handed circular (red). (c) Actual sample of* Λ = 20 µm *where the nanostructured volume is visible due to substantial light scattering in the visible domain. (d) The images corresponds to the same section of the sample; top: the sample is observed under crossed linear polarizers; bottom: birefringent optical imaging reveals the one-dimensional periodic modulation of the optical axis orientation angle in the plane of the sample, here* $\psi = 2\pi x/\Lambda$.

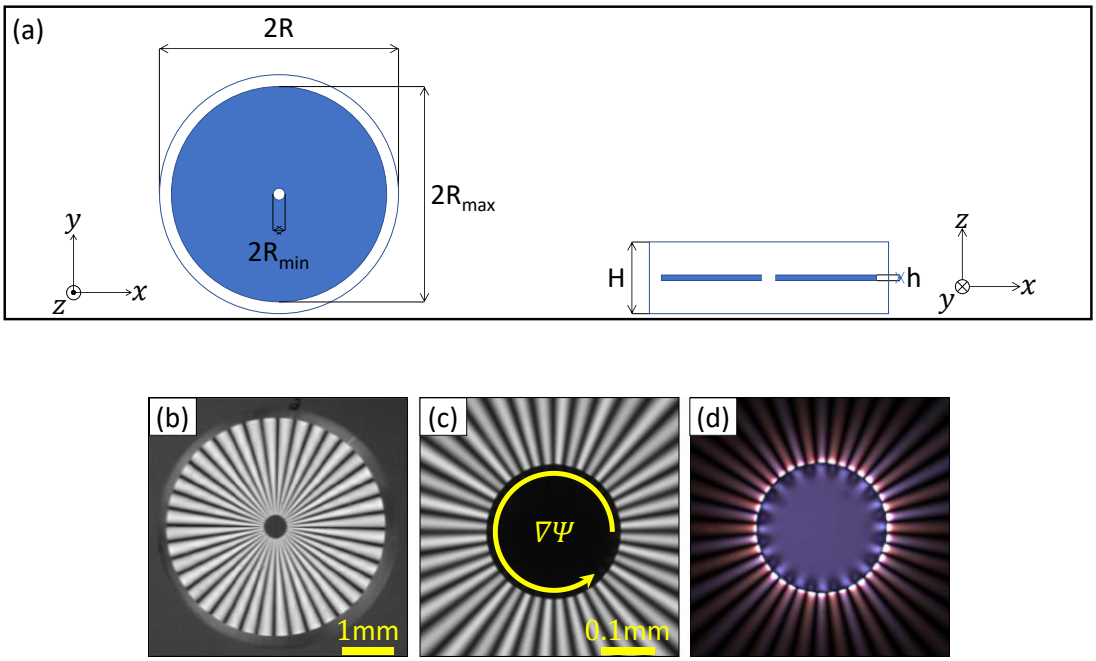

Figure 2.8: *Nanostructured silica glass disks. (a) Our set of samples consist in five disks with diameter of* $2R$ = 5mm, *a thickness of* H = 1mm, *with a structured volume written with a thickness of* h = 74µm *in between of two concentric circles of* $2R_{min}$ = 250µm *and* $2R_{max}$ = 4.5mm. *(b-d) These images are taken from [65]: (b) example of observation between crossed linear polarizers for* q = 10, *where it shows an azimuthal periodic modulation of the optical axis orientation angle in the plane of the sample, here* $\psi = q\varphi$. *(c) Sample zoomed at the central part, and (d) inner circle tensions distribution unveiled by adjusting the incident polarization angle and the camera exposure.*

2.2.2 Optomechanical experimental attempt

2.2.2.1 Lateral force experiments

The experiment is prepared according to the protocol described in Sec.2.1.1.2, leading to a self-alignment of the rectangular slab having its grating wave vector aligned with the larger side of the rectangular trench of the pool.

A Gaussian laser beam at λ = 532 nm, having a waist of w_0 = 0.3 mm at

the sample location, is used to irradiate the sample according to sketch shown in Fig.2.3(d). The displacement δx of the sample from the situation at rest is monitored by video recording, for left/right-handed circular and linear incident polarization states. Experiments are repeated for a set of incident power from 0.2 W to 1 W by 0.1 W. The results are collected in Fig.2.9 and the summary of our observations is the following:

- A lateral displacement of the sample is observed as a consequence of the action of the light on it.
- No clear dependence on the incident polarization state is found.

We thus conclude that our observations are not associated with the effect we are searching for. Possible drawbacks at work are the effects of light-induced flows as a result of residual absorption of the sample that could arise from uncontrolled temperature gradients. Indeed, it is known that temperature gradient and ensuing Marangoni flows for an object placed at air/fluid interface can generate motion [68]. Also we suspect effects from the substantial and possibly non-uniform light scattering of the sample, see Fig.2.12(a). Indeed, any broken symmetry resulting from the scattering along the x axis will induce lateral motion. However, the reversal of the direction of displacement with power at fixed incident polarization state remains a strong signature of a phenomenon that cannot be explained on simple grounds.

2.2.2.2 Optical torque experiments

Here we use the setup shown in Fig.2.5(c) using an incident Gaussian beam with waist $w_0 = R_{\max}$, see Fig.2.8(a), and a power of 5 W was used. No motion was observed, which led us to redesign the experimental system. Various options have been tested with the hope to get rid of possible unwanted and uncontrolled contact line at the rim of the disk. The three investigated approaches are illustrated in Fig.2.10. The situation of Fig.2.10(d) turned out to be a non-stable equilibrium configuration, i.e., the sample was misaligned with any perturbation. The cases that correspond to Figs.2.10(a) and (b) were both tested under 3 h illumination.

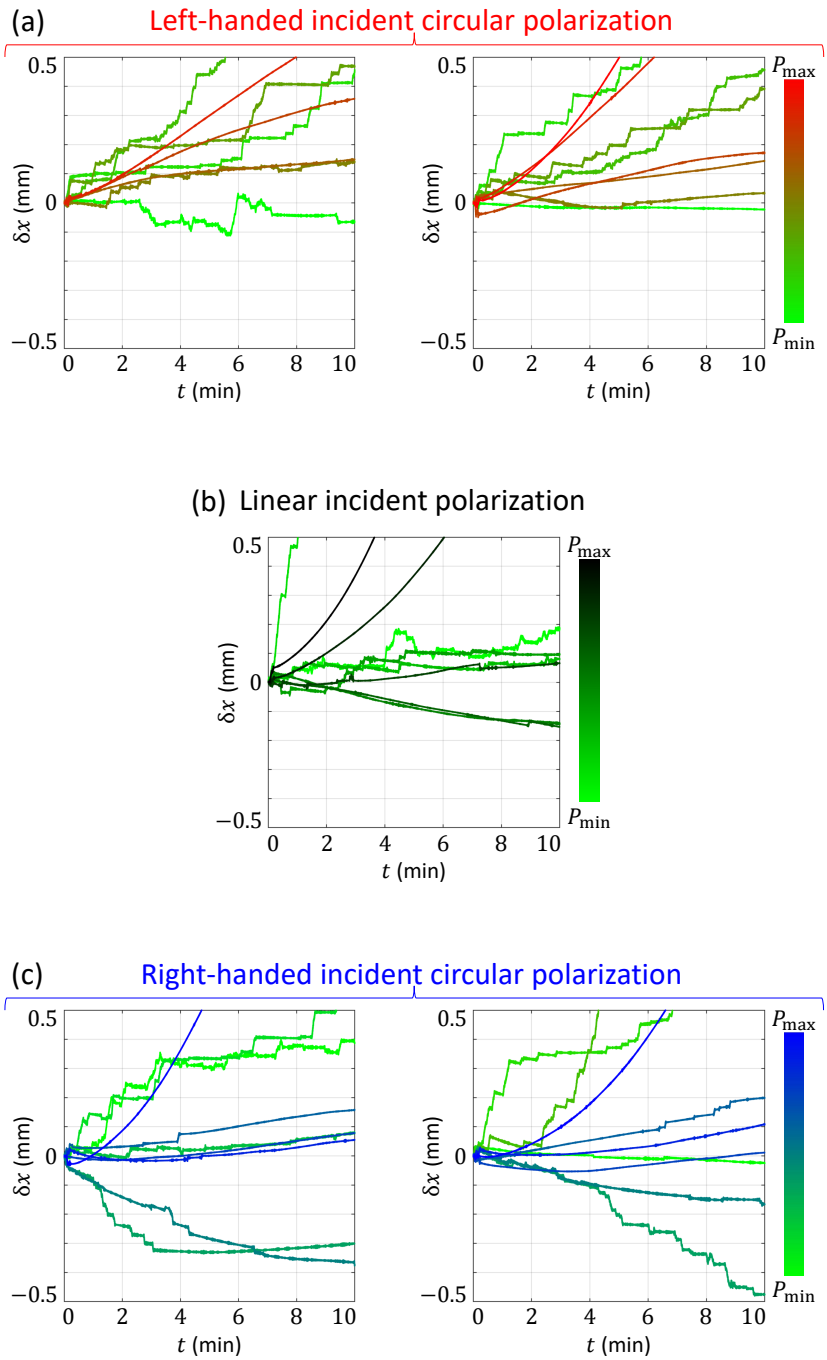

Figure 2.9: *Data plots of displacement (δx) vs. time (t) as a function of the beam power (P) and beam polarization. The applied beam power runs from* 0.1 W *to* 1 W *with (a) left-handed circular polarization (two sets of experiments), (b) linear polarization (one sets of experiments), and (c) right-handed circular polarization (two sets of experiments).*

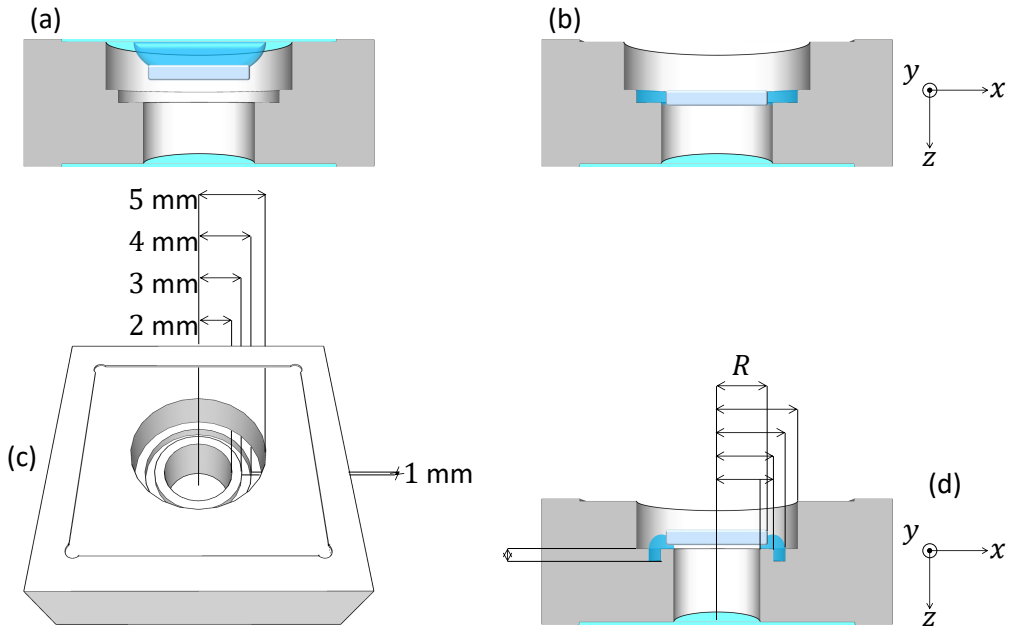

Figure 2.10: *Alternative systems tested for the left-handed torque experimental realization in order to reduce the viscous torque. (a) A liquid droplet is placed at a cover-slip to hold the disk by capillarity. (b,d) The sample is held by a ring of water sealing an air chamber created in between a cover-slip at the bottom of the pool, the pool, and the disk itself. (c) New pool designed with a trench milled at the middle step for the system (d).*

- In the case of Fig.2.10(a), no angular displacement is observed towards any preferential direction that exceeded the noise level of our detection system.
- In the case of Fig.2.10(b), the formation of condensation drops below the plate cannot be avoided, which vividly recalls that thermal effects induced by light are actually at work. Essentially, this leads to the destabilization of the sample when the 'water ring' axisymmetry is affected by condensation.

From these negative results, we conclude that we have to explore another experimental approach. Since the ideal estimations discussed above are encouraging, we decided to focus on the definition of other materials achieving both better optical performance (i.e. less scattering, less residual absorption, smaller patterning spatial period) and less inertia. Our choice went to liquid crystal polymer technology, which is discussed in the next section.

2.3 Patterned polymer liquid crystal samples

Photo patterned polymer liquid crystal technology is used in the industry for a wide variety of spin-orbit based optical elements [69]. Here we opted for one-dimensional grating design identical to that use for lateral force experiments discussed above, made of patterned polymer liquid crystal layer of thickness $h \sim 2$ µm suitable to meet the condition of $\Delta = \pi$ for our wavelength $\lambda = 532$ nm. These structured thin films are lying on the top of a soft plastic substrate of thickness $H = 200$ µm. The samples were fabricated by Beam Co. company, and each element has a radius of $R = 5$ cm, and a grating period of $\Lambda = 4.6$ µm, see Fig.2.11.

The optical performance of this material in terms of light scattering is greatly reduced with respect to nanostructured glass. A qualitative comparison is shown in Fig.2.12(a), from which one can visually appreciate reduced residual scattering in the case of polymer liquid crystal samples. Moreover the spatial period of the grating, $\Lambda/2$, is reduced by four times, as one can see by comparing Fig.2.7 and Fig.2.12(b-c). This leads to four times larger lateral force magnitude for the same power since the deflection angle is four times larger, noting small angle approximation remains fairly valid.

Two kinds of objects are prepared from the same structured film. Namely, rectangular with dimensions 6 mm × 1 mm are hand-cut for lateral force

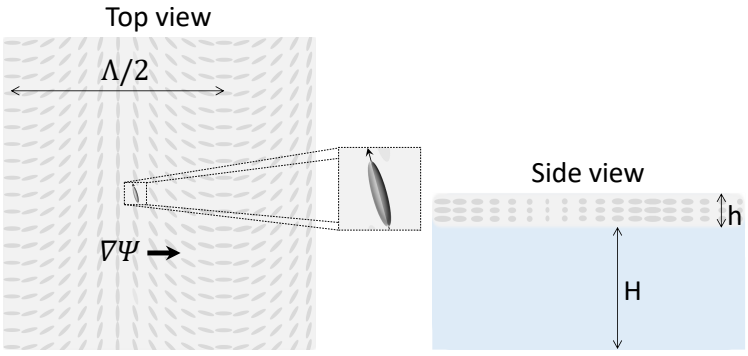

Figure 2.11: *Cycloidal birefringent grating patterned on a polymer liquid crystal layer lying on a soft plastic substrate. The polymer liquid crystal layer thickness is* h ~ 2µm*, that corresponds to* $\Delta \simeq \pi$ *at* $\lambda = 532$ nm*; the soft plastic substrate thickness is* H ~ 200µm.

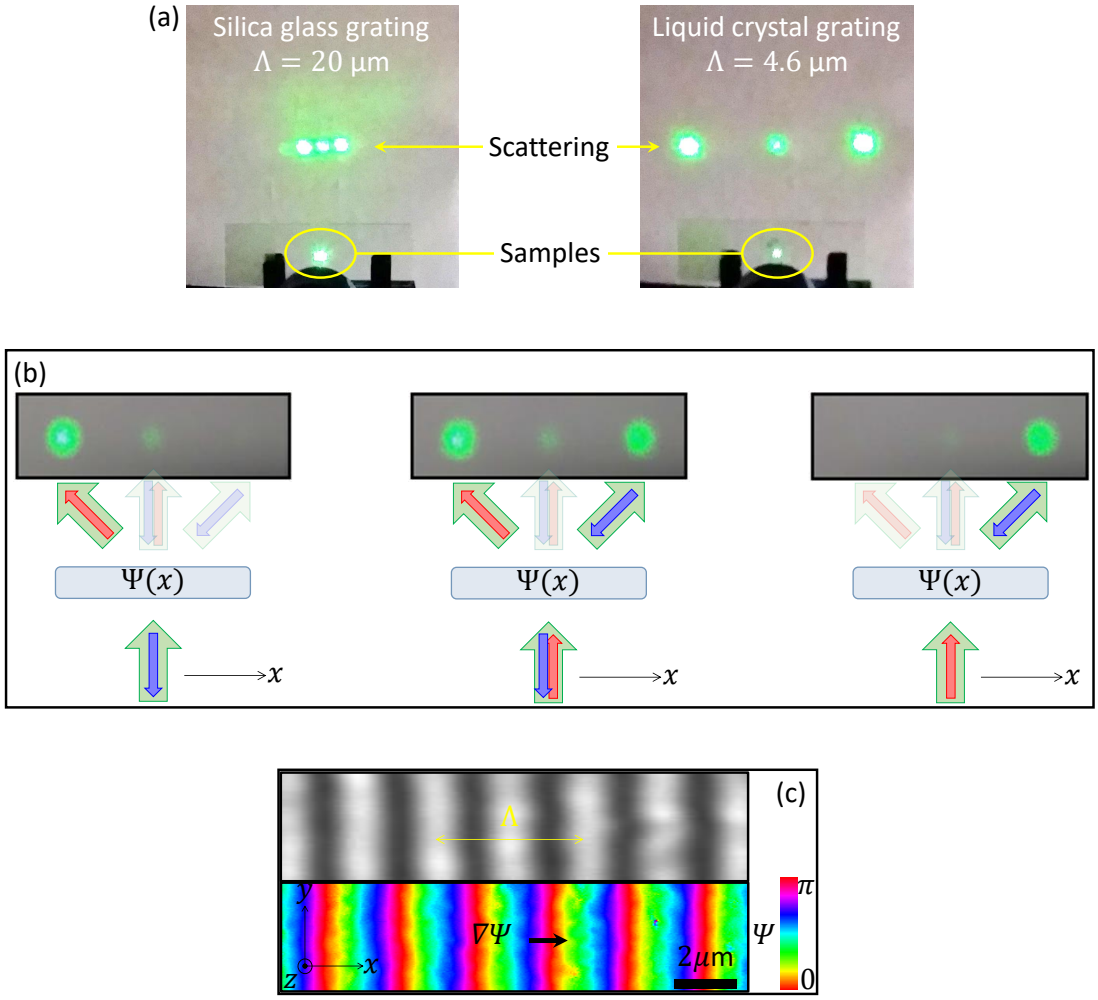

Figure 2.12: *(a) Comparison between the diffracted fields from gratings made of nanostructured glass and photopatterned polymer liquid crystals irradiated by a linearly polarized light Gaussian beam. The picture allows observing both the sample and the screen placed at a distance ~ 25 cm from the sample. (b,c) Optical characterization of the patterned polymer liquid crystal samples. (b) Actual diffraction patterns for three polarization states of light: right-handed circular (blue), linear (blue and red), and left-handed circular (red). (c) The images corresponds to the same section of the sample; top: the sample is observed under crossed linear polarizers; bottom: birefringent optical imaging reveals the one-dimensional periodic modulation of the optical axis orientation angle in the plane of the sample, here* $\psi = 2\pi x/\Lambda$.

experiments, see Fig.2.13(a). Effective circular-shaped azimuthally structured elements are obtained by assembling a discrete set of four right-angle circular sectors having different optical axis orientation. Recalling that cutting the plate by hand implies a low resolution in the cut, four sectors correspond in practice to our technical limit. The process is summarized in Fig.2.13(b-d).

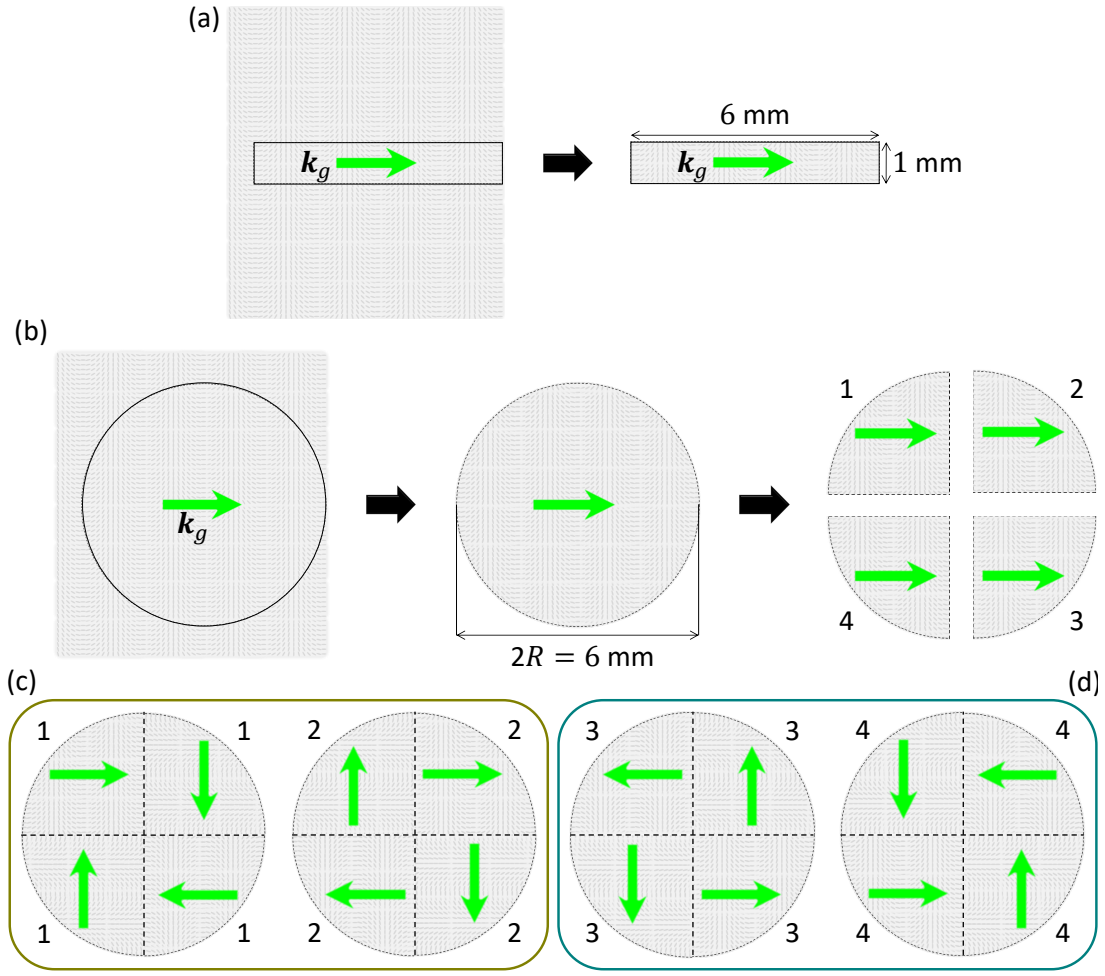

Figure 2.13: *(a) All rectangular plates are hand-cut in the same way, with the longest side parallel to the grating wavevector. (b-d) Assembling sectors of a polarization grating slab in order to obtain a effective azimuthal distribution of the optical axis. (b) The hand-cut process consist to cut four circular sectors from the 1D patterned film. (c) and (d) depict the clockwise and counter-clockwise arrangement of the grating wavevector* $\boldsymbol{k}_g$*, respectively.*

2.4 Lateral forces demonstration

We use the same experimental arrangement as the one used when dealing with nanostructured glass samples. The sample positioning protocol of the sample at the interface also worked with patterned liquid crystal samples, see Fig.2.14.

An additional advantage of this technological option is that we can easily perform several tests with different dimensions for the object simply by cutting the desired shaped from the initial large area sample.

2.4.1 Qualitative observations

At first we perform a set of four experiments consisting in a null experiment (no illumination), and three series of excitation-relaxation (illumination on-off) having a total duration $2t_{\text{off}}$, where t_{off} = 3 min is the time at which the light

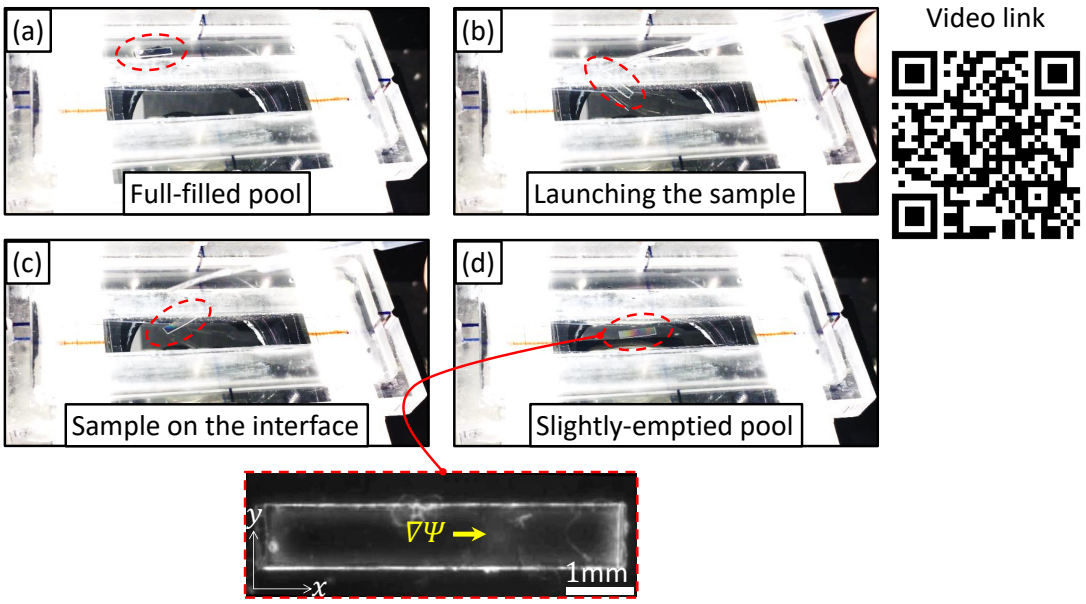

Figure 2.14: *Sample positioning protocol depicted in four frames extracted from the video that can be seen by scanning the provided QR code: (a) The pool is full-filled and the sample is placed on "the shore". (b) The sample is gently pushed with a pipette onto the air/water interface. (c) The floating sample slowly moves. (d) The sample eventually self-aligns owing to capillary effects as water is removed with the pipette.*

beam in switched off. The incident beam is a normally incident Gaussian beam of power $P \sim 1$ W, beam waist $w_0 = 0.45$ mm, wavelength $\lambda = 532$ nm. The used polarization states of the incident are right-handed circular (RH), linear, and left-handed circular (LH), see Fig.2.15.

Null experiment confirms the stability of the system, and defines the position at rest, which is fixed as the origin of the displacement, $x = 0$. Under RH and LH illumination, we observe displacement from the initial position, towards opposite equilibrium positions $\pm x_{\max}$. As the excitation beam is switched off, the object returns to the rest position. Finally, under linearly polarized light the object exhibits only slight deviation from the position at rest that depends on the sample. The latter observation validates the compensating mechanical contributions from the RH and LH components of the incident light field.

2.4.2 Modeling the translational dynamics

In the previous section, we qualitatively observed a Hookean behavior associated with a restoring force of a capillary nature associated to the curved air/water interface. Neglecting non-linear effects, dynamics can therefore be described quantitatively according to a one-dimensional linear oscillator model. Namely,

$$m\ddot{x} + \gamma\dot{x} + \kappa x = H(t)F_{\perp} \tag{2.14}$$

where the dot refers to the time derivative, m is the mass of the sample, γ refers to losses, and κ refers to elastic restoring force. Also, H is the step function defined as $H(0 < t < t_{\text{off}}) = 1$ and $H(t > t_{\text{off}}) = 0$. The general solution of Eq.(2.14) expresses as

$$x_{\text{on}}\left(0 < t < t_{off}\right) = \frac{F_{\perp}}{\kappa}\left[1 + \frac{\beta_{-}e^{\beta_{+}t} - \beta_{+}e^{\beta_{-}t}}{\beta_{+} - \beta_{-}}\right], \tag{2.15}$$

and

$$x_{\text{off}}\left(t > t_{\text{off}}\right) = \frac{F_{\perp}}{\kappa}\frac{\beta_{-}e^{\beta_{+}(t-t_{\text{off}})} - \beta_{+}e^{\beta_{-}(t-t_{\text{off}})}}{\beta_{-} - \beta_{+}}, \tag{2.16}$$

where

$$\beta_{\pm} = \frac{-\gamma \pm \sqrt{\gamma^2 - 4m\kappa}}{2m}, \tag{2.17}$$

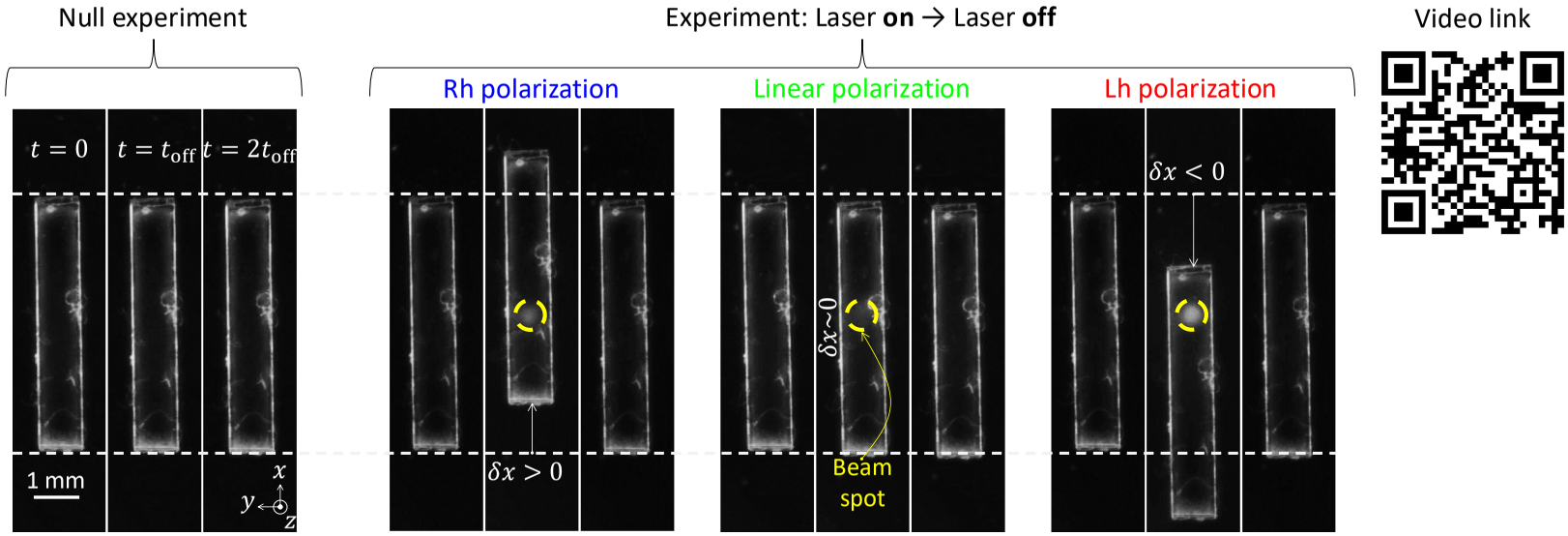

Figure 2.15: *A set of four experiments is shown as four groups of three images each, where a summary of video records can be seen by scanning the provided QR code. All groups start ($t = 0$) and end ($t = 2t_{off}$) at rest. Within the time interval $0 \leqslant t \leqslant t_{off}$ the sample is illuminated with a Gaussian beam of power $P \sim 1.4$ W, wavelength $\lambda = 1.4$ nm, and waist $w_0 = 0.45$ mm, until the laser is switched off at time $t_{off} = 3$ min, with the exception of the null experiment that remains without illumination all the time. The central image of each group corresponds to the time $t = t_{off}$. The null experiment allows testing of the stability of the system; experiments with circularly polarized light show that the spin of light directs the action of light on the object, $RH \rightarrow \delta x > 0$ and $LH \rightarrow \delta x < 0$; the experiment with linearly polarized light shows that the symmetrical action of the light cancels the previous effect.*

with $\{\gamma, \kappa\}$ being two adjustable parameters related with the viscous drag and an effective spring constant, respectively.

2.4.3 Quantitative analysis

A systematic study of the displacement of an object of mass m = 1.6 mg and dimensions 6 mm × 1 mm is made as a function of the incident optical power from 0.14 W to 1.4 W by 0.14 W steps, for both RH and LH incident circular polarization states. A complete cycle is considered as a period of excitation of three minutes followed by a period of relaxation of the same duration. The collected set of dynamics is displayed in Fig.2.16(a). In this figure, each curve is the average of three cycles; this provides a robust data set. The adjustment of the dynamical behavior using Eqs.(2.15), (2.16) and (2.17) yields constants of $\gamma \simeq 40$ mgs^{-1} and $\kappa \simeq 2$ mgs^{-2}, see Fig.2.16(b) for visualization of a given fit and Fig.2.17 for a summary of all the fitting procedures.

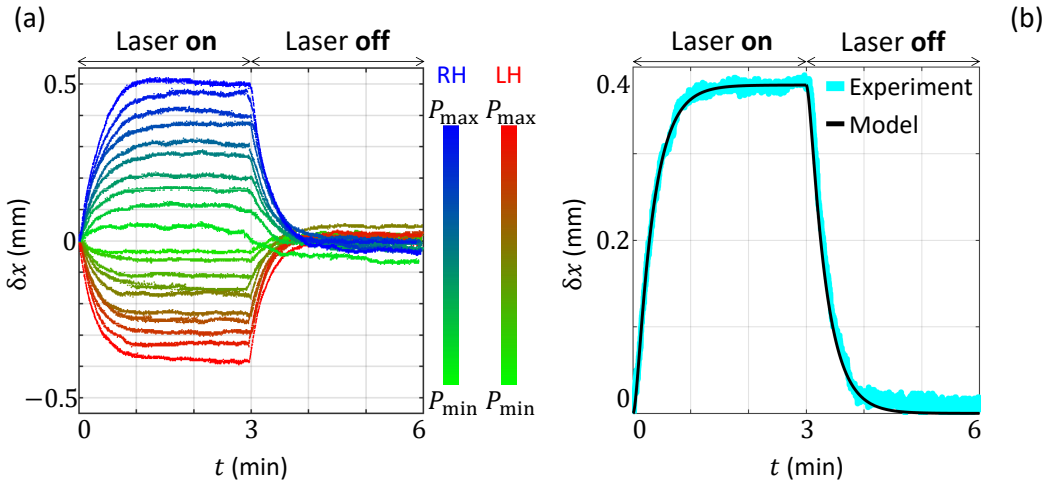

Figure 2.16: *Lateral force full set of experimental results obtained by laser illumination of* λ = 532 nm *circularly polarized, for ten evenly spaced power values from* 0.14 W *to* 1.4 W. *(a) Displacement* δx *as a function of time* t *and power* P. *(b) Typical excitation-relaxation dynamics and its adjustment at a given power and polarization handedness using* γ *and* κ *as the adjustable parameters.*

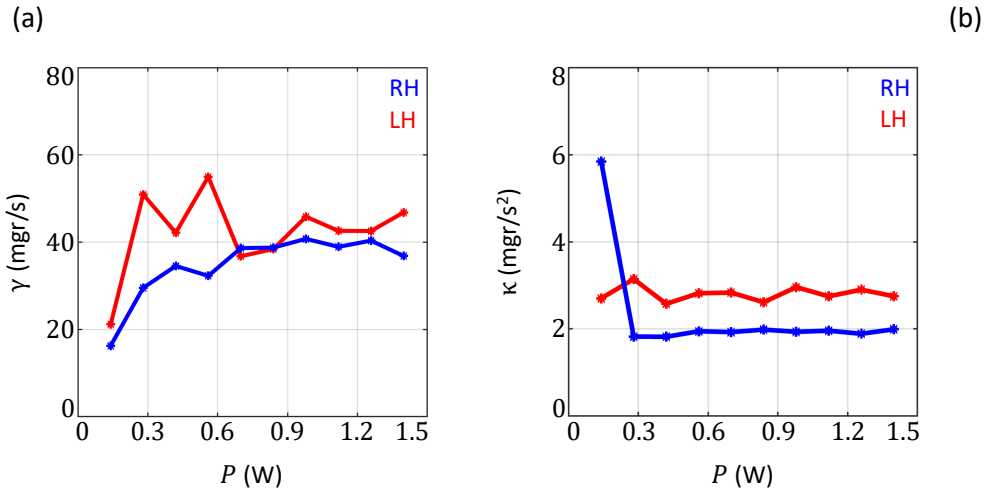

Figure 2.17: *Values of the adjustable parameters γ and κ enabling the qualitative description of excitation-relaxation dynamics as a function of power and polarization: (a) is constant associated to the viscous force γ, and (b) is the constant associated to the restoring force κ.*

2.5 Left-handed torques demonstration

2.5.1 Qualitative observations

Firstly, we note that, in contrast to an ideal q-plate design, our discrete version implies that the torque exerted by an incident beam depends on its intensity distribution. Indeed, increasing the 'optical lever arm' will increase the torque. This is quantitatively addressed by recalling that

$$\boldsymbol{\Gamma} = \iint \boldsymbol{r} \times \boldsymbol{f}_{\perp} dxdy, \tag{2.18}$$

where $\boldsymbol{f}_{\perp}$ is the force which lies on the surface and is perpendicular to a laser beam impinging at normal incidence onto the sample. Therefore, $|\boldsymbol{f}_{\perp}| \propto I$. Then, we can take advantage of the torque radial dependence by using an annular intensity distribution, which can be generated from a Gaussian beam by using a spherical lens and an axicon, see Fig.2.18.

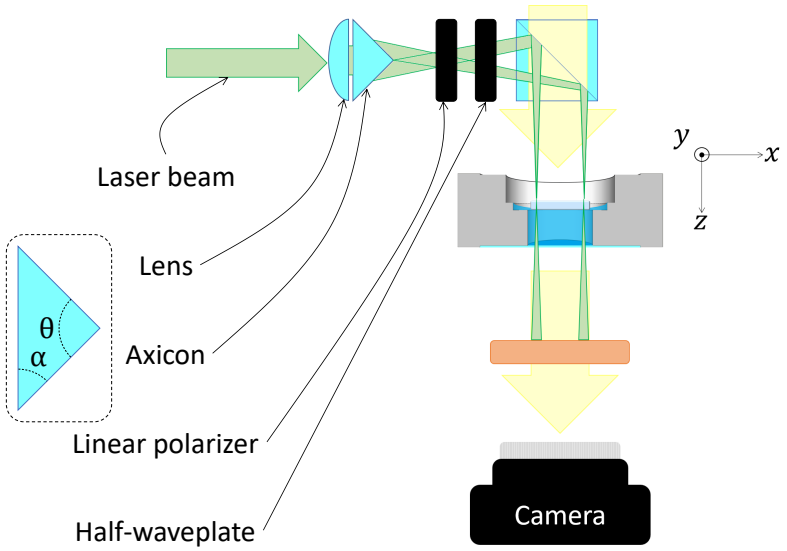

Figure 2.18: *A secondary line is added to the arrangement depicted in Fig.2.5(c). The use of a lens followed by an axicon, combined with the use of a linear polarizer and a half-waveplate, allow generating a circular polarized ring-shaped illumination.*

According to [70], the ring is characterized by a radius

$$r_0 = (n-1)\alpha f, \tag{2.19}$$

and a Gaussian width

$$w_0 = 1.05\lambda\frac{f}{w}, \tag{2.20}$$

where r_0, n, f, λ, w, and w_0 stands for the ring radius, the axicon refractive index, the lens focal length, the input beam waist, and the ring width at the focal plane, respectively, while $\alpha = (\pi - \theta)/2$ being θ the axicon apex angle. We tested a set of three UV fused silica ($n = 1.4607$ at $\lambda = 532$ nm) ultra-flat axicons of $\theta = \{179°30', 179°48', 179°57'\}$, from which we eventually used the first one in combination with a plano-convex lens of $f = 150$ cm to generate the intensity pattern at the focal plane shown in Fig.2.19(a).

We thus consider a ring-shaped intensity distribution $I(r)$ described by three parameters η_0, r_0, and w_0 shown in Figs.2.19(b,c) expressed as

$$\frac{I(r)}{I_{\max}} = \eta_0 + (1-\eta_0)e^{-2\left(\frac{r-r_0}{w_0}\right)^2} dxdy, \quad \text{for} \quad r < r_0, \tag{2.21}$$

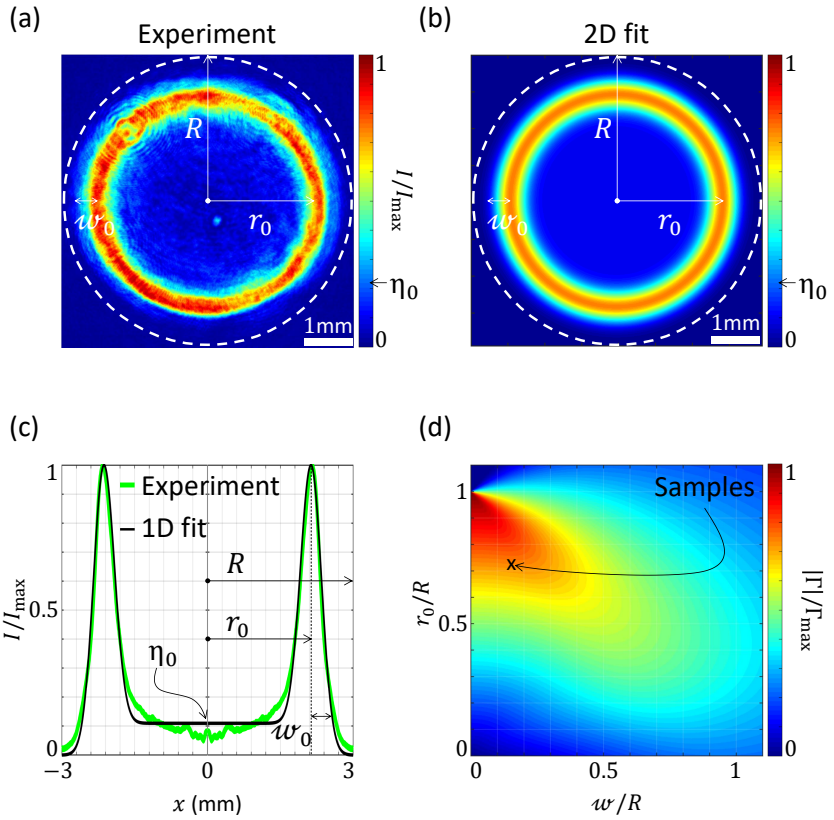

Figure 2.19: *Modeling the illumination and estimating the applied torque on the sample. (a) Experimental image of the controlled polarization lighting ring, generated with an axicon. (b) 2D fit of the experimental image and (c) 1D fit of the azimuthal average of the illumination intensity profile, and mirrored by the vertical axis in the sake of visualization and comparison, that corresponds to that used in our experiment. The elements of the initial observation are characterized by* $\eta_0 = 0.12$, $r_0 = 0.73R$, *and* $w_0 = 0.15R$. *(d) Estimation of the torque as a function of the parameters of the ring illumination: spinner radius* R, *ring radius* r_0, *and Gaussian waist radius* w_0.

and

$$\frac{I(r)}{I_{\max}} = e^{-2\left(\frac{r-r_0}{w_0}\right)^2} dxdy, \quad \text{for} \quad r > r_0, \tag{2.22}$$

This model allows us to evaluate that our experimental conditions correspond to a torque of magnitude

$$|\mathbf{\Gamma}| = \frac{4\sin\alpha}{c} \int_0^R I(r) r^2 dr \tag{2.23}$$

that is approximately 75% of the ideal value expected, see Fig.2.19(d).

Two kinds of rotors of four sectors each, are prepared according to Fig.2.13(c,d), and a pair of them are shown in Fig.2.20. Using the system depicted in Fig.2.5, the rotors are placed on the tailored axisymmetric capillary trap of our air/liquid interface. Then, the rotors are illuminated with the circularly polarized beam having ring-shaped intensity profile shown in Fig.2.19(a) with $P \sim 3$ W incident power for 2.5 min and observed for an additional 2.5 min without illumination.

The qualitative observations are shown in Fig.2.21. Both right-handed and left-handed torques are observed with an angular deviation of several degrees in a steady state. Note that the objects were not spinning as one could have expected. We attribute this to the fact that the contour of the rotors is irregular due to the hand-cut manufacturing process. Irregularities at the rotors' edge are 'imprinted' on the contact line which leads to wrinkled air/liquid interface. Ensuing broken axisymmetry prevents a rotational motion to takes place easily.

2.5.2 Modeling the rotational dynamics

The results are shown in Fig.2.22 for the two kinds of fabricated rotors shown in Fig.2.20. As we have seen, the rotational dynamics shows similar behavior as we observed in the lateral force experiments. Using the analogy between the

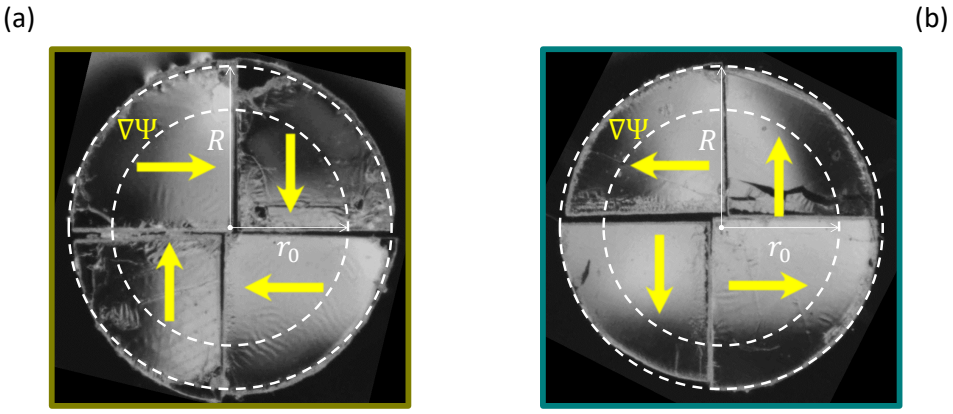

Figure 2.20: *Two samples with opposite spatial distribution of the orientational gradients* $\nabla\psi$*, and radius* $R = 3$ mm *are prepared to ensure either (a) left-handed or (b) right-handed effects.*

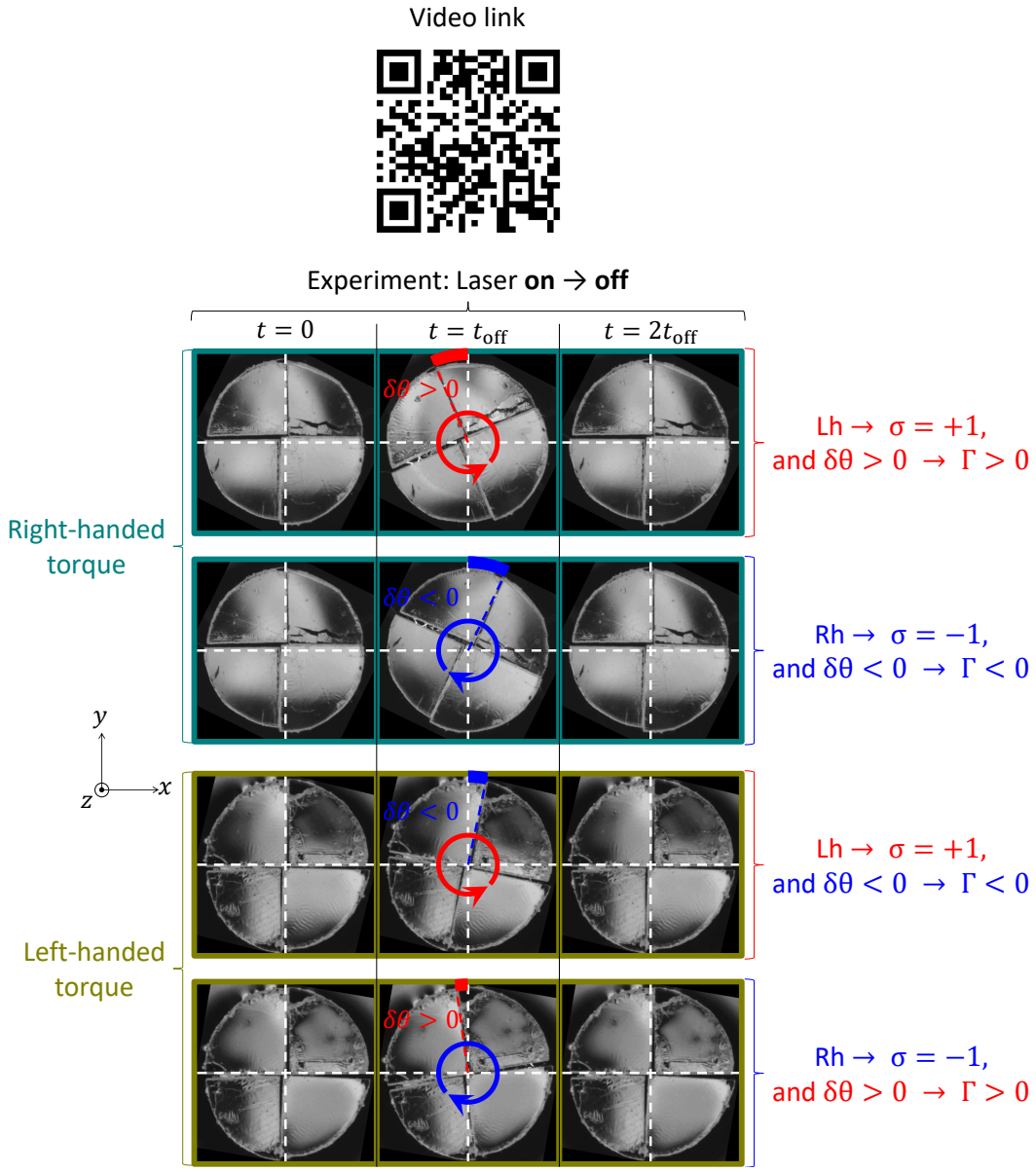

Figure 2.21: *A set of four experiments is shown as four groups of three images each, where a summary of video records can be seen by scanning the provided QR code. All groups start ($t = 0$) and end ($t = 2t_{\text{off}}$) at rest. Within the time interval $0 \leqslant t \leqslant t_{\text{off}}$ the sample is illuminated with the ring-shaped beam described in Fig.2.19(a), and a power $P \sim 3$ W, until the laser is switched off at time $t_{\text{off}} = 2.5$ min. The central image of each group corresponds to the time $t = t_{\text{off}}$. Typical steady-state angular deviation $\delta\theta$ (of the sample in the (x, y) plane) associated with right-handed ($\sigma\Gamma > 0$) and left-handed ($\sigma\Gamma < 0$) optical torque experiments.*

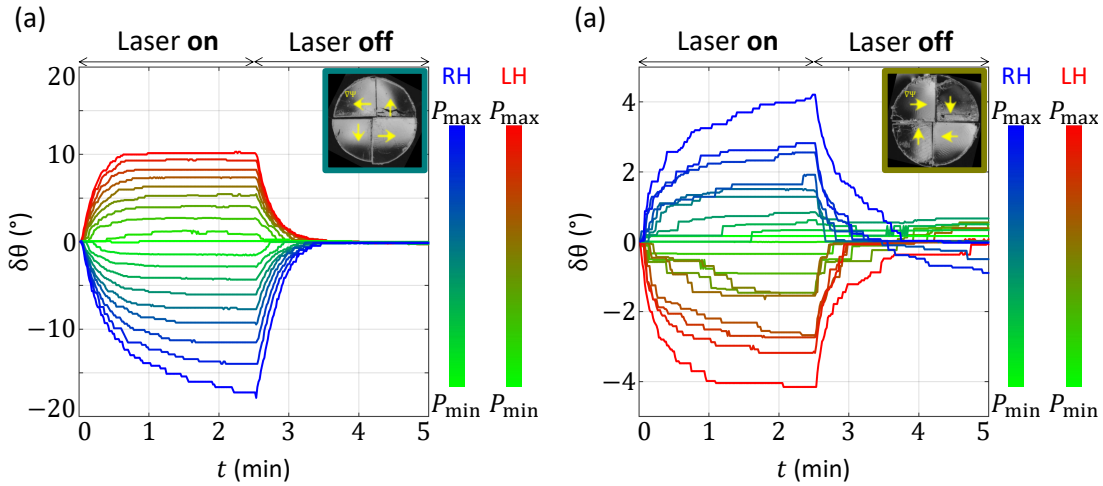

Figure 2.22: *Collected data of the optical torques experiment. Plot of angular displacement as a function of time and spin-power for the case of the (a) right-handed rotor and the (b) left-handed rotor; each curve is the average of three cycles of excitation/relaxation at fixed spin-power.*

position and the angle spatial variables, i.e., $x \to \theta$ and $m \to I = \frac{1}{2}mR^2$, we obtain the following model:

$$I\ddot{\theta} + \gamma\dot{\theta} + \kappa\theta = H(t)\Gamma_{\text{opt}}. \tag{2.24}$$

Its general solution is

$$\theta_{\text{on}}\left(0 < t < t_{off}\right) = \frac{\Gamma_{\text{opt}}}{\kappa}\left[1 + \frac{\beta_- e^{\beta_+ t} - \beta_+ e^{\beta_- t}}{\beta_+ - \beta_-}\right], \tag{2.25}$$

and

$$\theta_{\text{off}}\left(t > t_{\text{off}}\right) = \frac{\Gamma_{\text{opt}}}{\kappa}\frac{\beta_- e^{\beta_+(t-t_{\text{off}})} - \beta_+ e^{\beta_-(t-t_{\text{off}})}}{\beta_- - \beta_+}, \tag{2.26}$$

where

$$\beta_\pm = \frac{-\gamma \pm \sqrt{\gamma^2 - 4I\kappa}}{2I}, \tag{2.27}$$

with $\{\gamma, \kappa\}$ being two adjustable parameters related with the viscous drag and an effective spring constant, respectively.

2.5.3 Quantitative analysis

Typical excitation/relaxation rotational dynamics are presented in Fig.2.23(a), which shows the average of three independent events. As for the lateral displacement experiments, the dynamics are quantitatively described by Eq.2.24. The losses still arising (mainly from the viscosity of water) are taken into account by coefficient γ, while κ relates to a torsional spring probably arising from elasticity associated with the wrinkled air/liquid interface commented above.

The power dependence of the effect is shown in Fig.2.23(b), where the right- and left-handed nature of the driving optical torque is inferred by looking at the sign of the product $\sigma\theta_\infty$, where θ_∞ is the steady angular deviation under constant irradiation power. Indeed, $\sigma\Gamma$ and $\sigma\theta_\infty$ have the same sign. In addition, we emphasize the large value of the optical torque per unit power, which is estimated by dividing Eq.2.23 by the total beam power, namely

$$\frac{|\Gamma|}{P} = \frac{2\sin\alpha}{\pi c}\frac{\int_0^R I(r)r^2dr}{\int_0^\infty I(r)dr}, \tag{2.28}$$

which is of the order of 1 $\mathrm{pNmW^{-1}}$ for our samples, see Fig.2.23(c).

It is instructive to mention that the present macroscopic samples behave as effective q-plates, introduced in Sec.1.4.3 and Fig.2.8, with structural topological charges $|q_{\text{ eff}}| \sim 1700$, see Fig.2.23(d). This is deduced by balancing the Eq.2.23 with Eq.2.8, which gives

$$q_{\text{eff}} = 1 \mp \frac{|\mathbf{\Gamma}|\omega}{2P} \tag{2.29}$$

for the right- and left-handed cases, respectively.

2.6 Summary and prospective study

The main results of this chapter have been published in 2018 in Nature Photonics [71]. We showed that the direct experimental observations of unusual optomechanical manifestations are restricted neither to complicated instrumental approaches nor to weak transverse effects that vanish in the limit of the single dipole. This points out that structured anisotropic matter is a versatile optics to

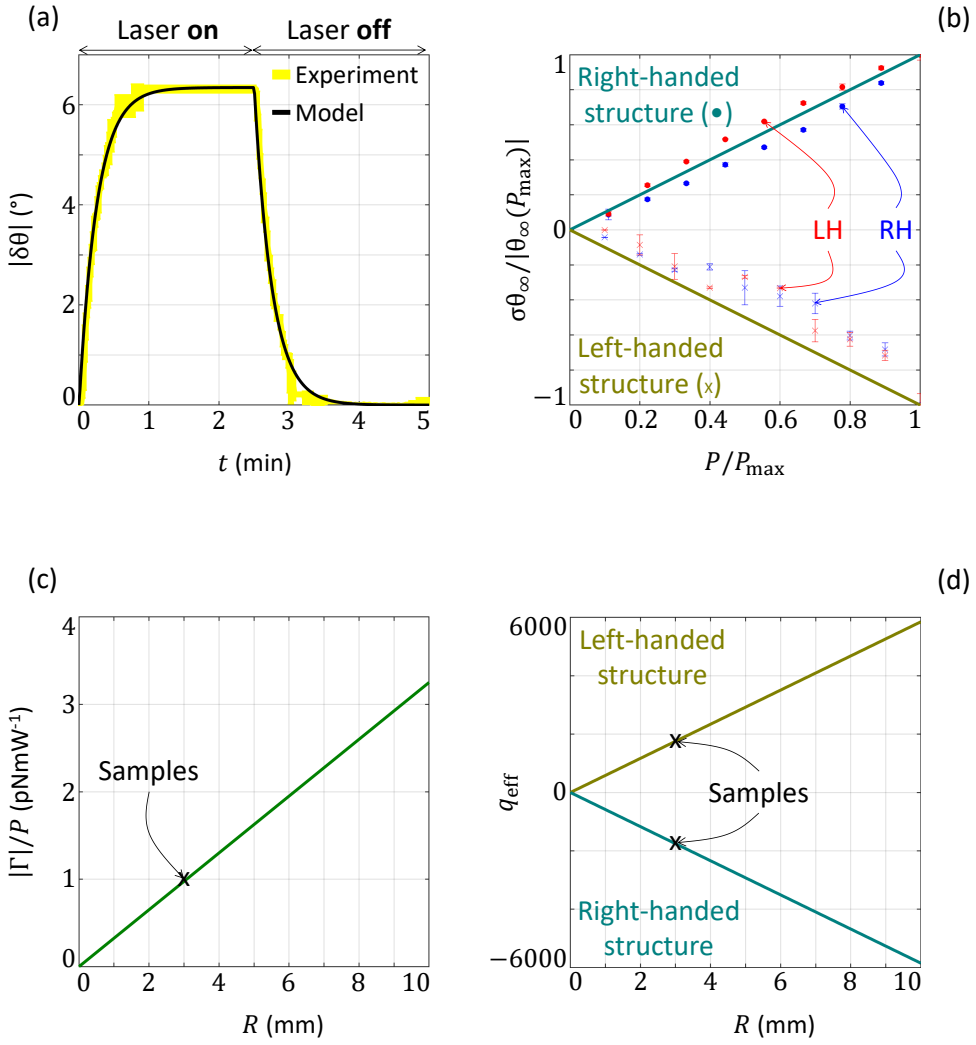

Figure 2.23: *Results and analysis of the torque experiment. (a) Typical curve and fit of the experiment that gives* $\gamma \sim 60$ mgmm^{2}s^{-1} *and* $\kappa \sim 10$ mgmm^{2}s^{-2}. *(b) Power dependence of* $\sigma|\theta_\infty|/\theta_\infty(P_{\max})$, *with* $P_{\max} \sim 3$ W, *the sign of which allows straightforward identification of the right-handed and left-handed nature of the applied optical torque. (c) Calculated torque per unit power as a function of radius of an ideal four-quadrant disk irradiated by a circularly polarized incident ring-shaped beam in the sample plane, using the actual beam parameters. (d) Estimated structural topological charge* q_{eff} *with radius* R.

explore new facets of light-matter interactions, which do not necessarily require the use of coherent light sources. Interestingly we recall that, until now, geometric phases and spin-orbit interactions have been able to displace light beams [72], but now it has been shown that they can displace matter along independent degrees of freedom of translation and rotation.

Achieved naked-eye observations using macroscopic objects with nominal optical force of the order of 1 nN implies dealing with mechanical effects that do not suit practical applications at the macroscale. Instead, nN-level forces are well-adapted for optical manipulation at the microscopic scale, as testified by the development of micromanipulation technologies fueled by light, such as optical tweezers. This motivated us to explore the possible implementation of based on the spin-orbit interaction of light. The associated challenge is to define, design, fabricate, and manipulate such micro-optical elements, which is the matter of the next chapter.

CHAPTER 3

Towards spin-orbit optomechanics at the microscale

In the preceding chapter, we reported on the direct experimental assessments of optical lateral forces and left-handed torques via their mechanical manifestation using millimeter-sized spin-orbit optical elements. In this chapter, we report chronologically on experimental attempts to observe the left-handed torque at the micrometer scale. In Sec.3.1, we introduce the material subwavelength design that we used in all our attempts, first realized using structured gold thin films. Such an option has rapidly been abandoned, and the three other options we explored are then discussed as independent sections. In Sec.3.2, we present our experimental attempts with silicon-nitride spinners, which correspond to miniaturized versions of previously used macroscopic samples. This option turned out to be unsuccessful, and we then moved to the use of diamond samples, which is presented in Sec.3.3. Still, without yet obtaining robust and satisfying light-induced rotational effects. The chapter is eventually ending with the Sec.3.4 where we present our most promising developments that are still in progress at the time of writing this manuscript.

3.1 First steps towards spin-orbit micro-optics

As we demonstrated in Chap.2, polymer liquid crystal materials are an appropriate material for manufacturing spin-orbit optical elements at the millimeter scale that allow implementing optical manipulation experiments. However, we recall these elements are made from structured 2 µm-thick films deposited on plastic disks of two inches diameter and 200 µm thickness, eventually cut by hand.

Therefore, we had to rule out such an approach from scratch due to obvious crippling issues when considering miniaturization.

The need for miniaturization led us to initiate the development of spin-orbit micro-optical elements that could eventually be used in optomechanical experiments. At first, the idea was merely to gain expertise in the fabrication and characterization of microscopic spin-orbit vortex generators based on azimuthally patterned artificially birefringent elements. This was done in collaboration with the Swinburne University of Technology, where the group of S. Juodkazis has a long-standing experience in material science and nanofabrication technology. I contributed to these efforts, at first by doing part of the structural and optical characterization of the fabricated samples. The latter are geometric phase metasurfaces with space-variant nanoslits milled through 300 nm-thick gold films. They operate as an azimuthally varying birefringent optical retarder enabling the generation of high-purity optical vortex beams with topological charges up to $|\ell| = 10$ in the visible range, which led to a paper I am coauthoring [73].

In practice, we choose a discrete design made of equal-angle sectors, each of them being associated with a uniform orientation of the subwavelength grating, see Fig.3.1(a-f). Design has been optimized to give birefringent phase retardation of almost π at 532 nm wavelength. Optical vortex generation capabilities are experimentally tested by irradiating the samples with circularly polarized Gaussian beam whose diameter fits into the structured area, which is a disk with diameter 100 µm. The typical intensity profile of the generated optical vortex beams and their spiral interference patterns for different circularly polarized incident Gaussian beams are shown in Fig.3.1(g-l). Once the sector-design has been validated, we had to address the challenge of obtaining freely-moving microscopic vortex generators.

However, in the previous example, the gold layer lies on a 500 µm-thick glass substrate. This implies that the 'structure + substrate' must be, (i) cut and released, (ii) capture and transport into an experimental chamber before any optomechanical attempt can be initiated. Also, recalling that the diameter of the structure is 100 nm, a successful cut-and-release process will provide with a tall cylinder aspect ratio will make it rather difficult to handle for optical mani-

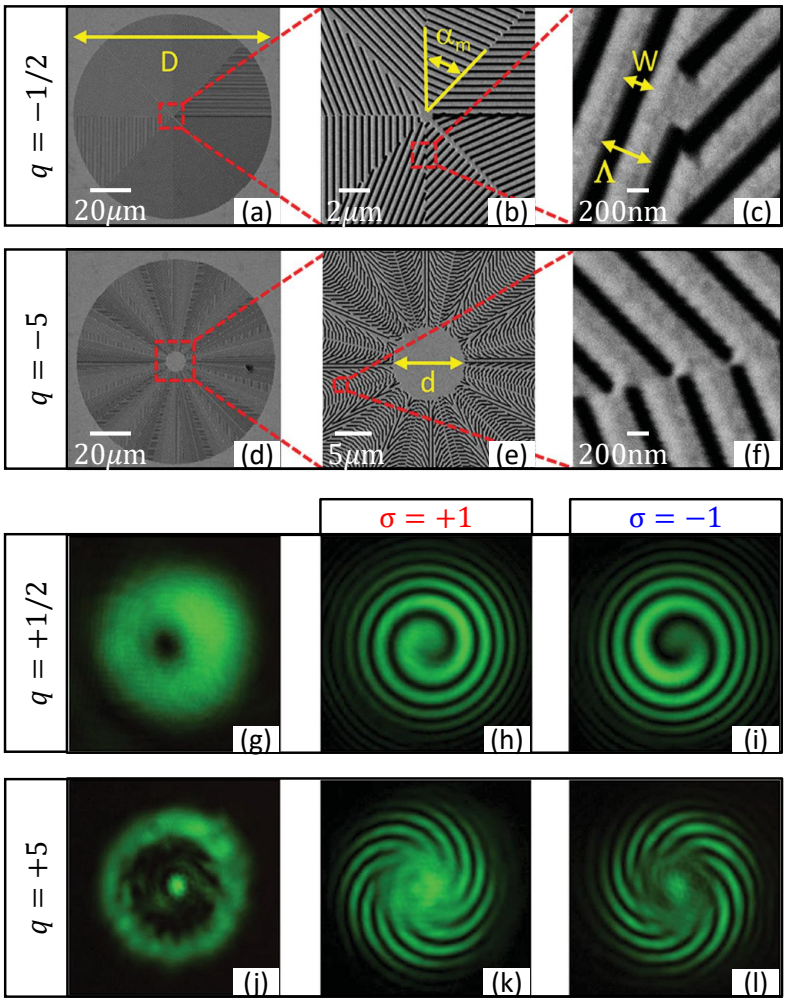

Figure 3.1: *SEM images (a–c) of fundamental* $q = -1/2$ *and (d–f) high-order* $q = -5$ *metasurfaces with thickness* $h = 300$ µm, *diameter* $D = 100$ µm, *grating period* $\Lambda = 500$ nm, *and slit width* $W = 160$ nm. *Each device is made of* $16|m|$ *sectors of angular width* $\alpha_m = \pi/(8|m|)$ *with* $\pi/8$ *steps for the grating orientation between adjacent sectors; see panels (b) and (e). The central part of high-order metasurfaces is purposely left unstructured over a disk of diameter* $d = 10$ µm *to preserve a proper resolution of the azimuthal pattern; see panels (e) and (f). Experimental intensity pattern of the circularly polarized component of the output vortex field whose polarization state is orthogonal to the incident circularly polarized Gaussian beam in the case of (g)* $q = 1/2$ *and (j)* $q = 5$. *Interference pattern of the generated optical vortex beam of charge* $\ell = 2\sigma q$ *with a coaxial Gaussian beam for two different incident helicities* $\sigma = \pm 1$; *see panels (h) and (i) for* $q = 1/2$ *and panels (k) and (l) for* $q = 5$.

pulation experiments, especially if considering to place the element at air/water interface for instance.

One approach to deal with such technical difficulties could be to consider thinner substrates, such as commercially available glass films with thickness ranging from 1 µm to 10 µm. By doing so, we would obtain flat disk-shaped samples, which could be cut using femtosecond laser milling. However, we anticipated thermal issues associated with the use of metal nanofilms, and we decided to move to a full dielectric option that allows more accessible manufacturing and handling of nanostructured micro-optical elements. This is discussed in the next sections.

3.2 Nanostructured silicon nitride option

Dielectric samples can be manufactured using commercial substrates in the typical thickness range of 100 nm – 1000 nm. This allows designing elements with typical lateral size of 10 µm – 100 µm, hence giving 'flat' disk-shaped optical components. Also, unlike metallic option, higher transmittance can be achieved when using the transparency window of the selected dielectric material. After evaluating the accessible materials and the technology with which we could work, we first decided to use silicon nitride membranes.

The design of the spin-orbit dielectric structures follows the same approach as for metal structures. Namely, it involves the structuring of the space-variant optical axis from subwavelength gratings using a discrete piecewise design for the azimuthal orientation of the optical axis. Specifically, we opted for 500 nm-thick membranes, which results from balancing the manufacturing time and the purity of the vortex generation based on the available thicknesses and nanofabrication tools. Indeed, on the one hand, thicker structures are preferable to achieve the optimal half-wave plate condition, however leading to a substantial increase in the manufacturing time. On the other hand, the mechanical integrity of the structures is found to be compromised for the slit depth larger than 350 nm. Eventually, the grating period is set to Λ = 500 nm, and the width of the slit is W = 250 nm. Scanning electron microscopy images are shown in Fig.3.2. Of

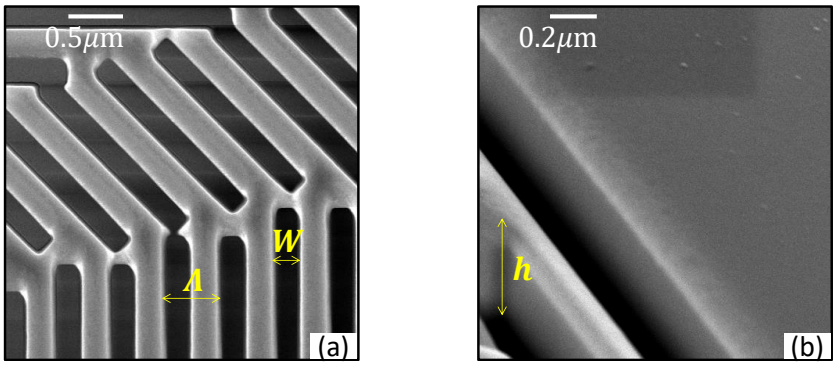

Figure 3.2: *Scanning electron microscopy images illustrating the fabricated dielectric space-variant birefringent pattern on a silicon-nitride membrane. (a)* Λ *and* W *correspond to the grating period and the slit width, respectively. (b)* h *corresponds to the membrane thickness.*

course, we are aware that the chosen period prevents claiming a truly subwavelength design keeping in mind that our operating wavelength for optical manipulation experiments is λ = 532 nm. Nevertheless, this choice comes from a trade-off between several practical constraints, which does not prevent for attempting to report on the sought-after effects.

3.2.1 Release and collection protocols

3.2.1.1 Mechanical release

Once the samples are fabricated, the challenge is to release the disk-shaped structured area. Our first approach consists to mill a circle around the structured area below which the coverslip has been previously covered by a polyvinyl alcohol (PVA, which is our water soluble glue) layer enabling to 'capture' the released object by sticking once it falls after the cut, see Fig.3.3(a,c-e). However, some cut micro-disks jumped in such a way that they got stuck on the black (non-transparent) membrane frame; we suspect that is a result of residual electrical charges from ion milling, see Fig.3.3(b) that illustrates what we call a 'bad' or 'good' release event.

In order to recover the precious samples, we figured out a mechanical recovery

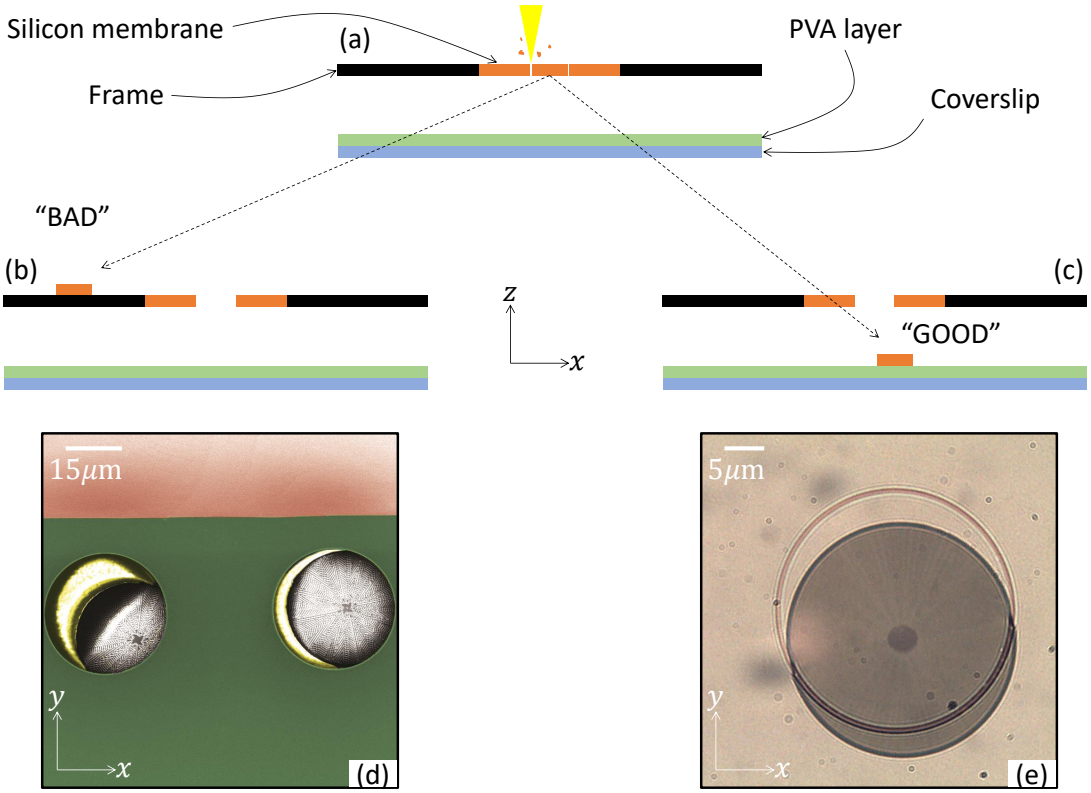

Figure 3.3: *Release of nanostructured micro-optical elements. (a) With the milling ion-beam, the structure is circled, while a coverslip has been previously coated with a PVA layer enabling to 'capture' the released object by sticking once it falls after the cut. Unsuccessful release event may happen, see (b), while the happy ending case is illustrated in (c). (d) Pair of spinners after milling, leaving the surrounding unstructured membrane (here artificially colored in green) and further caught by a polyvinyl-alcohol layer deposited on a glass substrate. (e) Bright field optical image of a spinner on a glass substrate after its release from the membrane. The circular footprint of the milling process can be seen.*

plan. We begin with the assembly of a microscope in reflection configuration to which we adapt a needle, both on independent translation stages for greater versatility. The black frame with the spinners to recover is deposited on a coverslip at the bottom of a glass vessel filled with water, hoping that when pushing the spinner with the needle tip, it would fall on the coverslip: the experimental arrangement is shown in Fig.3.4(a). According to the sequence of images from a

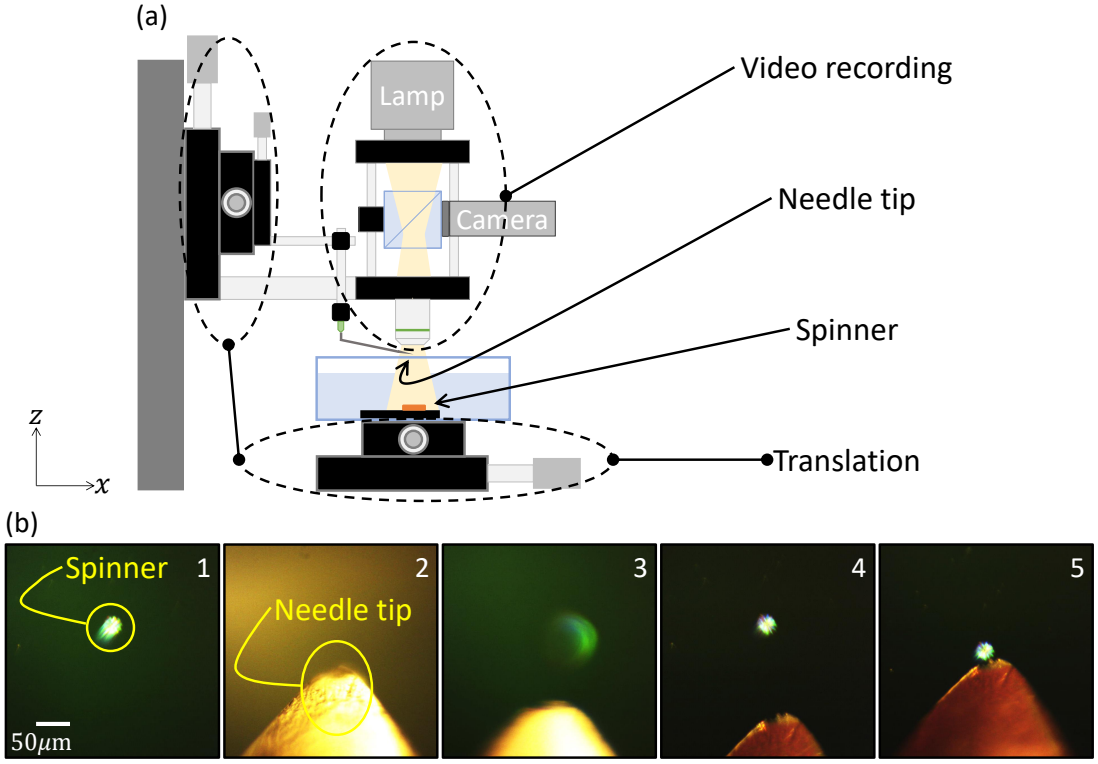

Figure 3.4: *Mechanical collection strategy. (a) System to recover samples consisting of a reflected light microscope configuration with an adapted free-to-move needle. The black frame with spinners is placed on the bottom of a glass vessel filled with water, in which the sample is expected to be collected. (b) Sequence of frames extracted from video recording of the mechanical recovery process: (1) The sample is located and centered (2) then the microscope is moved up to put in position the needle tip. (3-5) The needle tip is approached to the frame nearby the micro-structure in order to try to push it until it hopefully falls from the frame.*

release attempt video record shown in Fig.3.4(b), first, we locate the spinner without the needle on the screen. Then, playing with the image focus position, we align the needle tip almost at the location of the spinner in the (x, y) plane. Finally, we approach the needle close to the sample and gently push it until it falls out of the frame. This protocol should be made with great care, we recall here that all micro-manipulation steps are made by hand using micrometric translation stages.

We applied this procedure for two spinners that were in this situation. However, the approach failed. Indeed, the first one jumped out violently and we were not able to find it later, and the second one broke during the manipulation. Later on, we only focus on the spinners that remain on the membrane or those caught on a transparent substrate, which is what we describe next.

3.2.1.2 Release assisted by light

In order to avoid loosing spinners do to uncontrolled jumps at the end of the milling process, we decided to cover one of the two the faces of the membrane that will not be structured with a layer of PVA. Then, we structure the opposite face and finish with the ion-beam cutting of the spinner. Since PVA is a water-soluble synthetic polymer, we initially expected entire dissolution at contact with water. Unfortunately, water dissolution alone was not enough to make the spinners free. This led us to propose using a laser beam to assist the release for which we conceived the strategy illustrated in Fig.3.5. The strategy consists to create a closed and controlled volume environment where the object is confined, for which water is the natural candidate because it is a solvent for PVA.

First, using a bit of epoxy glue, the membrane frame is glued to the coverslip with the spinners and the PVA layer oriented in the opposite direction to the coverslip. Second, ~ 0.25 ml of water is deposited on the membrane and turned down and carefully placed on spacers that regulate the height h of the cell but allowing the drop to make contact with the lower coverslip. We choose a height $h > 100$ µm, which is typically three times larger than the spinner diameter ($2R$ = 30 µm). Finally, the system is ready to be irradiated with a laser beam making the light interaction and gravity release the spinner. As illustrated by step 3 in Fig.3.5, we start pumping with a laser beam of wavelength λ = 532 nm. Initially, we set the beam waist w_0 to match the spinner radius R and the power P is varied in the typical range 1 mW - 1 W.

In practice, once we get to the third step described above, which corresponds to what is shown in Fig.3.6(a), the release attempt is performed with a linearly polarized beam having a diameter equal to that of the spinner and initial power of 10 mW. The process begins with the continuous irradiation of the spinner at

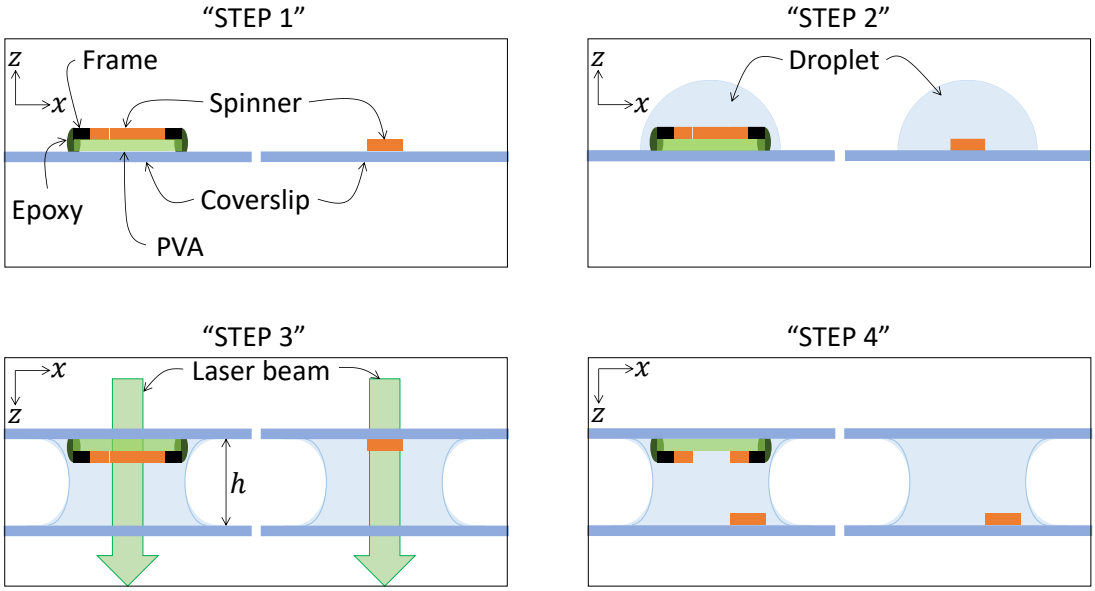

Figure 3.5: *Strategy to release the spinners depicted in four steps, either from their polymer-coated membrane or from a coverslip. The objective is to store every spinner on individual coverslip with the ability to release them on-demand at a later stage of the experiments. (1) Samples on a coverslip showing two situations: the spinner is either on the polymer-coated membrane or already sitting on the glass coverslip. (2) We place a droplet that covers the sample and then turn it upside, facing down a second coverslip, as shown in (3). A laser beam is used to release the sample from the upper substrate at a distance h from the bottom substrate, controlled by spacers, and let it freely falling onto the lower substrate (4).*

the lowest power level, followed by power increase with 5 mW step every 30 s, until a bubble is formed nearby the spinner. This happens at ~ 80 mW and when this occurs it is hard to visually monitor the events and the light-induced bubbles typically disappear after ~ 10 min. Several attempts for many spinners were carried out according to this protocol. Eventually we decided to quit such an approach since a burnt area was obtained at the end of the process.

Then, we decided to change strategy: instead of using a gradual increase of the beam power under continuous irradiation, we irradiate the sample only for a few seconds at a given power. Starting from low power value, we repeat cycles

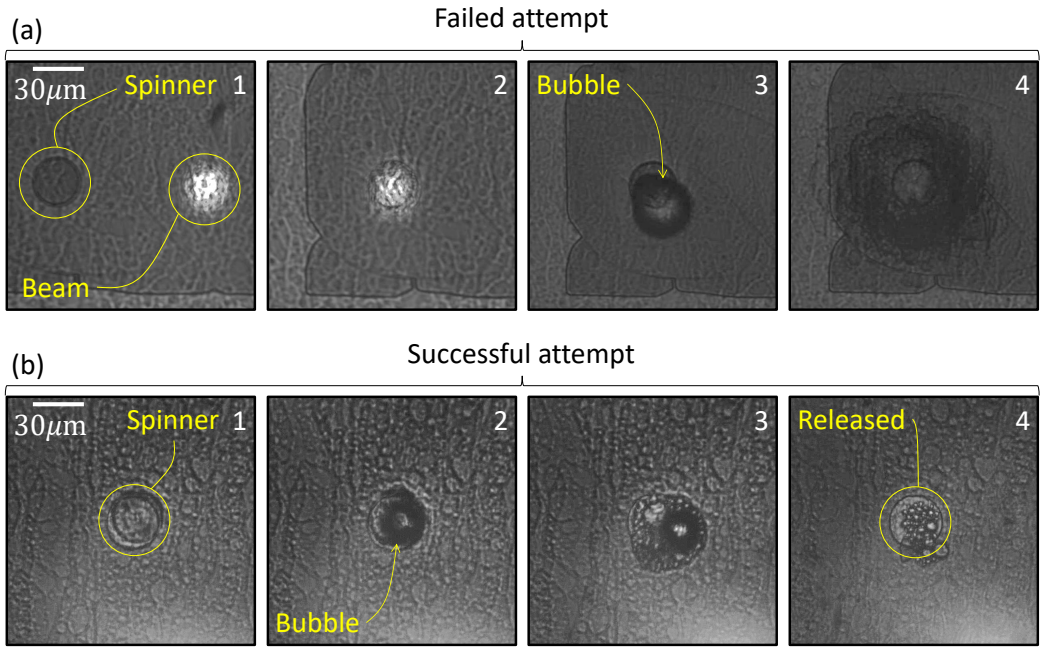

Figure 3.6: *Sequences of images that summarize the pathway followed to release the first spinner from the polymer. (a) Attempt to release a sample via progressive increase of the incident optical power and continuous illumination. (1) The target to be released and the spot of the laser beam on the polymer-coated sample. (2-3) Effect of laser irradiation that leads to the formation of a bubble. (4) Repeating the process does not help and eventually leads to a burnt area, evidenced by the appearance of a dark region. (b) Attempt to release a sample via an abrupt increase of the incident optical power, with transient irradiation exposure. (1) Target to be release. (2-4) Bubbles are generated as in the continuous case shown in (a), after several cycles of on/off exposure with ever-increasing power level, the spinner is eventually detached from the substrate.*

of short exposure followed by the relaxation time of the order of 30 s. Up to roughly 100 mW power bubbles are observed but without noticeable effects on the spinner until it suddenly detaches, see Fig.3.6(b). This protocol is found to be robust and reproducible, and the spinners have been released in such a manner. We eventually released three out of six initially fabricated spinners. Additional batches of silicon nitride samples led to the fabrication of a total of 24 spinners, the recovering rate is slightly below 50%.

3.2.1.3 Release-collection-storage protocol

Having the released spinners on the same coverslip together with impurities (that come mainly from the membrane) is a drawback, keeping in mind that further manipulation is our plan. Then, we applied the previous procedure again, starting at 200 mW, but it turned out badly for the spinner, which was broken, as shown in Fig.3.7.

Optical manipulation of freshly detached spinners lying at the bottom of the release chamber was unsuccessful. Spinners behave as if they are attached to the coverslip on which they landed. As a matter of fact, we need to be able to release on-demand the spinners to implement optical manipulation experiments. To this aim, a transfer protocol from one coverslip to another is established. Spinners are irradiated with the beam of the same diameter as the spinners but starting at 10 mW for 30 s and gradually increasing the power in steps of 10 mW, as shown in Fig.3.8. Finally, we managed to transfer them without any damage, and systematically we observed that the detachment occurred at beam power ~ 80 mW, which coincides with the conditions for the generation of bubbles at the first release step when the spinners are on their native membrane. The spinners did not exhibit any visible mechanical damage nor reduced their optical performance during the transfer protocol between substrates, which is found to

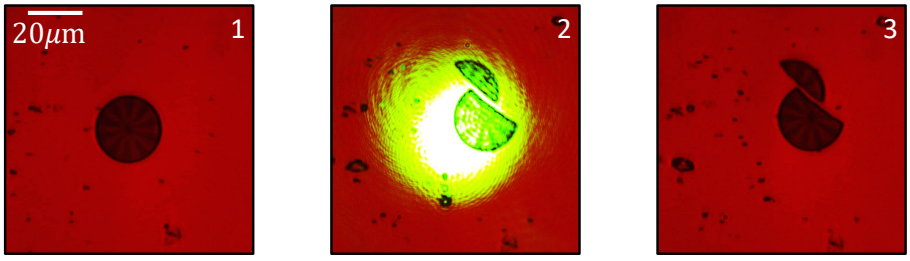

Figure 3.7: *Example of a failed attempt to transfer a spinner between substrates, where you wanted to focus on a new substrate after being released and collected from its original substrate, in the end, it breaks. After several tests with this spinner, it was determined that the safe beam power is* < 100 mW, *with a beam of diameter* ~ 30 µm.

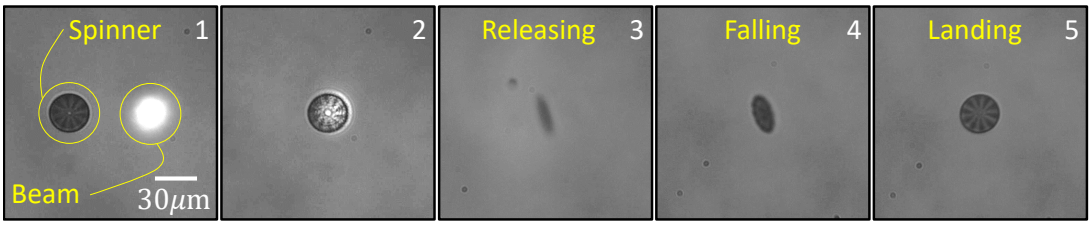

Figure 3.8: *Optical releasing protocol to transfer the sample from one substrate to another. (1) The spot of the laser beam that is of the same diameter as the sample is observed. (2) The sample is illuminated with a power of* ~ 80 mW. *If the sample is not released, the light power is increased by* 5 mW *along off/on/off irradiation cycles. (3-5) Series of images showing the fall of a spinner after its release until it lands on the lower substrate: here, we manually adjust the imaging focus condition to follow the spinner during its falling.*

be extremely robust. Indeed we repeated the process without fail several tens of times.

Summarizing, all the released spinners are transferred to an independent substrate, and sometimes we use this protocol a couple of times in a row to get rid of dust or other impurities that could lie nearby a collected spinner or simply to relocate the position of a spinner on the coverslip to ease further handling.

3.2.2 Single Gaussian pumping beam experiments

Firstly, we choose to manipulate optically the spinner at an air/liquid interface, for which we prepare the system by placing a water droplet on the substrate, in order to cover the spinner. Then we flip the substrate upside down so that the droplet gets suspended from the substrate. Subsequently, we place the substrate on the container designed to isolate the droplet from air flow as shown in Fig.2.10(a), and we release the spinner in a similar way to the previously described transfer protocol. After release, the spinner is self-centered at the bottom part of the droplet and is ready to be manipulated, see Fig.3.9(a).

The first attempts consisted of pumping the spinner from 1 mW incident power with a circularly polarized Gaussian beam, having a diameter of the order of the spinner diameter and the power is progressively increased by 1 mW

steps until light-induced motion is detected. However, the spinner escapes the illumination area above 7 mW power, so we had to operate below that power, see Fig.3.9(b).

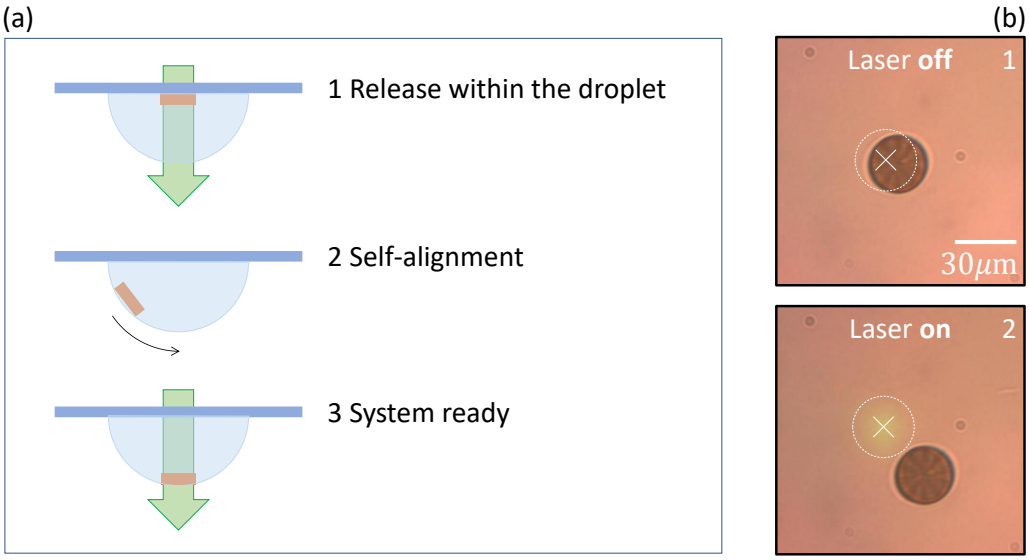

Figure 3.9: *Attempt to spin the sample by illuminating it with a Gaussian laser beam of the same diameter as the sample, with an initial power of* 1 mW *and increments of* 1 mW *every* 5 min. *(a) Sketch of the system depicted in three steps, similar to the system depicted in Fig.2.10(a). (b) Spinner in steady-state as in step 3 is eventually displaced by the laser beam at* 7 mW*, and no rotation is observed.*

Unfortunately, we do not observe stable rotational motion during several minutes of exposure although angular displacements can be observed. Also, during the experiment, we had to refocus the image of the object which indicates a change in the height of the pending droplet certainly due to evaporation. Observed erratic displacements are uncontrolled and we were not able to cope with this issue. Consequently, we developed strategy to mitigate such unwanted lateral displacements.

3.2.3 Optical confinement strategy

The idea is to confine the spinner at the place where the pump beam is and since the object escapes from the area of high intensity, the use of an optical beam having a donut-like intensity profile could help at first sight. For instance this could be made by using incident vortex beams. However, in order to prevent orbital contribution to the sought-after mechanical effects we use a radially polarized beam. Such a beam corresponds to the coherent superposition of two contracircularly polarized vortex beams having opposite topological unit charges. We obtain it by using a commercial component from Altechna, which is basically an azimuthally-varying half-waveplate having an orientation angle ψ of its optical axis given by $\psi = \phi/2$.

Then, we add the optical pumping field obtained from an independent laser source, namely, which is the circularly polarized Gaussian beam, see Fig.3.10. Although the pumping beam tends to expel the spinner, the idea is to use a trapping vortex field with high-enough power (up to 1.5 W in practice).

In practice, even though the doughnut trap strategy works, it is not stable enough because it induces a slight wobbling of the object that is out of control. Still we continued with this strategy by improving the intensity profile of the trapping optical field for our needs. This is done by using a ring-shaped intensity type profile, obtained using an axicon instead of a vortex plate. The setup is shown in Fig.3.11.

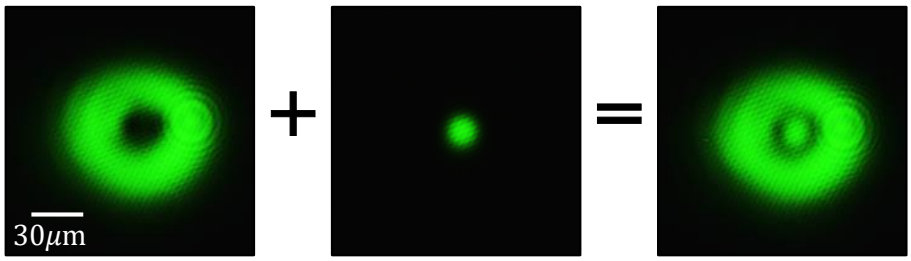

Figure 3.10: *Superposition of two incoherent beams: a doughnut one (radially polarized) and Gaussian one (circularly polarized). Two independent lasers at* 532 nm *wavelength are used, preventing from interference between the trapping and the manipulating fields*

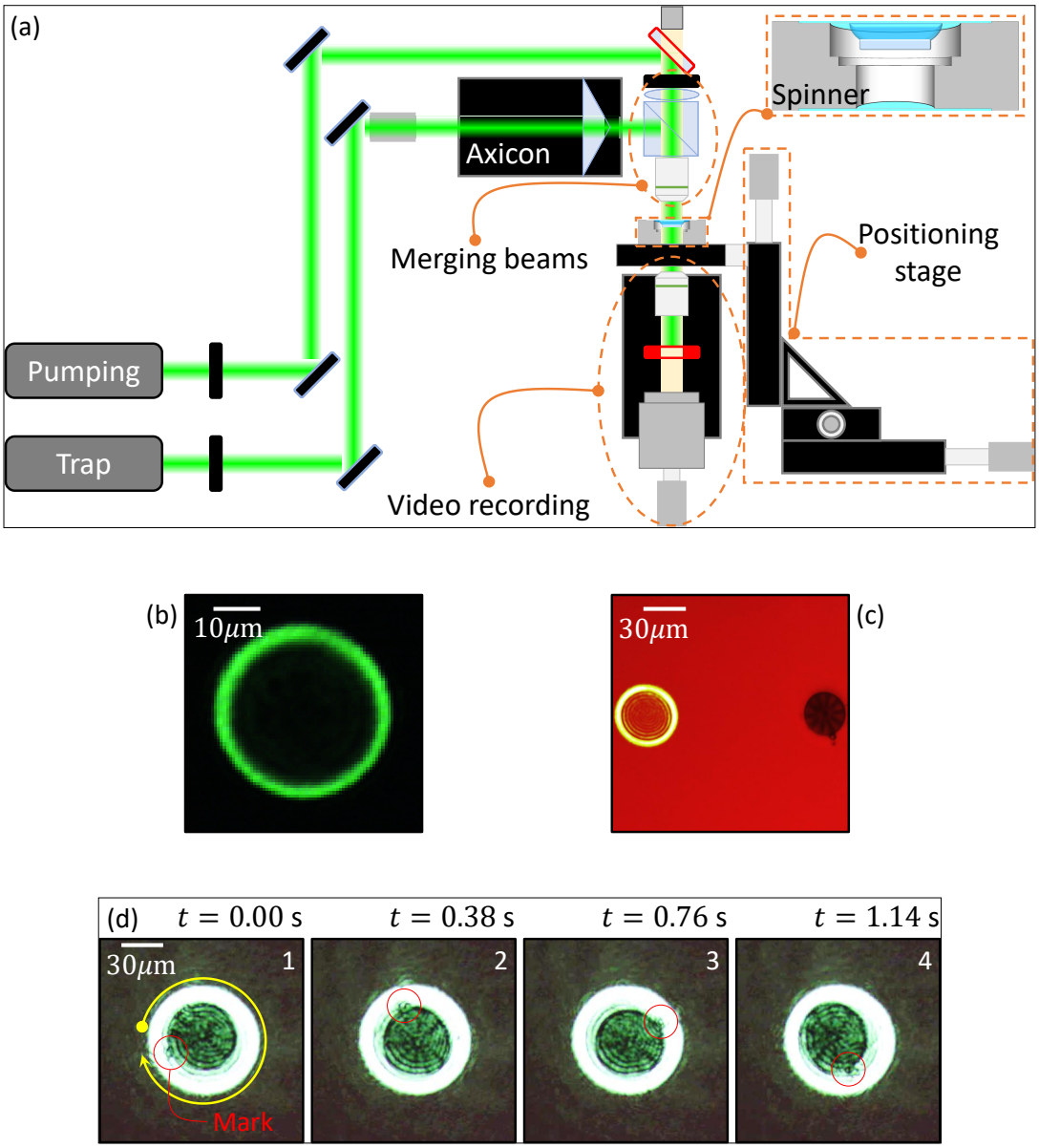

Figure 3.11: *Optical manipulation setup for micro-spinners: (a) The implementation of an axicon in the trapping line is used to generate a ring-shaped intensity distribution. Illustrations of (b) the annular trap and (c) the sample and the trap, where a spinner can be seen on the right side. (d) Sequence of images of the $q = 5$ spinner showing a constant rotation with a ~ 1 Hz frequency under a constant pump of $P \sim 150$ mW power, and a beam waist $w \sim 4R$, where R is the spinner's radius.*

The ring-type profile of the optical field allows the field power to be concentrated in a narrower region than what is achieved using a vortex beam, thus offering larger intensity gradients, hence better lateral confinement. Also, we decided to extend the pumping beam diameter up to five times that of the spinner in order to decrease possible lateral drawbacks of the pumping beam. Here, the ring obtained from the axicon is linearly polarized in order to discard possible spin angular momentum contributions from it.

Except for the optical trap implementation, the rest of the procedure to get the system ready is the same. The spinner is trapped with power of the order or larger than 100 mW. With the spinner fixed at the center of the air/liquid interface of the pending droplet, we start pumping it with a beam having a beam waist several times larger than the radius of the spinner from 1 mW power and power is increased until we observe a continuous and stable rotation of the spinner. An example is shown in Fig.3.11(d) for a $q = 5$ spinner which exhibits constant rotation of ~ 1 Hz frequency under a constant pump of $P \sim 150$ mW power, with a beam waist diameter that is about four times larger than that of the spinner.

Although the element was set into rotation, we conclude that the observed dynamics is not driven by spin-driven transfer of angular momentum from light to matter. Indeed, the direction of rotation is always the same regardless of the polarization state of the pumping light. Experimental facts led us to conclude that the technology used in the manufacture of the spinners does not suit our experimental goal. Therefore, we spent time to search for new options with our collaborators, and in the next section we present the research line that we eventually chose.

3.3 Nanostructured diamond samples

3.3.1 Fabrication and first observations

Although structuring materials can provide the desired spin-orbit optical functionalities, the performance of the fabricated components still depends mostly on

their material properties. Low absorption, high refractive index, high irradiation damage threshold, thermal stability, and high thermal conductivity represent a list of desirable characteristics of the material towards the elaboration of sub-wavelength space-variant structured optical elements offering a chance for implementing spin-orbit optical manipulation and ensure stable performance in a wide range of operating conditions. This led us to choose diamond, which is resilient to hostile environments and ageing, and highly transparent from UV rays to far-infrared bands. Noteworthy, the high refractive index at visible wavelengths and high thermal conductivity of diamond distinguish it from other available materials and make it attractive for optics and photonics, making it our best candidate to pursue our experimental quest.

The technological process involves many design-trial-test cycles, which is the approach we used so far. In fact, the choice of diamond material come with advances in material structuring made by our collaborators. The idea is to start with commercially available diamond membranes with thicknesses ranging from 50 nm to several tens of microns. The first batch of non-cut structures made from 5 µm-thick membranes is shown in Fig.3.12, where scanning electron image and bright field optical images are shown.

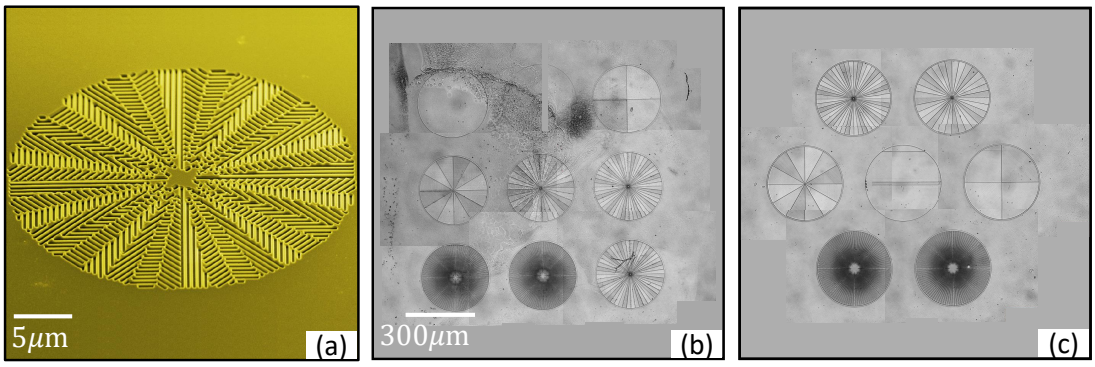

Figure 3.12: *The first batch of nanostructured geometric phase plates fabricated from a diamond membrane. (a) Scanning electron micrograph of an optical vortex generator for* $\ell = 10$. *Extension to any other wavelength is easily achieved by design, adapting the grating pitch, depth and filling factor to the need. (b,c) Bright field optical images of the two nanostructured membranes with* 5 µm *thickness, whose elements are not yet cut in their periphery.*

The features of these new diamond structures are: (i) n = 2.425, (ii) Λ = 400 nm, (iii) $W = \Lambda/2$, and (iv) h = 270 nm, see Fig.3.2, all these values optimized for a light source of λ = 532 nm. In what follows, both the structural and optical characterization of the samples are presented with various values of q for 300 µm diameter optical elements.

On the one hand, the structural characterization consists in the determination of the effective optical axis and birefringent phase retardation of the nanostructured elements. This is done using polarization-based optical imaging device. The result are collected in Fig.3.13(a,b).

On the other hand, we demonstrate the optical vortex generation for the operating wavelength λ = 532 nm, which is done by illuminating the elements with

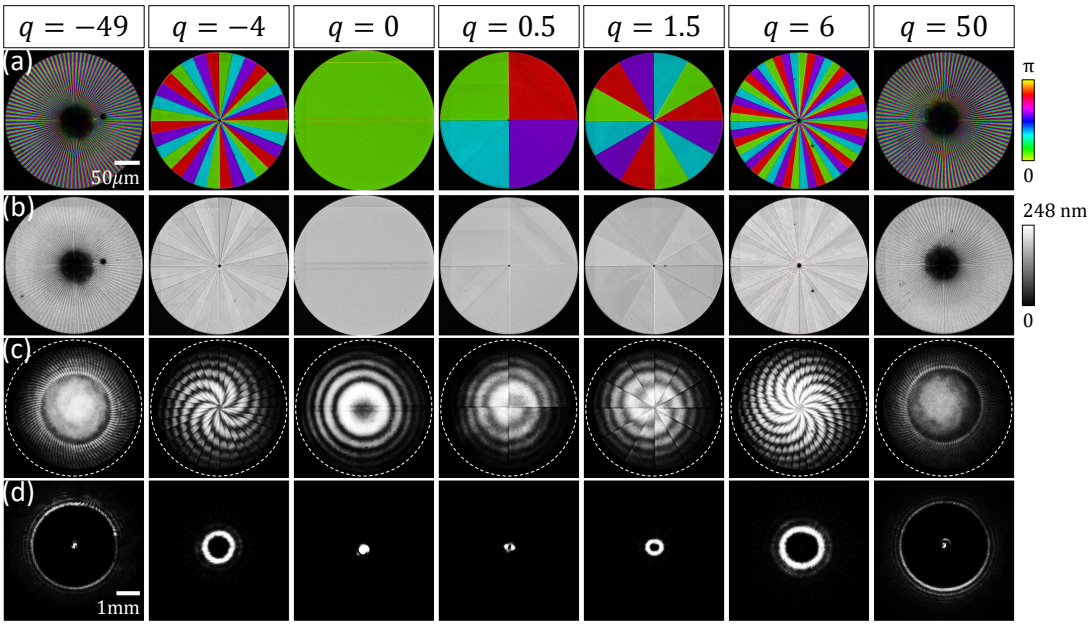

Figure 3.13: *Structural (a,b) and optical (c,d) characterization of the first batch of diamond elements. (a) Slow axis orientation maps, see orientation angle color bar at the end of the row. (b) Maps of birefringent phase retardation in gray scale, from 0 to 248 nm, see color bar at the end of the row. (c) Interference patterns between a test beam and the vortex generated by each structure in its plane for incident circular polarization. (d) Far-field image of the generated vortex.*

a circularly polarized Gaussian beam. The vortex phase structure is revealed in the plane of the structures by observing the interference patterns obtained using a coaxial Gaussian reference beam, see Fig.3.13(c). One can appreciate the $2|\ell|$ spiral arms whose handedness depend on the sign of q at fixed input handedness for the circular polarization state. Note that for the largest values of q the interference fringes are hardly seen while thin ring-shaped intensity profile with large diameters imply poor interference with the Gaussian reference beam in the central part. In addition, the characteristic doughnut-shaped intensity patterns of the generated vortex beam are also observed in the far field, as displayed in Fig.3.13(d).

For spinners with $q = -49$ and $q = 50$, the observed dark central region of ~ 45 µm in diameter in Fig.3.13(a,b) results from high structural gradients, which imply a loss of the topological structuring. This explains that the light passing through the center of the structure is not processed.

3.3.2 Releasing diamond structures

After having validated the ability to fabricate nanostructured diamond microdisks, we design and fabricate 25 spinners with various values of q and collected after cut on three distinct glass coverslips using PVA layer, as we introduced in Fig.3.3 for silicon nitride samples. The collection is shown in Fig.3.14. Then we used the previously introduced light-assisted on-demand release protocol for all the

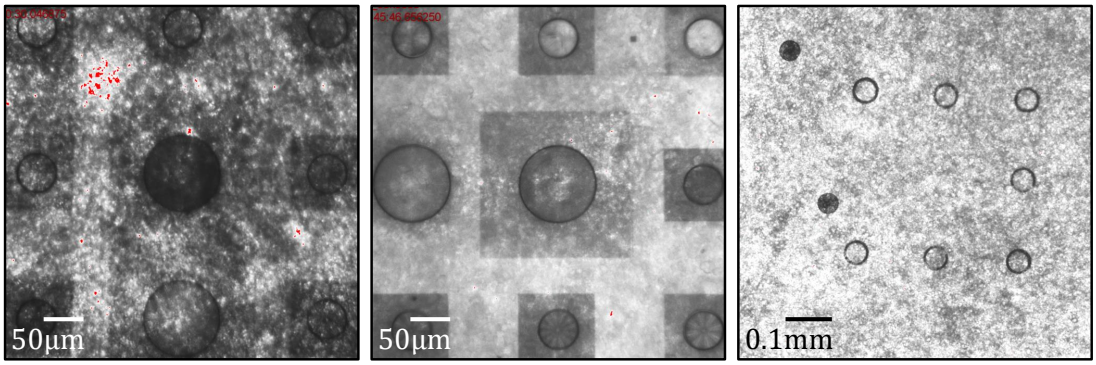

Figure 3.14: *Collection of 25 spinners on their original substrate as received: 21 with a* 50µm *diameter and 4 with* 100µm *diameter.*

spinners.

Despite technical manufacturing improvements, it remains a challenge to remove the glue and only one third of the full set of spinners is eventually properly released on individual coverslips, as shown in Fig.3.15. The spinners that we consider to be functional are those entirely free from PVA, so in principle, they are more transparent and easily distinguishable optical inspection using a polarized microscope. At first glance the functional spinners (see green boxes) are distinguished from those that are not (see red boxes). We tried to remove the glue layer that obscures some of the spinners, but after five attempts for each spinner, we could only substantially improve the situation for one spinner only which is the spinner #12 in Fig.3.15.

Finally, the set of functional structures is characterized optically from a structural point of view, the results being displayed in Fig.3.16.

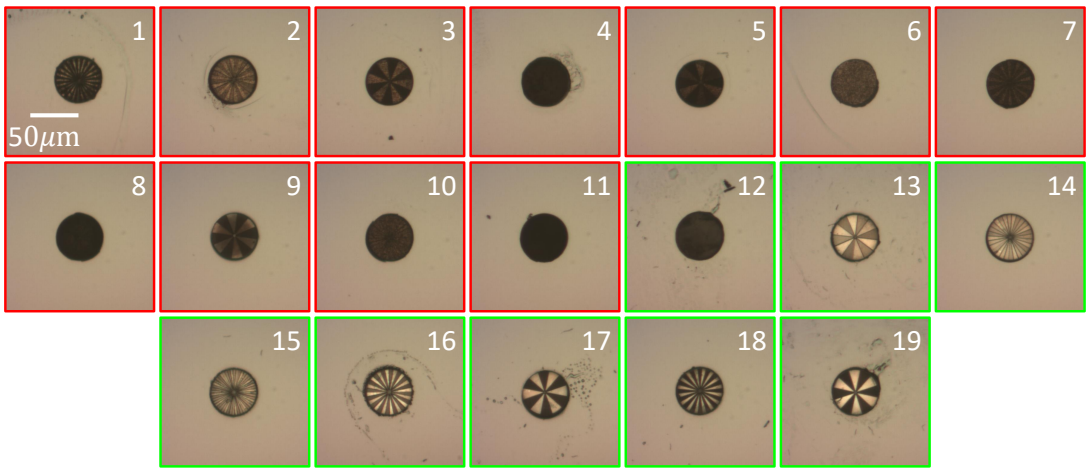

Figure 3.15: *Images taken between two uncrossed linear polarizers show the set of spinners collected from the first batch. Each one is already on an individual coverslip after several transfers (up to five). The spinners framed in green are those we find suitable for optical manipulation, those framed in red are not, and we further discard their study.*

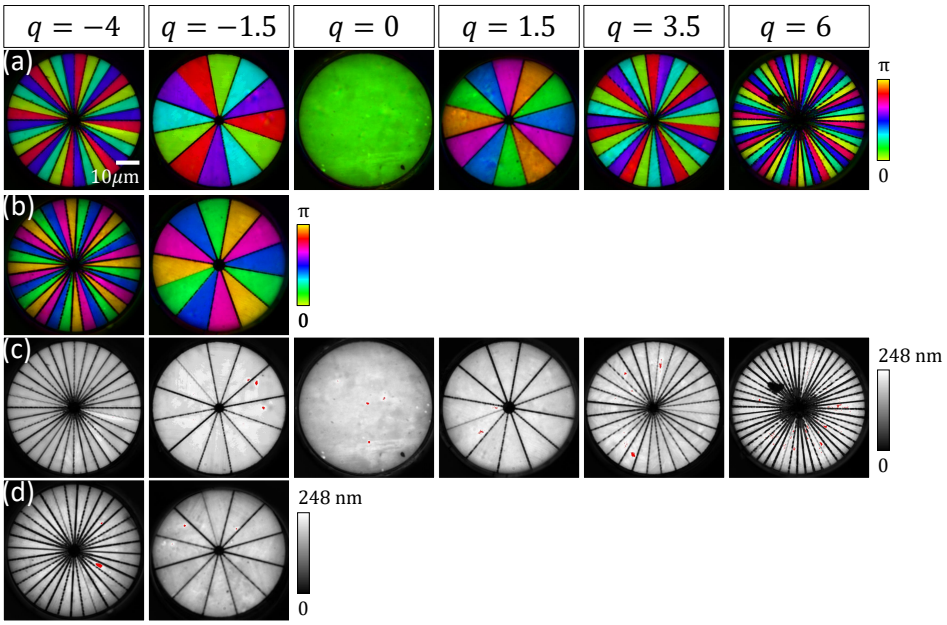

Figure 3.16: *Structural optical characterization of the functional set of spinners after individual release and storage protocol is done. (a,b) Slow axis orientation maps, see orientation angle color bar at the end of the row. (c,d) Maps of birefringent phase retardation in gray scale, from* 0 *to* 248 nm*, see color bar at the end of the row.*

3.3.3 Optical manipulation attempt on a flat substrate

When we started to implement optical manipulation experiments with diamond structures, we faced three main challenges when using the pending droplet approach. Namely, (i) the spinners escape from a Gaussian beam having a beam waist diameter of the order of the spinner diameter; (ii) the use of extended Gaussian beam leads to random motion of the spinners; (iii) the impurities inside the droplet gather next to the spinner and eventually interact with the pumping beam and also with the ring trap option that we tested here. Consequently, similarly to the case of silicon nitride spinners, our conclusions are that, even if some rotational motion could be observed, the pending droplet strategy cannot be considered successful. This led us to consider the manipulation of spinners deposited on a flat solid substrate.

For this purpose, a glass substrate is coated with a hydrophilic agent to favor

a thin film of water between the spinner and the substrate, with the hope to prevent crippling friction. Practically, the following protocol is used

- Coverslips are washed by leaving them for > 1 h into Hellmanex™ at 2 % vol. solution in ultrapure water at room temperature.
- Coverslips are dried in a ~ 800 ml beaker covered by aluminum foil with small holes, heating them up on the hot plate at 150° for > 1 h.
- Coverslips are treated twice putting them into a Mirapol™ at 5 % vol. solution in ultrapure water for > 15 min. The glass was dried up between rounds following the previous protocol for a longer time (~ 3 h).
- The cell was built up with the coverslip slightly wet, see Fig.3.17 that shows the experimental chamber.

The last step before optical manipulation is to transfer the spinner from its storage coverslip to the hydrophilic substrate, which is done again using a laser beam. As the spinner lands on the coated surface, it is free of translational and rotational movement within the space delimited by the lateral air/liquid interface. In practice, the spinners are occasionally stuck during optical manipulation. In that case, we use the laser beam to play around until the spinner hopefully jumps to a region where motion is again made possible.

The first test was made on the spinner with $q = 0$ and using right-handed circularly polarized Gaussian beam with waist diameter equal to that of the spinner.

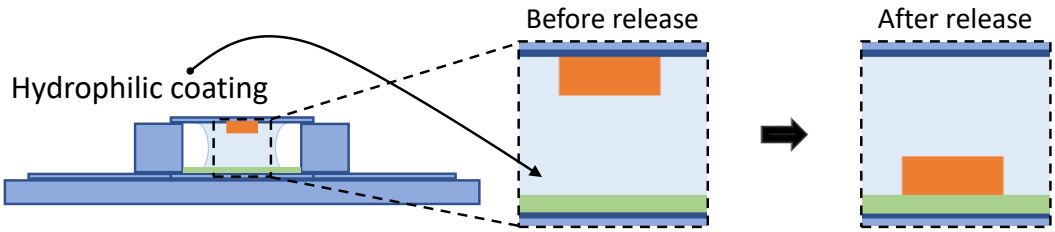

Figure 3.17: *Experimental arrangement dedicated to the optical manipulation of spinners. When the spinner lands on the hydrophilic coated substrate after optical release, it is ready to be manipulated.*

We start with a power of 10 mW and gradually increase it until rotational motion is observed. Changing the helicity of the circularly polarized light, should lead to rotation reversal, which is a crucial test to assess spin-controlled torque exerted on the spinner. The highlights of this test are:

- Stable rotation is observed above an incident ~ 45 mW.
- The direction of rotation depends on the circular polarization handedness.
- The rotation frequency increases with the beam power.

The quantitative assessment of the rotational dynamics is made by observing the spinner between 'half-crossed' linear polarizers. By doing so, we obtain a non-zero illuminated background while the light transmitted through the spinner (that is a half-waveplate for $q = 0$) is fully modulated. This is shown in Fig.3.18(a,b). From the dynamics of the normalized transmission through the spinner we extract the rotation frequency, which is four times smaller than the modulation frequency of the measured transmission.

We notice that for $q \neq 0$ spinners, the above procedure does not apply as such since there are always sectors that transmit light and some that do not. In that case, our approach consists of analyzing the dynamics of the correlation coefficient between the images corresponding to the times $t = 0$ and $t \neq 0$ as a function of time, see Fig.3.18(c,d). We obtained the 2D correlation coefficient with a program that tracks the spinners frame by frame. Thus we calculate the coefficient using only the image of the spinners area. The wobbling of the spinners was observed during the tests, is negligible in most cases, and clearly being confined within the ring trap: compare images (a) and (c) of Fig.3.18, where the yellow ring represents the location of the ring trap. In this case, every local maximum of the correlation coefficient corresponds to a situation when the pizza sectors are positioned in the same manner. Therefore, one period of rotation corresponds to N periods for the correlation coefficient dynamics for an N-sector spinner. This can be ascertained in Fig.3.18(c,d).

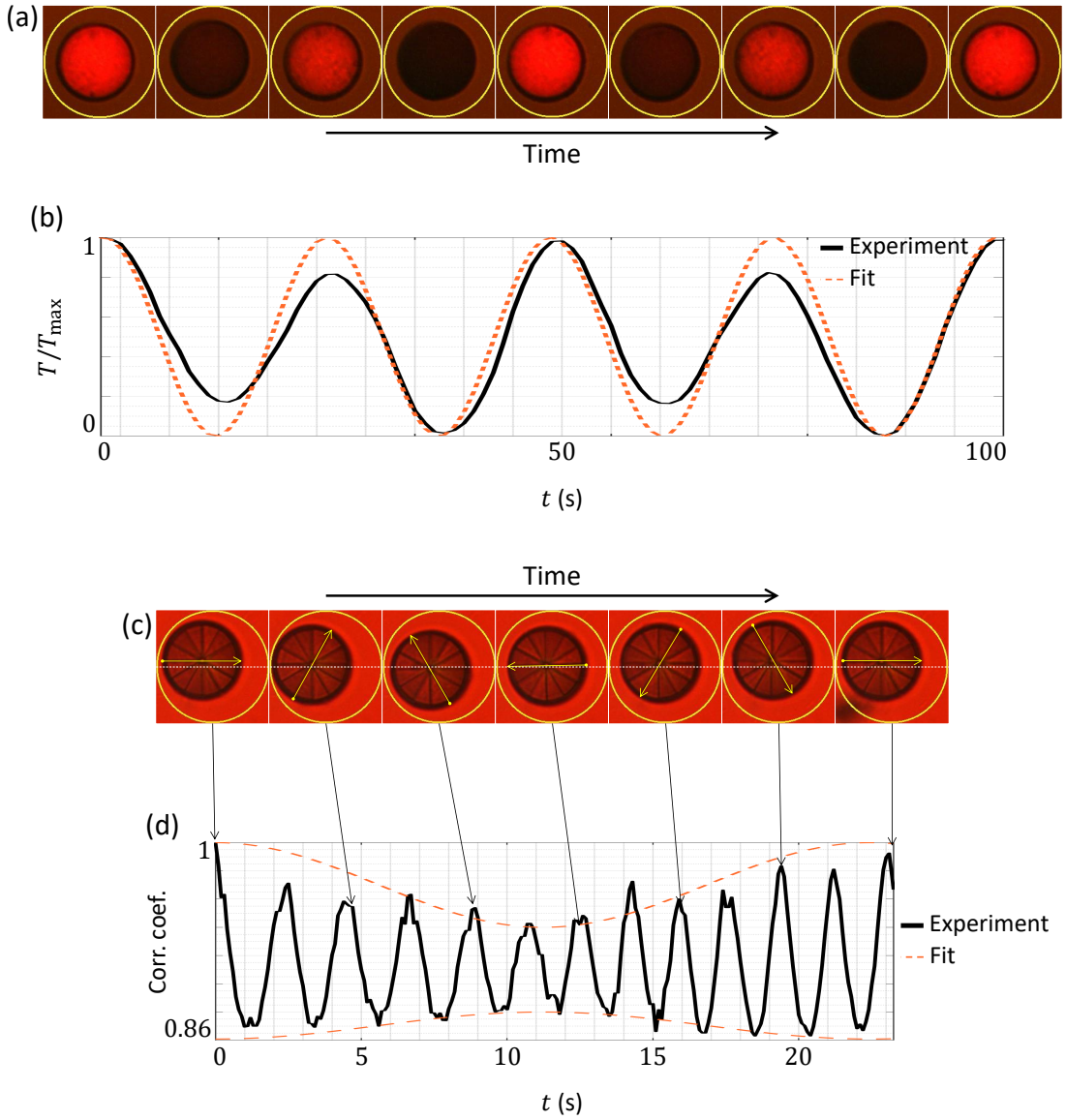

Figure 3.18: *First spin-dependent spinner rotation, where the annular trap and the hydrophilic coating are both at play. (a,c) Sequence of images over one full turn of the $q = 0$ and $q = -1.5$ spinners, respectively, (see text for details). The yellow circles indicates the position of the annular trap. (b) Normalized optical transmission of the spinner as a function of time (solid line), adjusted with a sinusoidal function (dash line) in order to extract the rotation frequency. (d) 2D correlation coefficient (see text for details) between a frame and the first frame as a function of time.*

Importantly, the experiments carried out with the three available spinners with $q > 1$ (see Fig.3.16) unveil a new challenge: no torque reversal is observed between $q = 0$ and $q > 1$, as expected from Eq.2.8. Indeed, all the spinners have the same direction of rotation for a given polarization state of the incident beam.

Regardless of this unexpected result, we performed the quantitative analysis of the full set of spinners. The results are presented in Fig.3.19. The spinner rotation frequency f as a function of optical power P and polarization (RH or LH) for $q = 0$ is shown in Fig.3.19(a). In this figure, every event correspond to a independent measurement providing 10 full turns. From the collected data set, average values and corresponding standard deviations are defined. The power dependence of the spinning frequency is adjusted by a linear fit, independently for RH and LH incident beam polarization state. Almost identical slopes are found, which supports the fact that the spin angular momentum transfer from light to matter is at the origin of the observed dynamics.

Even though the study of spinners with $q \neq 0$ led us to conclude that the observation of left-handed torque is not conclusive, we scrutinize the rotational dynamics as a function of q in order to find a trace of the effect of the structure of the element on its rotation frequency. In particular we studied how much of the incident optical power is processed in order to asses properly the balance of angular momentum for our light/matter system. This is made by defining the optical performance of vortex generation

$$\eta = \frac{P_{-\sigma}}{P_{+\sigma} + P_{-\sigma}}, \tag{3.1}$$

where σ is the helicity of the incident circular polarized beam, and $P_{\pm\sigma}$ are the power of the output circularly polarized components of the field. This quantity is measured in a static configuration, hence at low incident power. Results are shown in Fig.3.19(b). Then, we are able to report on the effect of q on the rotational dynamics by normalizing the observed spinning frequencies according to the incident power and vortex generation efficiency. Namely $f/(P\eta)$, see Fig.3.19(c). The expected trend $f/(P\eta) \propto (1 - q)$ is clearly not observed.

We suspect that residues of glue could be at the origin of this non-understood behavior. Indeed,

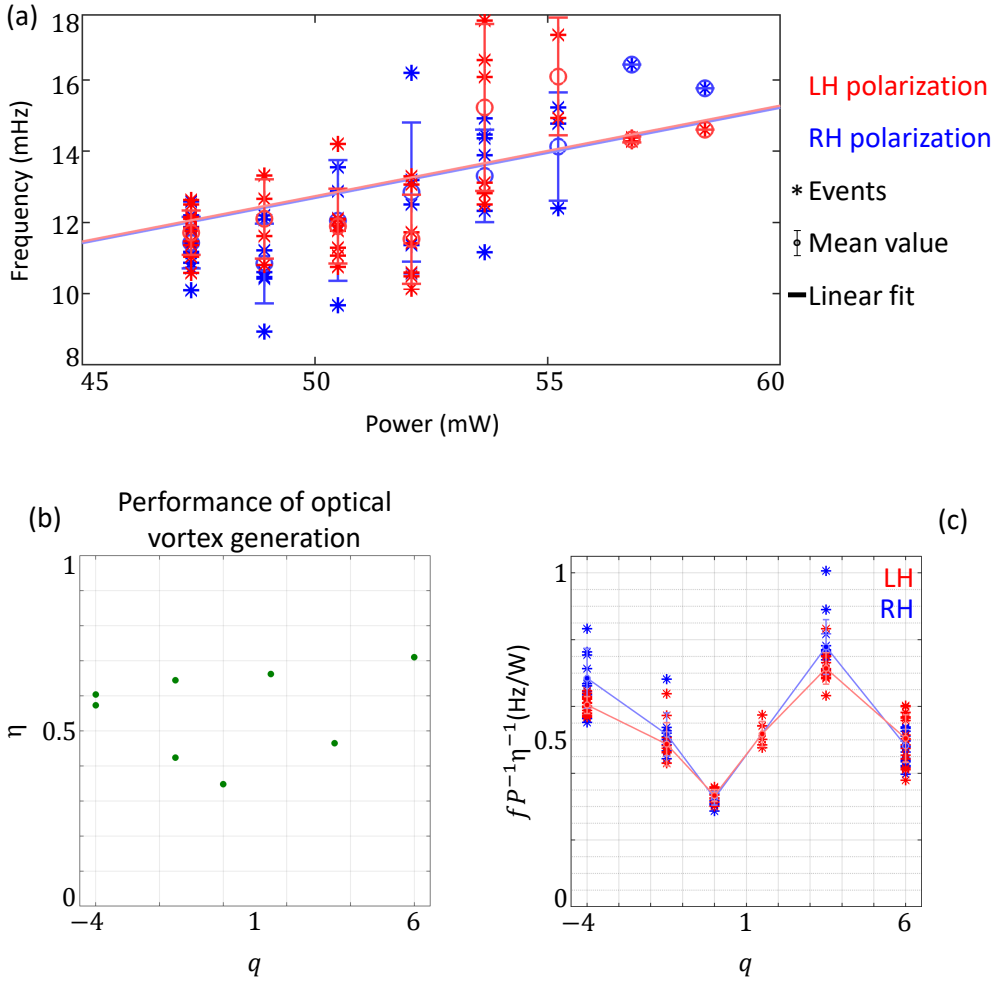

Figure 3.19: *Data analysis from the experiment with diamond spinners. (a) Plot of the $q = 0$ spinner rotation frequency as a function of the incident power and right (RH) o left (LH) handedness of the circular polarization, as well as a linear adjustment for both, RH and LH cases. (b) Vortex generation efficiency eta of our samples, measured directly under experimental conditions. (c) Spinner rotation frequency weighted by converted optical power as a function of q for right and left handed circular polarization of the incident light.*

- This can lead to absorption optical power during manipulation of the spinner resulting in undesirable thermal effects (see Fig.3.6) and even contribute with a sufficient right-handed torque component to overcome the contribution of the orbital part of the structure (see Fig.1.6).

- This can modify the optical properties of the material, as can be seen in extreme cases in the spinners indicated with a red frame in Fig.3.15.

Summarizing, even though we do not detect a net effect of the nanostructured diamond elements, which would have ideally revealed the left-handed torque, these first observations are nevertheless important advances for us towards our initial goal. Then, we have considered a novel manufacturing process that get rid of the use of glue, which is the purpose of the next section.

3.4 Free standing diamond spinners

3.4.1 Fabrication and characterization

By updating the various fabrication steps, a protocol has been established to obtain free-standing spinners that do not require the use of glue to recover the spinners. First, the diamond membrane is structured to get the uncut spin-orbit optical micro elements as it has been done in Fig.3.12, which corresponds here to Fig.3.20(a). Second, the sample is covered by a resin and a mask delimiting the area to be protected is designed. Namely, spinners, frame, and two diametrically opposed small holding triangular tips are aimed at being preserved, while the rest will be totally etched. The result of the deep etching is shown in Fig.3.20(b) and a zoom on one spinner is shown in Fig.3.20(c). Third, the final step consists to remove the resin leftovers, see Fig.3.20(d), for an image between crossed polarizers where the leftovers are removed already. The full set of fabricated free-standing spinners is shown in Fig.3.20(e).

Structural and optical characterization is performed in a similar manner as done for the previous generation of spinners (see Sec.3.3) before to release them. A summary is shown in Fig.3.21. In the present case, a direct mechanical release is possible since the spinners are no longer attached to a substrate. This is done by using an arrangement as depicted in Fig.2.3(b,c), where the array of the spinners is placed above the trench with water and the menisci ready, as used in the lateral force experiment, which act as a collecting net. Manually, by a gently touching

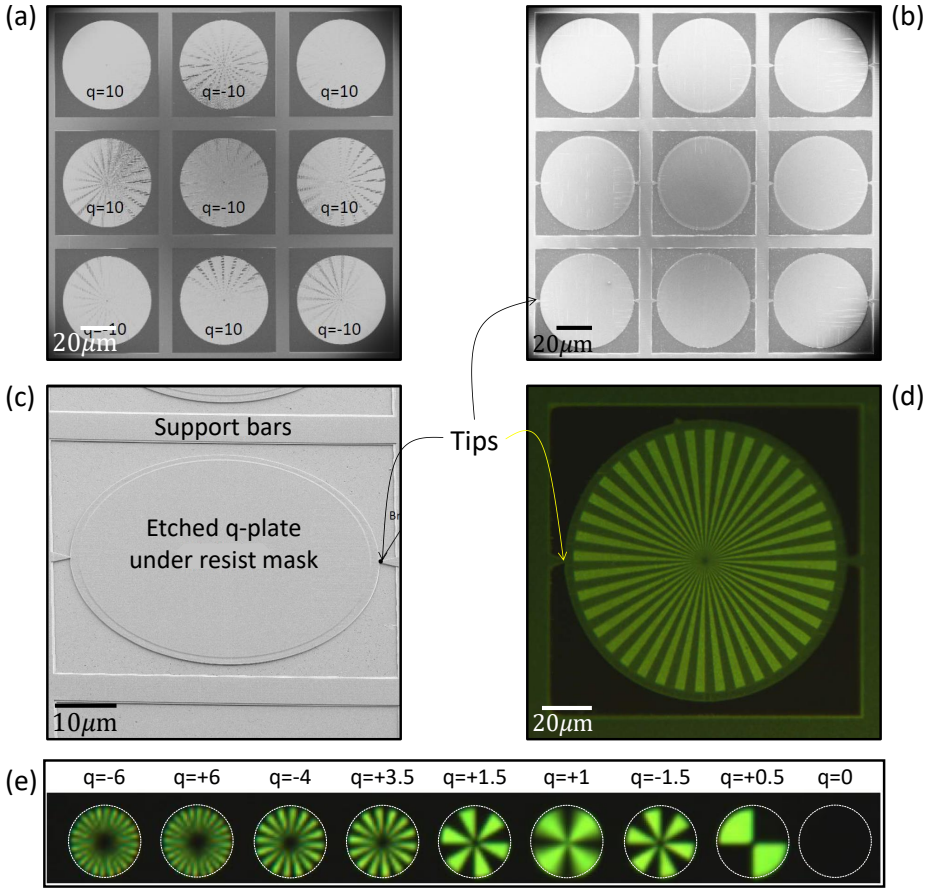

Figure 3.20: *Freestanding spinners manufacturing: (a) First, q-plates structuring. (b) Second, deep etch mask (c) Third, after etching. (d) Forth, a single finished spinner holded by two tips after the mask was removed. (e) Final set of structure under linear crossed polarized light.*

the array with the tip of a needle, a bunch of spinners are released and caught. Afterwards, we collect the released spinners by drying up the trench and proceed using the previously introduced light assisted release protocol.

Once a full set of spinners is released, a complementary characterization is also performed for this last generation of spinners. Namely, the transmittance and vortex conversion efficiency is measured from the analysis of the output field using a Gaussian beam with diameter equals that of the diameter of the spinner. (50 µm). For transmittance we measure $T = P_{out}/P_{in}$, and for the vortex conversion efficiency we measured Eq.3.1. The retardance is measured

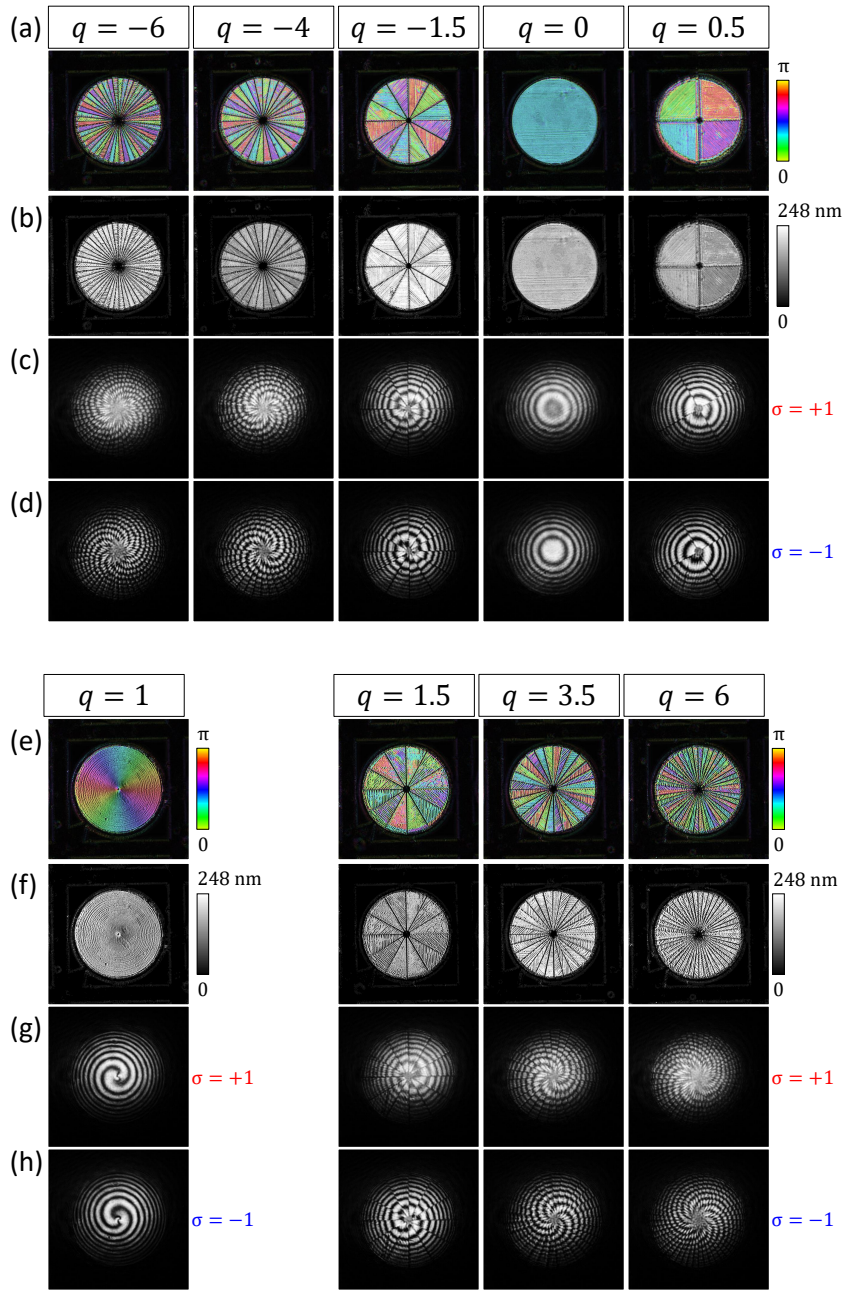

Figure 3.21: *Structural and optical characterization of a random row in the free standing spinners array. (a,e) Slow axis orientation maps, see the orientation angle color bar at the end of the row. (b,f) Maps of birefringent phase retardation in gray scale, from* 0 *to* 248 nm, *see color bar at the end of the row. (a,b,e,f) These images look different with respect previous ones due to a change in the software of our polarimetry device. (c,d,g,h) Interference patterns between a test beam and the vortex generated by each structure in its plane for the incident circular polarization marked at the end of the row. The figure is arranged in three groups which correspond to right-handed structures ($q < 0$), neutral structure ($q = 0$), and the left-handed structures ($q > 1$).*

with the images shown in Fig.3.21(b,f) as

$$\Delta = \Delta_{max} \frac{\iint_D I \; dA}{\iint_D \; dA}, \tag{3.2}$$

where I is the pixel value, D is the spinners region, and Δ_{max} is given by the color bar of the image: notice that the images have change from those of previous characterizations due to technical difficulties with the native software of our polarimetry device, what led us to install OpenPolScope open source software. The results are shown in Fig.3.22.

In view of measured performance with a laser beam having the characteristics of that used for optical manipulation. All is in place for spinning the spinners.

3.4.2 Optical manipulation experiment

Eventually, we give a try to manipulate the spinner at the air/liquid interface. Firstly, the spinners are mechanically released from the suspending frame using a needle and touching with care the structured membrane. A set of spinners thus detach and, using previously described protocol, each spinner is collected on an

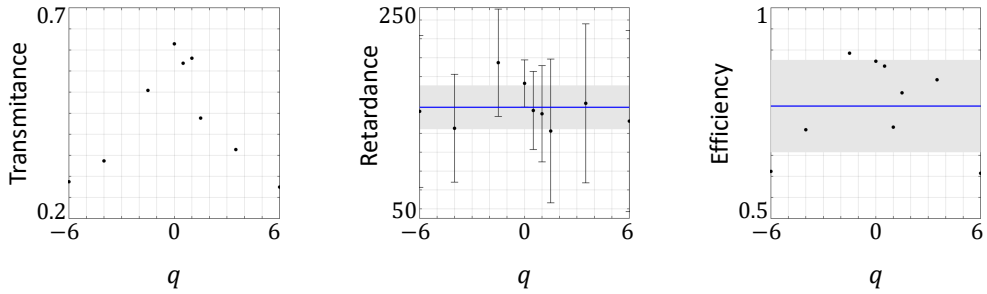

Figure 3.22: *Complementary characterization of the spinner optical performance for a full set of spinners. Transmittance and efficiency are measured using an incident Gaussian beam fitting the spinner area, directly measured from the array in air before releasing the spinners. The retardance is measured from polarimetric device (see text for details). (a) Transmittance as a function of q value. (b) Retardance and (c) vortex conversion efficiency where the blue line is the mean value and the gray band is the standard deviation.*

individual coverslip.

When releasing spinners from the coverslip into the droplet, we notice that, with the usual parameters of the beam, the necessary releasing optical power jump to a value larger than 200 mW, which supports reduced absorption. However, here again, the spinner escapes the pumping beam without the presence of a ring trap, see Fig.3.23(a). In contrast, when the ring trap is switched on, steady rotation can be observed, see for instance Fig.3.23(b).

Another option is here proposed to get rid of the ring-tarp, which consist to structure substrates in order to have micro-pools of 10 µm and 100 µm diameter, see Fig.3.24(a). As can be seen in Fig.3.24(b), the micro-pool strategy allows observing stable rotation with using the Gaussian pumping beam alone.

However, despite all our efforts, we still do not observe the effect of the

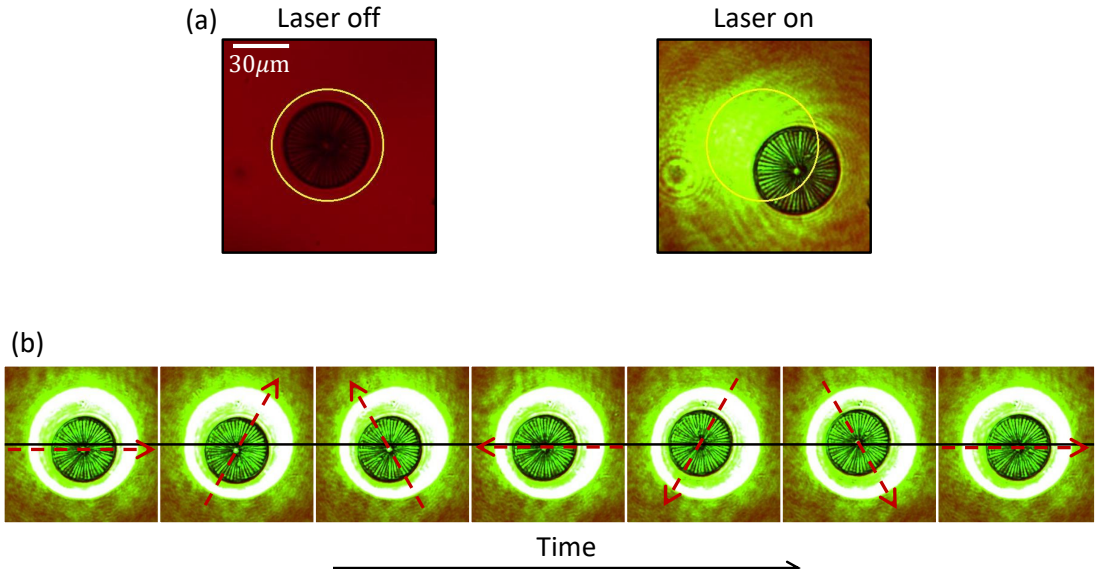

Figure 3.23: *(a) Spinner escaping from the Gaussian laser beam at a droplet air/liquid interface using same protocol as that used in section 3.2.2. Here, the yellow ring corresponds to the location of the beam. (b) A complete turn of the spinner is shown on a flat glass substrate coated with a hydrophilic layer and immersed in water, limiting its escape with a linearly polarized ring of light, and pumped with a second independent beam of diameter equal to that of the spinner.*

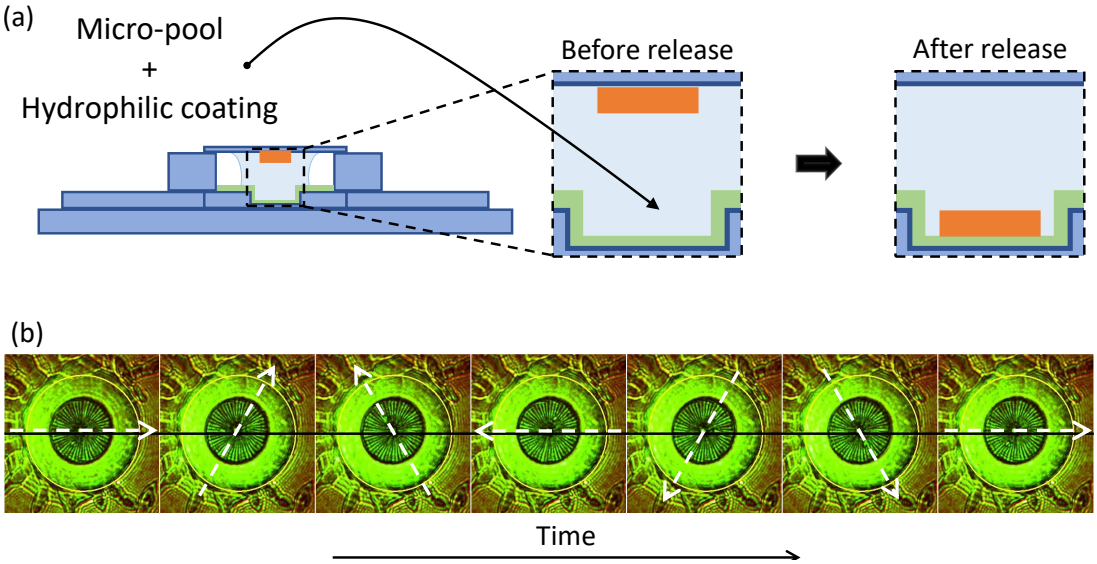

Figure 3.24: *(a) We have added an anisotropy in the topography of the substrate to eliminate the drag effect of the hydrodynamic flow that we assume, and it still comes from an effect of absorption of the spinner and which we could not eliminate. (b) A complete turn of a spinner is observed inside a micro-pool milled in a glass substrate and coated by a hydrophilic layer to eliminate the need for the ring trap and to be able to extend the pumping beam more in order to have a flatter intensity profile.*

nanostructuring of the plates q, i.e., the rotation is dependent on the helicity of the pumping beam but independent of the value q.

The hydrophilic coating is now the only element that could be a source of uncontrolled interactions with the spinners. In the same way, we have overlooked a possible alteration of the optical performance of the structures due to the environment that contains the spinner: water. This is because the characterization has always given us consistent results with the design and material of the structures. However, air may be trapped within the structured area of the sample, which, when immersed in the liquid, alters the birefringence of the material locally. Therefore, we will discuss strategies that could be implemented in the future, which is the subject of the ending chapter of this thesis.

CHAPTER 4

Conclusions and perspectives

Summarizing all the work done in this thesis, we were able to report experimentally on various unexplored yet direct mechanical manifestations of spin-orbit mechanical effects of light. At the macroscopic scale, successful experimental demonstrations of lateral forces and left-handed torques have been reported. At the microscopic scale, however, we encountered a lot of practical challenges at various levels. Namely, we mention the choice of the material, the fabrication process of nanostructural micro-optical elements, the ability to handle micro-samples into experimental chambers in order to implement optical manipulation experiment, and the mechanical stability of optical manipulation protocol. Along the way, we solved a lot of issues and reported on a robust and reproducible protocol to eventually have on-demand microscopic spin-orbit optical elements ready to be manipulated by light. Unfortunately, despite the intense instrumental efforts, we were not succeeding to demonstrate the left-handed torque direct manifestation at the microscale. Still, spin-controlled rotational dynamics has been observed, which encourages us to pursue the efforts after present thesis is completed.

In fact, additional attempts have been made while the manuscript was under writing. One of them is summarized in Fig.4.1. It consist to place an experimental chamber on a piezoelectric actuator in order to make the bottom surface on which sits the sample vibrating. The idea is is here to develop a protocol free from stuck-events as we were facing even with the best strategy discussed at the en of Chap.3. Unfortunately, such attempts have been unsuccessful. An option could be, instead, to make use of surface acoustic wave generated directly on the substrate on which is deposited the sample. This could be a future action.

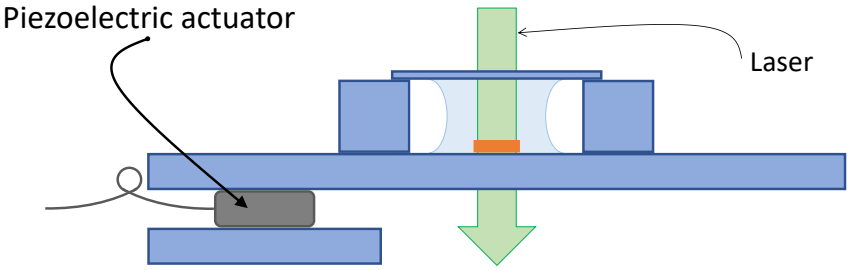

Figure 4.1: *Sketch of the experimental approach aiming at creating mechanical vibration of the substrate on which sits the micro-optical element to be manipulated in order to facilitate its ability to rotate under the action of light.*

Another option concerns the improvement of the release protocol. So far, we were using brutal mechanical release of free-standing spinners using relatively large needle. The drawback of this approach is that it is not safe at all regarding the high level of fragility of the arrays of free-standing spinners. With the aim at have full control over the mechanical release of a given spinner, we used a micro-needle and a set has been built in order to poke any desired spinner out of the array. The process is illustrated in Fig.4.2(a), where is shown how a single spinner can be released. By placing a pool with a curved interface below the array, the poked spinner can be recovered at air/fluid interface, ideally towards further optical manipulation. The image of such a spinner having land on air/water in-

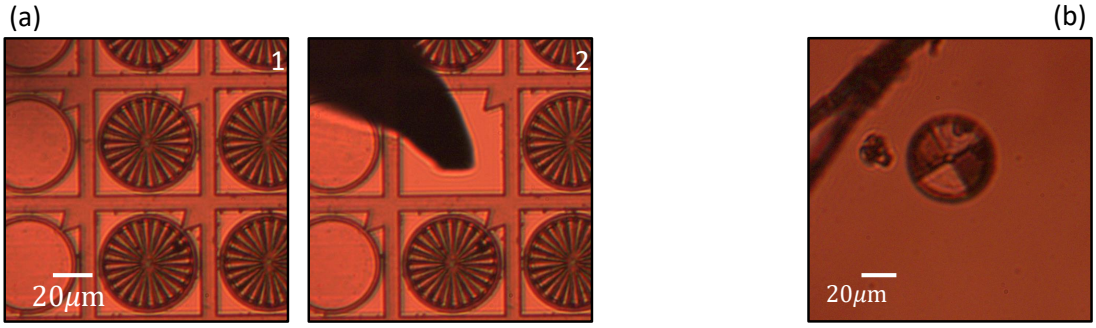

Figure 4.2: *(a) Sequence of image illustrating the micro-poking strategy: (1) initial array, (2) just after poke, the shadow of the micro-needle can be seen. (b) Image of a poked spinner that has landed on air/water interface place underneath the array.*

terface is shown in Fig.4.2(b).

In the continuation of this thesis, it is plan to further work to eventually achieve the initial goal of Chap.3. Current developments carried out in our team make us believe that the mission remains possible.

Bibliography

[1] L. Allen, M. W. Beijersbergen, R. J. C. Spreeuw, and J. P. Woerdman, "Orbital angular momentum of light and the transformation of Laguerre-Gaussian laser modes", *Physical Review A* **45**, 8185 (1992).

[2] D. Marcuse, *Light transmission optics*, *Van Nostrand Reinhold electrical/-computer science and engineering series* (Van Nostrand Reinhold Company, 1982).

[3] S. J. van Enk and G. Nienhuis, "Eigenfunction description of laser beams and orbital angular momentum of light", *Optics Communications* **94**, 147 (1992).

[4] G. Nienhuis and L. Allen, "Paraxial wave optics and harmonic oscillators", *Physical Review A* **48**, 656 (1993).

[5] L. Allen, J. Courtial, and M. J. Padgett, "Matrix formulation for the propagation of light beams with orbital and spin angular momenta", *Physical Review E* **60**, 7497 (1999).

[6] J. Kepler, *De cometis libelli tres* (Augustae Vindelicorum, Augsburg, 1619).

[7] I. Newton, *Opticks: or, A treatise of the reflections, refractions, inflexions and colours of light.* (Sam. Smith and Benj. Walford, London, 1704).

[8] J. C. Maxwell, *A Treatise on Electricity and Magnetism* (Dover Publications Inc., New York, 1954), Vol. 2.

[9] P. N. Lebedev, "Experimental examination of light pressure", *Annalen der Physik* **6**, 433 (1901).

[10] E. F. Nichols and G. F. Hull, "A Preliminary Communication on the Pressure of Heat and Light Radiation", *Phys. Rev. (Series I)* **13**, 307 (1901).

[11] E. F. Nichols and G. F. Hull, "The pressure due to radiation", *Proceedings of the American Academy of Arts and Sciences* **38**, 559 (1903).

[12] A. Sadowsky, "Ponderomotive action of electromagnetic and light waves on crystals", *Acta et Commentationes imp. Universitatis Jurievensis* **7**, 1 (1899).

[13] J. H. Poynting, "The wave motion of a revolving shaft, and a suggestion as to the angular momentum in a beam of circularly polarised light", *Proceedings of the Royal Society of London. Series A, Containing Papers of a Mathematical and Physical Character* **82**, 560 (1909).

[14] R. A. Beth, "Mechanical Detection and Measurement of the Angular Momentum of Light", *Physical Review* **50**, 115 (1936).

[15] J. F. Nye and M. V. Berry, "Dislocations in Wave Trains", *Proceedings of the Royal Society A: Mathematical, Physical and Engineering Sciences* **336**, 165 (1974).

[16] H. He, M. E. J. Friese, N. R. Heckenberg, and H. Rubinsztein-Dunlop, "Direct Observation of Transfer of Angular Momentum to Absorptive Particles from a Laser Beam with a Phase Singularity", *Physical Review Letters* **75**, 826 (1995).

[17] D. Gao, W. Ding, M. Nieto-Vesperinas, X. Ding, M. Rahman, T. Zhang, C. Lim, and C.-W. Qiu, "Optical manipulation from the microscale to the nanoscale: fundamentals, advances and prospects", *Light: Science &Amp; Applications* **6**, e17039 (2017).

[18] D. Castelvecchi, E. Gibney, and M. Warren, "Laser tricks win physics Nobel", *Nature* **562**, (2018).

[19] S. Fürhapter, A. Jesacher, S. Bernet, and M. Ritsch-Marte, "Spiral phase contrast imaging in microscopy", *Optics Express* **13**, 689 (2005).

[20] G. A. Swartzlander, E. L. Ford, R. S. Abdul-Malik, L. M. Close, M. A. Peters, D. M. Palacios, and D. W. Wilson, "Astronomical demonstration of an optical vortex coronagraph", *Optics Express* **16**, 10200 (2008).

[21] K. Dholakia, N. B. Simpson, M. J. Padgett, and L. Allen, "Second-harmonic generation and the orbital angular momentum of light", *Physical Review A* **54**, R3742 (1996).

[22] A. Mair, A. Vaziri, G. Weihs, and A. Zeilinger, "Entanglement of the orbital angular momentum states of photons", *Nature* **412**, 4 (2001).

[23] G. Gibson, J. Courtial, M. J. Padgett, M. Vasnetsov, V. Pas'ko, S. M. Barnett, and S. Franke-Arnold, "Free-space information transfer using light beams carrying orbital angular momentum", *Optics Express* **12**, 5448 (2004).

[24] B. Thidé *et al.*, "Utilization of Photon Orbital Angular Momentum in the Low-Frequency Radio Domain", *Physical Review Letters* **99**, 087701 (2007).

[25] A. Ashkin, J. M. Dziedzic, J. E. Bjorkholm, and S. Chu, "Observation of a single-beam gradient force optical trap for dielectric particles", *Optics Letters* **11**, 288 (1986).

[26] J. Chen, J. Ng, Z. Lin, and C. T. Chan, "Optical pulling force", *Nature Photonics* **5**, 531 (2011).

[27] V. Kajorndejnukul, W. Ding, S. Sukhov, C.-W. Qiu, and A. Dogariu, "Linear momentum increase and negative optical forces at dielectric interface", *Nature Photonics* **7**, 787 (2013).

[28] O. Brzobohatý, V. Karásek, M. Šiler, L. Chvátal, T. Čižmár, and P. Zemánek, "Experimental demonstration of optical transport, sorting and self-arrangement using a 'tractor beam"', *Nature Photonics* **7**, 123 (2013).

[29] G. A. Swartzlander, T. J. Peterson, A. B. Artusio-Glimpse, and A. D. Raisanen, "Stable optical lift", *Nature Photonics* **5**, 48 (2010).

[30] K. Y. Bliokh, A. Y. Bekshaev, and F. Nori, "Extraordinary momentum and spin in evanescent waves", *Nature Communications* **5**, 3300 (2014).

[31] A. Canaguier-Durand and C. Genet, "Transverse spinning of a sphere in a plasmonic field", *Physical Review A* **89**, 033841 (2014).

[32] S. Sukhov, V. Kajorndejnukul, R. R. Naraghi, and A. Dogariu, "Dynamic consequences of optical spin–orbit interaction", *Nature Photonics* **9**, 809 (2015).

[33] M. Antognozzi *et al.*, "Direct measurements of the extraordinary optical momentum and transverse spin-dependent force using a nano-cantilever", *Nature Physics* **12**, 731 (2016).

[34] F. J. Rodríguez-Fortuño, N. Engheta, A. Martínez, and A. V. Zayats, "Lateral forces on circularly polarizable particles near a surface", *Nature Communications* **6**, 8799 (2015).

[35] S. Scheel, S. Y. Buhmann, C. Clausen, and P. Schneeweiss, "Directional spontaneous emission and lateral Casimir-Polder force on an atom close to a nanofiber", *Physical Review A* **92**, 043819 (2015).

[36] R. Movassagh and S. G. Johnson, "Optical Bernoulli forces", *Physical Review A* **88**, 023829 (2013).

[37] S. Sukhov, V. Kajorndejnukul, J. Broky, and A. Dogariu, "Forces in Aharonov–Bohm optical setting", *Optica* **1**, 383 (2014).

[38] A. Y. Bekshaev, K. Y. Bliokh, and F. Nori, "Transverse Spin and Momentum in Two-Wave Interference", *Physical Review X* **5**, 011039 (2015).

[39] S. Fardad, A. Salandrino, A. Samadi, M. Heinrich, Z. Chen, and D. N. Christodoulides, "Scattering detection of a solenoidal Poynting vector field", *Optics Letters* **41**, 3615 (2016).

[40] S. B. Wang and C. T. Chan, "Lateral optical force on chiral particles near a surface", *Nature Communications* **5**, 3307 (2014).

[41] R. P. Cameron, S. M. Barnett, and A. M. Yao, "Discriminatory optical force for chiral molecules", *New Journal of Physics* **16**, 013020 (2014).

[42] A. Hayat, J. P. B. Mueller, and F. Capasso, "Lateral chirality-sorting optical forces", *Proceedings of the National Academy of Sciences* **112**, 13190 (2015).

[43] A. Canaguier-Durand and C. Genet, "Plasmonic lateral forces on chiral spheres", *Journal of Optics* **18**, 015007 (2016).

[44] M. H. Alizadeh and B. M. Reinhard, "Transverse Chiral Optical Forces by Chiral Surface Plasmon Polaritons", *ACS Photonics* **2**, 1780 (2015).

[45] N. Kravets, A. Aleksanyan, and E. Brasselet, "Chiral Optical Stern-Gerlach Newtonian Experiment", *Phys. Rev. Lett.* **122**, 024301 (2019).

[46] D. Hakobyan and E. Brasselet, "Left-handed optical radiation torque", *Nature Photonics* **8**, 610 (2014).

[47] S. H. Simpson and S. Hanna, "Optical trapping of spheroidal particles in Gaussian beams", *Journal of the Optical Society of America A* **24**, 430 (2007).

[48] K. Volke-Sepúlveda, S. Chávez-Cerda, V. Garcés-Chávez, and K. Dholakia, "Three-dimensional optical forces and transfer of orbital angular momentum from multiringed light beams to spherical microparticles", *J. Opt. Soc. Am. B* **21**, 1749 (2004).

[49] A. Jesacher, S. Fürhapter, C. Maurer, S. Bernet, and M. Ritsch-Marte, "Reverse orbiting of microparticles in optical vortices", *Opt. Lett.* **31**, 2824 (2006).

[50] D. Haefner, S. Sukhov, and A. Dogariu, "Conservative and Nonconservative Torques in Optical Binding", *Physical Review Letters* **103**, 173602 (2009).

[51] J. Chen, J. Ng, K. Ding, K. H. Fung, Z. Lin, and C. T. Chan, "Negative Optical Torque", *Scientific Reports* **4**, 6386 (2014).

[52] M. Nieto-Vesperinas, "Optical torque on small bi-isotropic particles", *Optics Letters* **40**, 3021 (2015).

[53] A. Canaguier-Durand and C. Genet, "Chiral route to pulling optical forces and left-handed optical torques", *Physical Review A* **92**, 043823 (2015).

[54] F. Mitri, "Negative optical spin torque wrench of a non-diffracting non-paraxial fractional Bessel vortex beam", *Journal of Quantitative Spectroscopy and Radiative Transfer* **182**, 172 (2016).

[55] J. Chen, S. Wang, X. Li, and J. Ng, "Mechanical effect of photonic spin-orbit interaction for a metallic nanohelix", *Optics Express* **26**, 27694 (2018).

[56] N. Sule, Y. Yifat, S. K. Gray, and N. F. Scherer, "Rotation and Negative Torque in Electrodynamically Bound Nanoparticle Dimers", *Nano Letters* **17**, 6548 (2017).

[57] F. Han, J. A. Parker, Y. Yifat, C. Peterson, S. K. Gray, N. F. Scherer, and Z. Yan, "Crossover from positive to negative optical torque in mesoscale optical matter", *Nature Communications* **9**, 4897 (2018).

[58] R. Bhandari, "Polarization of light and topological phases", *Physics Reports* **281**, 1 (1997).

[59] Z. Bomzon, G. Biener, V. Kleiner, and E. Hasman, "Space-variant Pancharatnam–Berry phase optical elements with computer-generated subwavelength gratings", *Optics Letters* **27**, 1141 (2002).

[60] G. Biener, A. Niv, V. Kleiner, and E. Hasman, "Formation of helical beams by use of Pancharatnam–Berry phase optical elements", *Optics Letters* **27**, 1875 (2002).

[61] S. Pancharatnam, "Generalized theory of interference and its applications - Part I. Coherent pencils", *Resonance* **44**, 247 (1956).

[62] M. V. Berry, "Quantal phase factors accompanying adiabatic changes", *Proceedings of the Royal Society of London A* **392**, 45 (1984).

[63] H. Sarkissian, S. V. Serak, N. V. Tabiryan, L. B. Glebov, V. Rotar, and B. Y. Zeldovich, "Polarization-controlled switching between diffraction orders in transverse-periodically aligned nematic liquid crystals", *Optics Letters* **31**, 2248 (2006).

[64] L. Marrucci, C. Manzo, and D. Paparo, "Optical Spin-to-Orbital Angular Momentum Conversion in Inhomogeneous Anisotropic Media", *Physical Review Letters* **96**, 163905 (2006).

[65] D. Hakobyan, *Spin-orbit optomechanics of space-variant birefringent media*, Ph.D. thesis, Université de Bordeaux, Talence, 2016.

[66] V. G. Levich, *Physicochemical Hydrodynamics* (Prentice Hall, Englewood Cliffs, N. J., 1962).

[67] Y. Shimotsuma, P. G. Kazansky, J. Qiu, and K. Hirao, "Self-Organized Nanogratings in Glass Irradiated by Ultrashort Light Pulses", *Phys. Rev. Lett.* **91**, 247405 (2003).

[68] A. Karbalaei, R. Kumar, and H. Cho, "Thermocapillarity in Microfluidics—A Review", *Micromachines* **7**, 13 (2016).

[69] S. R. Nersisyan, N. V. Tabiryan, D. M. Steeves, and B. R. Kimball, "The Promise of Diffractive Waveplates", *Optics and photonics news* **21**, 40 (2010).

[70] M. Rioux, R. Tremblay, and P. A. Bélanger, "Linear, annular, and radial focusing with axicons and applications to laser machining", *Appl. Opt.* **17**, 1532 (1978).

[71] H. Magallanes and E. Brasselet, "Macroscopic direct observation of optical spin-dependent lateral forces and left-handed torques", *Nature Photonics* **12**, 461 (2018).

[72] K. Y. Bliokh, F. J. Rodríguez-Fortuño, F. Nori, and A. V. Zayats, "Spin–orbit interactions of light", *Nature Photonics* **9**, 796 (2015).

[73] D. Hakobyan, H. Magallanes, G. Seniutinas, S. Juodkazis, and E. Brasselet, "Tailoring Orbital Angular Momentum of Light in the Visible Domain with Metallic Metasurfaces", *Advanced Optical Materials* **4**, 306 (2016).